SOVIET ATOMIC ENERGY

АТОМНАЯ ЭНЕРГИЯ
(ATOMNAYA ÉNERGIYA)

TRANSLATED FROM RUSSIAN

$\frac{c}{b}$ CONSULTANTS BUREAU, NEW YORK

SOVIET ATOMIC ENERGY

SOVIET ATOMIC ENERGY

CONTENTS

Engl./Russ.

CONTENTS

(continued)

Engl./Russ.

ARTICLES

PHYSICOCHEMICAL INTERACTION OF OXIDE FUEL WITH THE CLADDING

OF THE FUEL ELEMENTS OF A FAST REACTOR

V. A. Tsykanov, E. F. Davydov,   UDC 621.039.542
E. P. Klochkov, V. K. Shamardin,
V. N. Golovanov, and F. N. Kryukov

A necessary condition for achieving the planned burnout of fuel in fast reactors is maintenance of the seal of the cladding of fuel elements throughout the period of operation. Corrosion of the cladding as a result of its physicochemical interaction with fission products of the fuel decreases the short- and long-term hardness and plasticity, which is taken into account in designing the fuel elements by increasing the thickness of the cladding [1]. To decrease or avoid corrosion damage to the cladding, it is necessary to clarify the nature and mechanisms of corrosion, as well as the role of separate fission products in the corrosion processes.

In this paper, we give a classification of the forms of corrosion damage and we examine the role of the main corrosion-active fission products (cesium, iodine, and tellurium) in the corrosion of fuel-element cladding irradiated in BOR-60.

Samples and the Procedure Used in the Investigation. We investigated the physicochemical interaction between the fuel, containing the fission products, and the cladding for fuel elements with uranium—plutonium oxide fuel in tablet form and OKh16N15M3B steel cladding in an austenitic state. We irradiated the fuel elements in a BOR-60 reactor in order to study their operational efficiency.

We present below the main characteristics and conditions of irradiation of the fuel elements:

outer diameter and thickness of the cladding, mm	6.9 × 0.4
cladding material	Austenitic OKh-16N15M3B steel
starting stoichiometric coefficient (O/M)	1.98–2.00
Pu/(Pu + U)	0.15–0.20
maximum power of the fuel elements per unit length, kW/m	53.0
maximum temperature of the inner surface of the cladding, °K	960
maximum burnout, % of heavy atoms	14

We studied the interaction between the fuel element and the cladding for polished specimens, cut out of different fuel elements as well as from sections of a single fuel element. We studied the structure of the interaction zone with the help of a remote MIM-14 optical microscope, and we studied the distribution of chemical elements with an x-ray microanalyzer MAR-2, equipped for operation with moderately active samples [2]. Maintenance of the starting chemical composition and morphology of the products of interaction of the fuel core with the cladding in the course of preparation of the samples was considered to be of special importance. For this, we performed the sectioning and polishing without using any materials which either dissolved the products of interaction or which contain the same components as the possible products of interaction. In important cases, we performed these operations beneath a film consisting of dehydrated mineral oil. In cases when the sample had to be cooled for the cutting operation, we protected the surface of the section with a polymerized film consisting of a solution of nitrocellulose in amyl acetate.

With the help of an x-ray spectral microanalysis we investigated the redistribution of the chemical elements in the main metal of the cladding, the composition and distribution of elements in the products of corrosion and in the fuel core. We followed the role of separate fission products of the fuel in the corrosion process by means of identification of the corrosion products. The physicochemical processes, in which different fission products par-
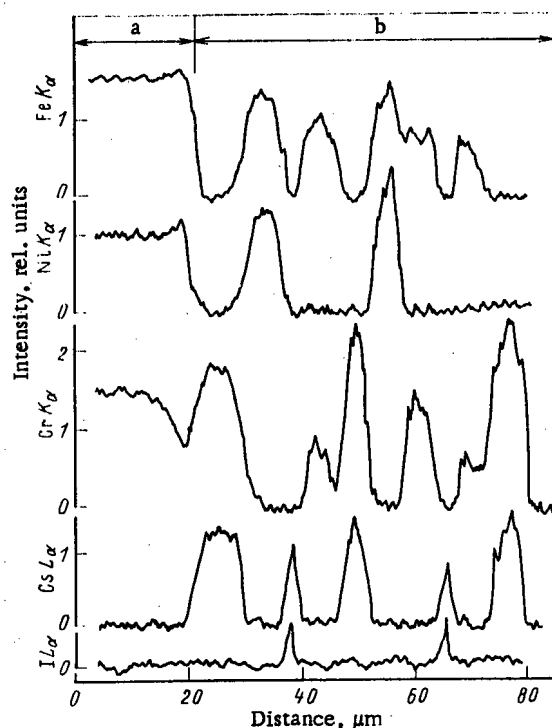
Fig. 1. Distribution of chemical elements in the products of matrix-corrosion of the jacket at a temperature of 940°K and burnup of 10% of the heavy atoms in the fuel in the main metal (a) and in the corrosion products (b).

ticipate, can occur in the same section of the cladding, which complicates the analysis of corrosion-induced damage, or in different sections of the jacket, which permits studying different forms of corrosion independently.

Results. As metallographic investigations of the transverse sections of the fuel elements showed [3], general (matrix) and intercrystallite corrosion of the cladding occurs at temperatures above 770°K as a result of the physicochemical interaction with the oxide fuel. The general corrosion consists of a uniform nonselective interaction of the cladding material with the fuel core, as a result of which the thickness of the cladding decreases. The products of matrix corrosion are nonmetallic compounds or mixtures of nonmetallic compounds with metallic particles, located in the gap between the fuel and the main metal of the cladding.

The x-ray spectral microanalysis established that the products of the matrix corrosion include iron, chromium, nickel, cesium, and small quantities of iodine. At cladding temperatures of 770–850°K, the elements in the corrosion products are distributed relatively uniformly. At cladding temperatures above 850°K, the following segregations of chemical elements were observed in the products of corrosion: chromium–cesium, iron–chromium and in some cases cesium–iodine. The metallic particles consisted of iron and nickel (Fig. 1).

Cesium was recorded in specimens cut out closer to the center of the active part of the fuel elements on the surface of the fuel core together with uranium and plutonium. Tellurium was recorded in the peripheral layer of the core together with cesium and was never observed in the products of matrix corrosion. The redistribution of chemical elements in the main metal of the cladding was observed at a temperature above 920°K and was characterized by a depletion of chromium on the inner side of the cladding (Fig. 1).

An x-ray spectral microanalysis of the samples with intercrystallite corrosion of the cladding established that there exist two forms of intercrystallite corrosion damage with intrinsic characteristic distribution of chemical elements in the region of corrosion. The distinguishing feature of the first type of intercrystallite corrosion is the presence of cesium in the corrosion-damaged grain boundaries. In this case, the chemical composition of the boundary regions of the grains in the material remains unchanged (Fig. 2). Such corrosion of the cladding was observed in the upper part of the fuel elements after irradiation up to burnup of more than 3% of the heavy atoms. With an increase in the duration of the ir-

208
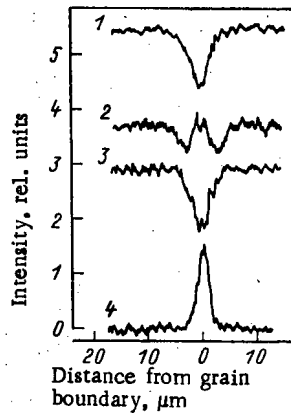
Fig. 2. Distribution
of elements near the
boundary of a grain,
subjected to corrosion
as a result of the in-
teraction with cesium:
1) FeKα; 2) CrKα; 3)
NiKα; 4) CsLα.
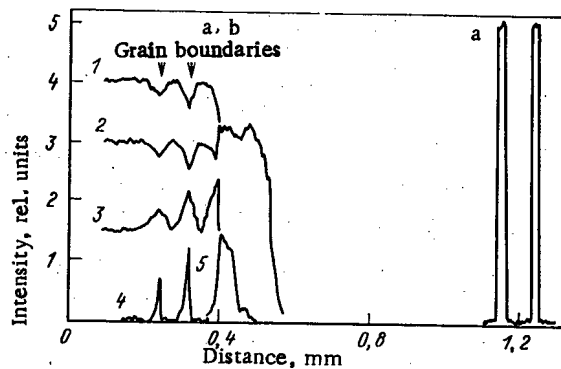
Fig. 3. Distribution of elements in
the region of intercrystallite corro-
sion, caused by interaction with io-
dine for the cladding (a) and fuel (b):
1) FeK$_\alpha$; 2) CrK$_\alpha$; 3) NiK$_\alpha$; 4) IL$_\alpha$; 5)
CsL$_\alpha$.

radiation, the region of corrosion damage spreads downward to the center of the active part
of the elements. However, when more than 7% of the heavy atoms are burned up, corrosion
slowed down. The maximum depth of such corrosion constituted ∿70 μm and practically did not
increase with burnup in the range 8-14% of the heavy atoms.

The characteristic feature of the second type of intercrystallite corrosion is the
presence of iodine on the corrosion-damaged grain boundaries and the change in the relative
content of the basic components of the steel in regions near the grain boundaries (Fig. 3).
In addition, the components of the steel cladding were present in the nearest-lying peripheral
regions of the fuel core: iron in the form of metallic inclusions and chromium, dissolved
in the fuel in the oxide state. In this case, in regions near the grain boundaries subjected
to corrosion, the content of iron and chromium is lower and the content of nickel is higher
than in the starting steel. Cesium was present together with uranium and chromium on the
surface of the core near the zone of corrosion damage of the cladding. This form of corro-
sion in cladding made of OKh16N15M3B steel is encountered most often in investigations of
spent fuel elements with oxide fuel. Corrosion damage of cladding was already observed with
fuel burnup of ∿2% of the heavy elements.

As the burnup increased, the corrosion damage, spreading both into the bulk and along
the inner surface of the cladding, increased. The maximum depth of such corrosion consti-

209
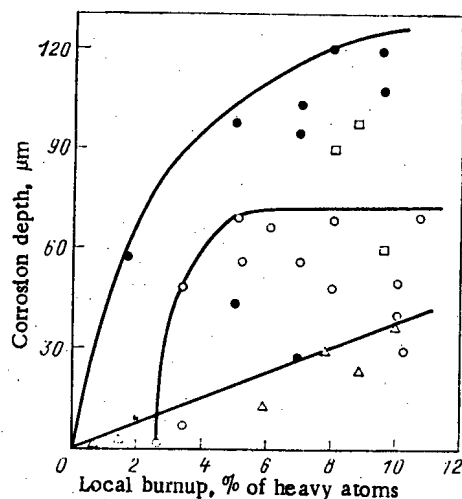
Fig. 4. Dependence of the depth
of corrosion of fuel-element
cladding on burnup of fuel at
temperatures of 920–960°K: Δ)
general corrosion in the presence
of cesium; ○,●) intercrystal-
lite corrosion in the presence
of cesium and iodine, respec-
tively; □) mixed corrosion in
the presence of tellurium.

tutes 120 μm with a cladding temperature of 960°K and local fuel burnup of 10% of the heavy atoms. Aside from these two basic forms, mixed corrosion of cladding, consisting of inter-grain breakdown of the material to a depth of one or several grains in front of the leading edge of general corrosion, was sometimes observed.

The x-ray spectral microanalysis of the samples with mixed corrosion of the cladding revealed the presence in the products of corrosion either of tellurium or tellurium together with small quantities of cesium and components of the steel. Such mixed corrosion of the cladding was observed, as a rule, after irradiation of the fuel elements up to deep burnup (exceeding 8% of heavy atoms).

Thus the data from x-ray spectral microanalysis of spent fuel elements permitted identi-fying four types of corrosion damage of cladding depending on the presence of chemical ele-ments: cesium, indicating general and intercrystallite corrosion; iodine, indicating inter-crystallite corrosion; and tellurium, indicating mixed corrosion. From the results of inves-tigations of spent fuel elements, we obtained the dependence of the depth of each of the four types of corrosion on burnup (Fig. 4). In order to compare the data presented in Fig. 4, the points characterize samples with fuel having an O/M ratio of O/M = 1.98–2.00, and the tem-perature of the inner surface of the cladding is 920–960°K.

Figure 5 shows the temperature dependence of corrosion, obtained from results of post-reactor investigations of fuel elements with the ratio O/M = 1.98–2.00 and local burnup of 8–10% of heavy atoms.

Discussion. The x-ray spectral microanalysis of spent fuel elements established that the formation of a zone of general corrosion of the cladding is related to the effect of cesium. Aside from cesium, the products of matrix corrosion include iodine, but this ele-ment is present together with cesium, and this suggests that it is found in the form of the chemical compound CsI, which is thermodynamically stable at the working temperature [4].

The chemical activity of cesium relative to the cladding is determined by the Cs—Cr—O phase diagram [5] and depends on the temperature of the cladding, the partial pressure of cesium, and the oxygen potential. The values of these parameters in the fuel elements of a fast reactor with the fuel $(U, Pu)O_2$ and O/M = 1.98–2.00 permit the formation of cesium chromates Cs_xCrO_4, where x = 2–5, on the inner surface of the cladding. Since the formation

210
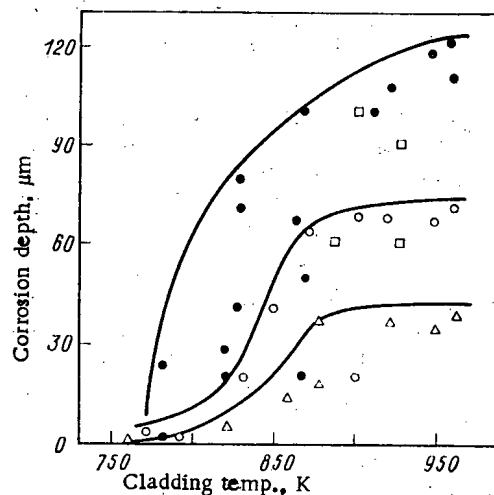
Fig. 5. Temperature dependence
of the depth of corrosion of fuel-
element cladding with fuel burnup
of 8–10% of heavy atoms (the label-
ling is the same as in Fig. 4).

of the indicated chemical compounds is related to depletion of the chromium in the steel,
the other components of the steel, primarily iron, are oxidized. The depth of the zone of
general corrosion for high-temperature sections of the fuel element is determined by the
amount of cesium intruding and, for sections situated closer to the center of the active
zone, by diffusion of chromium out of the cladding.

Under certain conditions, local sections of preferential interaction with cesium, for
example, precipitation of the carbides $M_{23}C_6$ along the grain boundaries, can arise in the
steel cladding [4]. This fact as well as the dependence of the depth of intercrystallite
corrosion in the presence of cesium on burnup (irradiation time) (see Fig. 4) and temperature
(see Fig. 5) indicate the relation of the corrosion to the precipitation of the carbides men-
tioned above on the grain boundaries. For short irradiation times, corresponding to fuel
burnup of less than 3% of the heavy atoms, the coefficient of filling of the grain boundaries
in the steel cladding by carbide precipitates of carbide is small and the interaction with
cesium has a matrix character and does not spread into the bulk along the grain boundaries.
For a burnup of 5–6% of heavy atoms, as a result of the radiation-thermal aging of the steel,
the coefficient of filling of grain boundaries by carbide precipitates reaches a maximum,
and this phenomenon explains the intercrystalline corrosion of steel in the presence of
cesium. For fuel burnup of 6–7% of heavy atoms, the coagulation of the precipitates slows
down the corrosion process, and with burnup exceeding 7% the depth of corrosion does not
increase (see Fig. 4). The relation of intercrystallite corrosion of the cladding in the
presence of cesium to the grain-boundary carbide precipitates is also confirmed by the ab-
sence of such corrosion in heat-treated steels, leading to the coagulation of the carbides.

Another fission product of the fuel, causing intercrystallite corrosion of the OKh16N-
15M3B steel jacket, is iodine, which forms with cesium the chemical compound CsI. Since
during fission of the fuel much more cesium forms than iodine, the latter will be found in
the form of the compound CsI, which is inert relative to the cladding which is confirmed by
extrareactor experiments in the presence of a temperature gradient [6]. However, for values
of the oxygen potential (about −400 kJ/mole and higher, depending on the temperature) created
by fuel with a ratio O/M = 1.98–2.00, cesium participates in competing reactions with the
formation of cesium chromates and uranates or uranoplutonates which are more stable than CsI
[4], which is confirmed by data from x-ray spectral microanalysis over the peripheral region
of the core and inner surface of the cladding. As a result of the action of the temperature
gradient, chemical transport reactions, which give rise to transfer of the components of the
steel into the fuel, become possible.

The rate of this transfer depends on the energy of formation and the vapor pressure of
the metal iodides. The low energy of formation of nickel iodides [6, 7] excludes transfer
of this element, which leads to nickel enrichment of regions near the boundaries (see Fig.
3). The preferential transport of components of the steel from the grain boundaries can be

211

explained by the energy state of the grain boundaries, which gives rise to their higher chemical activity and the high rate of diffusion processes [8, 9].

The x-ray spectral microanalysis of samples with mixed corrosion of cladding showed that this form of corrosion is related to the effect of tellurium. Extrareactor experiments on the compatibility of the tellurium to the steel showed that intense corrosion of steel occurred only in the presence of the liquid phase, but not in the tellurium vapor [10]. Therefore, a necessary condition for corrosion is condensation of tellurium on the inner surface of the cladding. Tellurium in the gas phase migrates into the peripheral region of the fuel core, where the compounds Cs_2Te or UOTe form. In this case, the equilibrium pressure of tellurium in the gas phase is not sufficient for it to condense on the surface of the cladding. An increase in the temperature of the fuel core can increase the equilibrium pressure to a magnitude that makes it possible for tellurium to condense on the cladding.

Conclusions. The investigations of fuel elements with mixed oxide fuel, used in BOR-60, revealed four types of corrosion damage to OKh16N15M3B steel cladding due to the action of fission products. It was shown that the general corrosion develops as a result of the interaction of the cladding with cesium with an oxygen potential created by the mixed oxide fuel. Precipitation of carbides, formed as a result of radiation-thermal aging of the steel, on grain boundaries leads to intercrystallite corrosion of the cladding in the presence of cesium. When mixed oxide fuel with the starting ratio $O/M = 1.98-2.00$ is used in the fuel elements, iodide transport of the components of the steel, giving rise to intercrystallite corrosion of the cladding, occurs. It was demonstrated that chemical activity relative to the stainless steel, leading to corrosion damage to the cladding, is high.

LITERATURE CITED

1. W. Roake, in: Proc. Tech. Committee Meeting on Fuel and Cladding Interaction, Tokyo, IAEA (1977), p. 189.
2. F. N. Kryukov and V. N. Golovanov, in: Apparatus and Methods of X-Ray Analysis, Collection of Papers LNPO "Burevestnik" [in Russian], No. 26, Mashinostroenie, Moscow (1981), p. 22.
3. F. N. Kryukov, V. N. Golovanov, and V. K. Shamardin, Preprint NIIAR-21(536), Dimitrovgrad (1982).
4. M. Bradbury, S. Pickering, and W. Whitlow, [1], p. 51.
5. D. Fee and C. Johnson, J. Nucl. Mater., 96, 80 (1981).
6. M. Aubert and D. Calais, ibid., 58, 257 (1975).
7. U. D. Veryatin et al., in: Thermodynamic Properties of Inorganic Materials [in Russian], Atomizdat, Moscow (1965), p. 110.
8. Physical Metallurgy [Russian translation], No. 2, Mir, Moscow (1968), p. 403.
9. Ya. M. Kolotyrkin and O. V. Kasparova, in: Corrosion and Corrosion Protection [in Russian], Vol. 6, VINITI, Moscow (1978), p. 180.
10. W. Batey and K. Bagley, J. Brit. Nucl. Energy Soc., 13, No. 1, 49 (1974).

08Kh14MF STEEL USED IN NUCLEAR POWER

A. K. Mednikov, P. G. Krutikov,   UDC 669.14.8
V. M. Sedov, V. P. Borisov,
L. I. Loshkova, and A. S. Zlobin

Stainless steels have to be used as constructional materials in order to provide high
reliability in nuclear power systems (NPS), partly on account of the increasing power levels.
Chrome—nickel austenitic steels types 08Kh18N10T, Kh18N9, Kh18N12T, etc. are widely used in
NPS, where they are exposed to various corrosive media, high-intensity ionizing-radiation
fields, high pressures, and thermal stresses for long periods. Research, production experi-
ence, and the use of NPS have shown that austenitic steels alloyed with nickel have the fol-
lowing disadvantages:

1) an elevated tendency to work hardening during manufacture and use;

2) a tendency to corrosion cracking in media containing chlorides, which reduces the
working reliability;

3) poor values for technological parameters such as the yield point, fatigue strength,
and thermal conductivity, along with a high coefficient of linear expansion; and

4) the formation of cobalt radionuclides by activation from corrosion products.

The choice of constructional materials for NPS has not been finally resolved. At
present there are three main ways of improving the working characteristics [1-3]: firstly,
improved preparation of nickel-bearing steels in order to reduce the concentrations of car-
bon, nitrogen, and oxygen to 0.01-0.03 mass %, which should eliminate the tendencies to in-
tercrystallite corrosion and embrittlement; secondly, the production of corrosion-resistant
titanium alloys of elevated resistance to various media; and thirdly, by the use of nickel-
free stainless chromium steels or steels with low nickel contents. Experience has shown that
such steels retain many of the advantages of pearlitic ones (ease of mechanical working, small
linear expansion coefficient, and satisfactory thermal conductivity) while having elevated
resistance to chloride corrosion cracking, pitting, slot corrosion, and also intercrystallite
corrosion at sufficiently low carbon contents. While the strengths of the steels are high,
they have the necessary plasticity and properties stable under prolonged ageing, and they do
not contain scarce nickel, which at the same time tends to improve the radiation environment.
Chromium alloy steels containing 9-15% chromium belong to the martensite and martensite—fer-
rite classes [4]. After heat treatment, these steels contain martensite, structurally free
ferrite, and carbides.

The Production Cooperative at the Central Heavy Engineering Research Institute has de-
veloped a nickel-free chromium steel 08Kh14MF, which has been used in SPP-500-1M and SPP-750
steam superheater separators, RBMK-1000 and RBMK-1500 reactors, and AES and AST heat exchang-
ers. This steel belongs to the martensite—ferrite class: it retains the above advantages
of chromium stainless steels, and its working properties are better, particularly during cold
deformation, and thence do not require heat treatment, while the material shows no tendency
to work hardening, which is important in the rolling of tube panels. 08Kh14MF steel has good
mechanical characteristics over a wide temperature range (Table 1).

The steel has good corrosion resistance in aqueous media at fairly high temperatures
(Table 2). Visual examination of specimens after corrosion tests and removal of the corro-
sion products has shown that 08Kh14MF steel does not show any tendency to pitting or other
forms of corrosion.

Measurements have also been made on the behavior in solutions of the acids used in
power engineering for flushing equipment (Table 3). The corrosion resistance in acids is
satisfactory. Sulfuric and hydrochloric acids are the most corrosive in relation to chromium
steel. The corrosion tests confirm electromechanical studies. Figure 1 shows that the

TABLE 1. Guaranteed Level of Mechanical Properties in Forgings, Billets, Hot-Formed and Cold-Formed Tubes and Hot-Formed and Cold-Formed Sheets Made of 08Kh14MF Steel at 20-500°C

Characteristic	Item	Temp., °C								
		20	100	150	200	250	300	350	400	500
σ_u, MPa	Forgings, billets, hot-formed tubes	550	530	520	510	500	500	500	460	380
	Cold-formed tubes and sheets	450	440	430	420	410	400	400	360	300
$\sigma_{0.2}$, MPa	Forgings, billets, hot-formed tubes	350	340	330	320	310	300	300	280	240
	Cold-formed tubes and sheets	250	250	240	230	220	200	200	180	160
δ, %	Forgings, billets, hot-formed tubes	20	20	20	19	19	18	18	18	20
	Cold-formed tubes and sheets	22	22	21	20	20	18	18	18	22
ψ, %	Forgings, billets, hot-formed tubes	60	60	60	58	58	55	55	54	65
	Cold-formed tubes and sheets	60	60	60	58	58	55	55	54	65

TABLE 2. Corrosion Rate for 08Kh14MF Steel at 350°C, $g/m^2 \cdot day$

Medium	Test conditions	Test time, h			
		250	500	1000	2000
Borated water containing 10 g/kg of H_3BO_3 + 0.02 g/kg of KOH at pH 8.25, O_2 content 1 mg/kg	In solution	0,159	0,149	0,096	0,062
	In saturated vapor zone	0,326	0,312	0,216	0,120
Double-distilled water, O_2 content 1 mg/kg	In solution	—	0,288	0,197	0,132
	In saturated vapor zone	—	0,316	0,264	0,174

largest currents (over 10^{-2} A/cm^2) occur in HCl, and the least in HNO$_3$. The steel after activation is rapidly passivated in pure water (Fig. 2). The steel becomes completely passive after 500 h, and the currents at potentials from 0 to 0.7 V are not more than 10^{-6} A/cm^2. Laboratory studies have confirmed tests on specimens made under working conditions in nuclear power stations. This means that 08Kh14MF steel can be recommended for steam superheater separators for nuclear power stations containing RBMK-1000 and RBMK-1500 reactors.

A major line in the use of nuclear fuel is the production of low-grade heat from NPS. Tests were therefore made on heat exchangers in which the tube bundles were made of steels 08Kh14MF and St. 20 (Table 4). Under the test conditions, which were close to the working conditions in the AST-500 project, 08Kh14MF steel had high corrosion resistance and showed no local forms of corrosion. In the same tests it was found that the amounts of corrosion products on St. 20 were greater than those on 08Kh14MF by more than a factor four, where the deposits on the latter tubes consisted mainly of lepidocrocite (γ-FeOOH), which is particularly readily removed in chemical washing.

At temperatures up to 100°C, it is desirable to use 08Kh14MF steel for facing structures. Under these conditions, its corrosion resistance is virtually equal to that of nickel stainless steels. At existing nuclear power stations, there are many large vessels made of scarce nickel-bearing steels (cooling and storage pools for fuel elements, emergency tanks, etc.). The use of 08Kh14MF steel, for example, for facing a single fuel-rod cooling and storage pond saves about 15-20 tons of Kh18N10T stainless steel.

TABLE 3. Corrosion Rates of 08Kh14MF Steel in Acid Solutions at 20°C Over 24 h

Acid	Concn. N	Corrosion rate, $g/m^2 \cdot h$	Acid	Concn., N	Corrosion rate, $g/m^2 \cdot h$
HNO$_3$	0,01	0,005	H$_2$SO$_4$	0,01	0,55
	0,1	0,067		0,1	6,79
	1,0	0,27		1,0	15,5
HCl	0,01	0,017	H$_2$C$_2$O$_4$	0,01	0,003
	0,1	2,81		0,1	0,004
	1,0	2,02		1,0	0,007
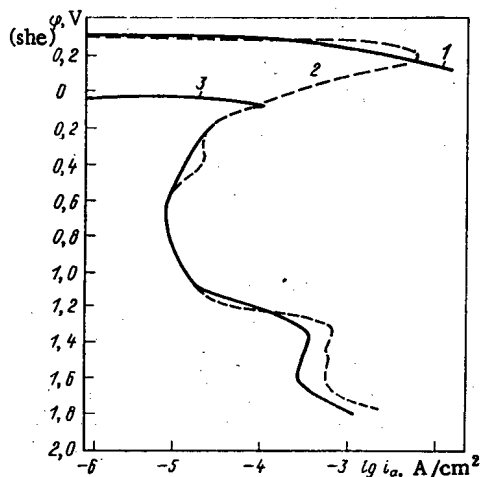
Fig. 1. Anodic polarization curves for 08Kh14MF steel in mineral acids: 1 N HCl (1); 1 N H$_2$SO$_4$ (2) and 1 N HNO$_3$ (3) at 20°C.

Tests have been performed under laboratory conditions on the corrosion resistance of steel in aqueous solutions similar in composition to the water in cooling and storage ponds for assemblies from power stations containing RBMK reactors [5, 6] at 20 ± 2 and 35 ± 5°C. The studies were made not only with specimens completely immersed in the solution but also with ones at the water—air interface. The areas of the specimens were 4-8 cm^2, solution volume 0.9 liter. During the tests lasting 4400 h in aqueous solutions containing 0-1 mg/liter of hydrogen peroxide and up to 10 mg/liter of chloride, the completely immersed specimens showed virtually no erosion. The mass change did not exceed the error of measurement (0.0002 g), while the corrosion rates were less than 0.0012 mg/m^2·day. The corrosion rate rises to 0.002 g/m^2·day when the chloride concentration is raised to 100 mg/liter. The surfaces after the corrosion tests were still lustrous and no superficial corrosion damage could be seen.

The specimens at the interface also showed no corrosion at chloride contents up to 10 mg/liter. When the concentration was raised to 50 mg/liter, some slight point corrosion occurred at the water line. On existing standards, the chloride concentrations in cooling and storage ponds for assemblies from nuclear power stations containing RBMK reactors [7] should not exceed 100 µg/liter. 08Kh14MF steels have high corrosion resistance under these conditions, and this is confirmed by tests on specimens in the cooling pond for the first block at Leningrad nuclear power station. Specimens of size 40 × 40 × 1 mm were used. The test time was 4680 h.

After the corrosion tests (Table 5), the appearance of the specimens was virtually unaltered, and there were no corrosion deposits. Specimens that had been in contact with 08Kh18N10T austenitic stainless steel (mounted on rods of this steel without insulation by PTFE film) corroded at rates 3-4 times less than with insulated specimens. Evidently, the chromium steel in a 08Kh14MF—08Kh18N10T galvanic pair has the more positive potential and the austenitic steel acts as anode.

215

TABLE 4. Test Results on Tube-Bundle Models for Heat Exchangers after Industrial Test (5000 h)*

Characteristics	Model 1		Model 2	
	tube space	intertube space	tube space	intertube space
Water quality and temp.	Aerated purified water, $T=30°C$	Deaerated purified water, $T=90°C$	Aerated purified water, $T=70°C$	Circuit water, $T=110°C$
Corrosion character and corrosion rate, mm/yr	St. 08Kh14MF, uniform, 0,0002 St. 20, pitting, 0,2—0,3	St. 08Kh14MF, uniform, 0,003. St. 20, pitting, 0,1—0,2	St. 08Kh14MF, uniform, 0,001 St. 20, pitting, 0,5—0,8	St. 08Kh14MF, uniform, 0,02—0,03 St. 20, pitting, 0,3—0,5
Deposited on tubes, g/m²	St. 08Kh14MF — 260 St. 20—1000	St. 08Kh14MF — 75 St. 20—250	St. 08Kh14MF — 80 St. 20—760	St. 08Kh14MF — 40 St. 20—1300
Deposit thickness on tubes, mm	St. 08Kh14MF — 0,35 St. 20—1—2	St. 08Kh14MF — 0,05 St. 20—0,4	St. 08Kh14MF — 0,10 St. 20—0,1—0,2	St. 08Kh14MF — 0,03 St. 20—0,8
Deposit composition	St. 08Kh14MF: 100% γ-FeOOH St. 20: 90% γ-FeOOH 10% Fe_3O_4	St. 08Kh14MF: 90% γ-FeOOH, 10% Fe_3O_4 St. 20: 80% γ-FeOOH 20% Fe_3O_4	St. 08Kh14MF: 100% γ-FeOOH St. 20: 40% γ-FeOOH. 10% Fe_2O_3	St. 08Kh14MF: 100% γ-FeOOH St. 20: 10% γ-FeOOH, 90% Fe_3O_4

*Results obtained by V. A. Shishkunov and A. A. Afanas'ev.

TABLE 5. Corrosion Rates of Reference Specimens Made of 08Kh14MF Steel in the Cooling Pond at Leningrad Nuclear Power Station

Treatment	Position in pond	Corrosion rate, g/m²·day
Mechanically cleaned	Vertical	$0,0019\pm0,0004$
	Horizontal	$0,0016\pm0,0004$
As supplied	Vertical	$0,0021\pm0,0004$
	Horizontal	$0,0016\pm0,0004$
As supplied in contact with 08Kh14MF steel	Vertical	$0,0004\pm0,0003$
	Horizontal	$0,0006\pm0,0003$
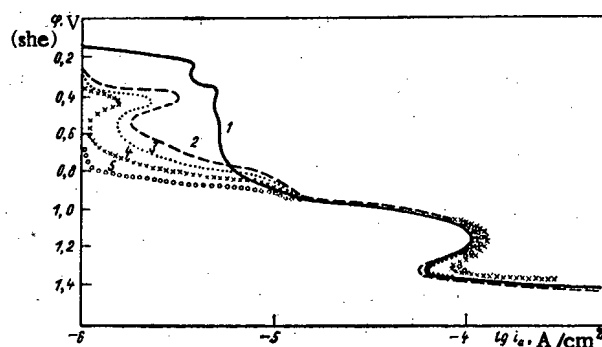
Fig. 2. Anodic polarization curves for 08Kh14MF steel in borate buffer after etching in 1 N H_2SO_4 for 24 h (1) and maintenance in distilled water at 20°C for 24 h (2), 50 (3), 120 (4), and 500 h (5).

216

The behavior of welded joints in 08Kh14MF steel was examined with specimens having two welds each. In one batch, automatic argon-arc welding was used with ÉP-955 and 07Kh25N13 rods, while in the other manual arc welding was used with electrodes based on these wires. The surfaces of the welds on removal from the cooling ponds showed thin friable films of lepidocrocite, which was readily removed with moist filter paper. There was no local corrosion damage at the weld itself and near it. The overall corrosion rate in the first batch was 0.0027 ± 0.0002 g/m²·day, while in the second it was 0.121 ± 0.0002 g/m²·day.

Therefore, these tests showed that 08Kh14MF steel can be recommended for general use as a basic constructional material for heat-exchanger equipment in nuclear power stations, combined heat and power stations, and heat sources working at temperatures from 70 to 350°C. The good corrosion resistance up to 100°C in aqueous media from various NPS units indicates that 08Kh14MF steel should be used as a facing material instead of nickel-bearing austenitic steels.

LITERATURE CITED

1. Ya. N. Kolotyrkin and E. A. Ul'yanin, Metalloved. Term. Obrab., No. 5, 2 (1981).
2. N. D. Tomashov, Zashch. Met., 17, No. 1, 16 (1981).
3. E. T. Dolbenko, L. P. Trusov, and I. R. Kryanin, Teploenergetika, No. 9, 2 (1980).
4. V. P. Borisov et al., Nickel-Free Stainless Chromium Steels in Soviet and Foreign Power Engineering [in Russian], No. 6-80-04, NIIÉINFORMÉNERGOmash., Moscow (1980).
5. V. M. Sedov et al., At. Energ., 47, No. 5, 294 (1979).
6. V. M. Sedov et al., ibid., 49, No. 4, 211 (1980).
7. V. M. Sedov et al., ibid., 51, No. 6, 380 (1981).

ANALYSIS OF THE LEAKAGE OF STEAM-WATER FLOW
WITH RUPTURE OF THE HEAT-CARRIER CIRCULATION
LOOP OF NUCLEAR REACTORS

Yu. V. Mironov and T. I. Fomicheva   UDC 621.039.586

In analyzing the safety of nuclear power plants, the sequence of hypothetical emergency situations associated with rupture of pipelines in the heat-carrier circulation loop is investigated. One of the main aspects of this research is the investigation of the thermohydraulic characteristics of heat-carrier motion in a damaged loop and the determination of the heat-carrier flow rate at the point of rupture.

For a channel reactor of RBMK type, analysis of a hypothetical emergency with heat-carrier loss in the rupture of a section with the technological channel has a series of distinctive features. First, emergencies in one channel do not lead to deep dynamic changes in the thermohydraulics of the reactor. In view of this, the boundary conditions at the ends of the emergency section remain approximately constant in the early stages of the emergency. This means that the situation may be investigated in a quasisteady approximation. Second, the section of the loop considered, including the technological channel, is a system of sufficiently long pipelines. With complete transverse rupture of the channel, critical conditions of leakage of the steam-water flow significantly limit the heat-carrier loss. However, local conditions determining the critical flow rate cannot be analyzed without complete calculation of the hydraulics of the whole of the considered section of the system, since the hydraulic pressure losses in this case are comparable with the losses on expansion in the vicinity of the critical cross section. At the same time, the dependence of the thermophysical properties of the two-phase medium on the local pressure over the length of the channel and the energy losses in expansion of the flow must be taken into account in detail.

The system of basic balance equations for some one-dimensional model of two-phase flow may be written in the following general form:

217
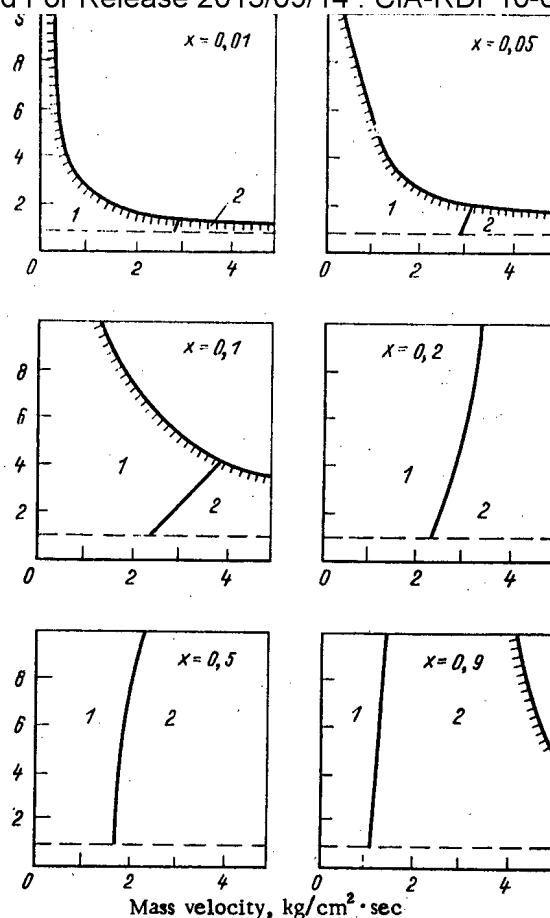
Fig. 1. Boundaries of correct formu-
lation of the thermohydraulic problem
for an equilibrium model of a two-
phase flow with a specified slip co-
efficient of the phases at a pressure
of 5 MPa: the continuous curve shows
the boundary of the region of correct-
ness (the shading is on the side of
the region of correctness); 1) sub-
sonic flow; 2) supersonic flow; S is the
slip coefficient, equal to the velocity
ratio of the steam and liquid phase
(the dashed line corresponds to S = 1).

$$A \frac{\partial u}{\partial t} + B \frac{\partial u}{\partial z} = f, \tag{1}$$

where t is the time; z is the coordinate over the channel length; u is the vector of unknowns
determining the flow; A and B are matrices with coefficients that are independent of the de-
rivatives of the components of vector u; f is the vector of the right-hand side.

As is known, mathematically correct formulation of the problem in Eq. (1), with a speci-
fied initial state of the flow in the channel, requires the existence, in the given set of
equations, of a complete set of real characteristics, the number of which is equal to the or-
der of the system in Eq. (1). The slope of these characteristics

$$\lambda = dz/dt \tag{2}$$

on the (z, t) plane is determined at each point from the solution of the following eigenvalue
problem:

$$\det (A\lambda - B) = 0. \tag{3}$$

The slope of the characteristics in Eq. (2) essentially determines the local velocity
of propagation of signals (small perturbations) in the flow. In connection with this, the

218
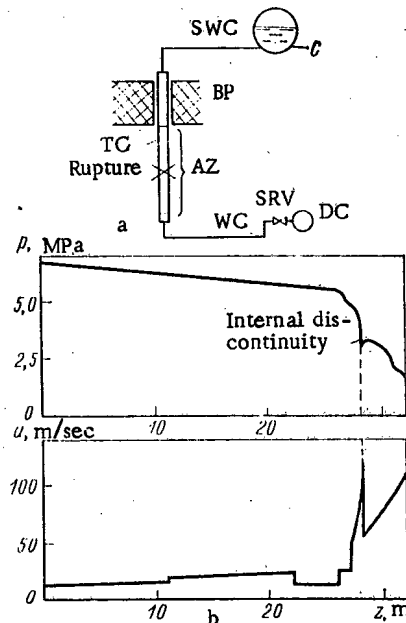
Fig. 2. Calculation by the
KRITIKA-3 program of a hypo-
thetical emergency situation
associated with rupture of
the technological channel:
a) diagram of the channel:
C, separator drum; SWC,
steam—water communication;
BP, biological protection;
TC, technological channel;
AZ, active zone; WC, water
communication; SRV, shut—off
and regulating valve; DC, dis-
tributing collector; b) pres-
sure distribution and velocity
of steam—water flow over the
length of the external part
of the emergency channel.

appearance of critical conditions of leakage, i.e., shutting—off of the flow when the ex-
ternal conditions at the output cease to affect the flow inside the channel, may ber inter-
preted as a situation in which the flow velocity in the output cross section of the channel
becomes equal to the maximum velocity of upstream propagation of the perturbations [1]. If
a similar situation arises for the given model of two—phase flow, all the eigenvalues of Eq.
(3) become nonnegative in the cross section at the output from the channel and, for at least
one of them, the following rigorous equality holds

$$\lambda_i = 0. \tag{4}$$

It follows from Eq. (4) that, in the critical cross section, the following condition
holds

$$\det (B) = 0. \tag{5}$$

For the steady variant of the system in Eq. (1), satisfaction of the condition in Eq.
(5) entails that the flow in the given cross section reaches a critical velocity. Thus, de-
termining the maximum steady flow rate through a long channel may be reduced to a nonlinear
boundary problem of specific form, when the condition in Eq. (5) is specified at the output
from the channel. The condition in Eq. (5) was used in precisely this form in [2] for a
thermodynamically equilibrium flow with slip, and in [3, 4] for more complex models of non-
equilibrium two—phase flow.

For long channels, as shown by a comparison of calculations and experiment in [2, 3],
the assumption of thermodynamic phase equilibrium allows the critical flow rate to be pre-

dicted sufficiently accurately. This is possible in the case where the heating of the water at the input is not too large, so that the balance steam content of the flow in the vicinity of the critical cross section is more than 2-4%. The idea of the channel length in this case is equivalent to the relaxation time of the thermodynamic processes in the two-phase medium. In experiments on small-diameter tubes (up to 10-20 mm), channels of length equal to more than 10-15 diameters may be regarded as sufficiently long. On passing to elements of a real heat-carrier circulation loop of a nuclear reactor, where the tube diameters are considerably larger, this threshold may evidently be reduced considerably. However, for components of small length, even in equilibrium flow, spatial effects play a pronounced role [5].

For a very low steam content in the critical cross section (for a volume steam content of less than ∿0.1), the equilibrium model gives values that are too low in comparison with the experimental results, with reasonable extrapolation of the experimental data on slip to the region of high mass velocity. In [6, 7], an attempt was made to compensate this discrepancy by means of fairly considerable slip coefficients of the phases in the critical cross section. On this basis, it proved possible to somewhat broaden the range of applicability of the equilibrium model in the region of low steam content. However, serious theoretical complications arise here. In Fig. 1, the boundaries of the correct formulation of the problem for the model of equilibrium two-phase flow with slip of the phases are shown. Beyond the boundaries of these regions, the eigenvalue problem in Eq. (3) has two complex-value roots, and the initial problem for Eq. (1) develops Hadamar instability. For a low steam content, with increase in mass velocity, this boundary approaches a slip of unity, whereas the slip coefficient corresponding to the given example for the dependence proposed in [7] is 3.12. For a steam content larger than 2-4%, the constraints on the slip coefficient are considerably weakened. But in this range, there is no practical necessity to correct the equilibrium model (at least for steady leaks from long pipelines).

Real progress in explaining these effects is achieved on dropping the hypothesis of thermodynamic phase equilibrium in the initial stages of boiling of the water flow. The hypothesis of metastable heating of the liquid phase, in combination with the semiempirical model of heterogeneous boiling of the water in [3], allows the experimental data on the leakage of hot water through an element of length greater than 3-4 diameters to be described with completely acceptable accuracy. The results of [8, 9], taking account of the existence of limiting metastable states of the liquid phase, led to the development of a physically well-founded model of critical flow conditions of a two-phase medium with a very low steam content, including the case of short nozzles and attachments.

For the present problem of analyzing the leakage of heat carrier with complete rupture of the pipeline from a section of the technological channel, the range of conditions in which metastability of the phases must be taken into account is extremely narrow (2-4% with respect to balanced steam content). For conditions in this range, considerable heating of the water before boiling at the entrance to the emergency channel is assumed; this is only characteristic of certain periods of shut-down cooling of the reactor. Thus, in most of the cases which are of practical interest, it is expedient to use the assumption of thermodynamic equilibrium of the two-phase flow. On this basis, the method proposed in [2] was realized in the KRITIKA-3 working program, written in Algol for a BÉSM-6 computer. This program is characterized by the following features:

it is intended for the calculation of part of the heat-carrier circulation loop composed of an arbitrary number of sections of different cross section, separated by point resistances calculated from the usual hydraulic relations;

at the input to the given channel, the pressure and heat content of the flow are specified;

at the output, the local pressure p satisfies the condition

$$p \geqslant p_a \qquad (6)$$

(p_a is the pressure of the surrounding medium), which, in combination with Eq. (5), allows the flow rate through the given channel to be determined in both purely hydraulic and critical conditions of leakage, by means of the selection method;

the thermodynamic properties of the water and steam at the saturation line and the heating of the water are specified in tabular form;

220

provision is made for the calculation of a section with a cross section that varies over the length (tapering nozzle), the parameters of which are specified in tabular form;

there is a special version of the program intended for the analysis of pipeline emergencies with superheated steam;

in the algorithm, provision is made for the possibility of shutting-off of the flow in some internal section of the channel, the condition in Eq. (5) being satisfied at the end of this section; the distribution of thermohydraulic flow parameters in the remainder of the channel is then calculated. The latter phenomenon may occur at a sudden expansion in cross section within the section being considered.

In terms of reaching critical conditions in the cross section preceding sudden expansion, the flow rate through the channel becomes that known from Eq. (5). The conditions at the output from the channel retain their previous form — Eqs. (5) and (6); at the input, i.e., at the internal critical cross section, only the stagnation enthalpy of the flow and the flow rate are regarded as specified, whereas the pressure is a variable parameter for the satisfaction of all the boundary conditions. Note that the program algorithm offers the possibility of calculating a system with an arbitrary number of internal discontinuities.

An example of how the KRITIKA-3 program may be used in analyzing hypothetical emergency situations associated with technological-channel rupture for a channel reactor of RBML type is shown in Fig. 2. These results correspond to the leakage of boiling water from a separator drum through the external branch of the emergency channel and the empty channel tube. In this situation, the critical cross section determining the heat-carrier flow rate from the separator drum is the sudden expansion in channel cross section on entering the empty technological channel, where there is an internal pressure discontinuity. The second discontinuity at the orifice of the broken technological channel corresponds to sonic emission of the two-phase flow into the surrounding medium.

Note, in conclusion, that the KRITIKA-3 program allows multivariant calculations of various emergency situations to be performed, with acceptable machine-time requirements, for nuclear reactors of channel type, providing the necessary information for the analysis of the consequences of such emergencies.

LITERATURE CITED

1. A. Tentner and J. Weisman, Nucl. Technol., 37, No. 1, 19 (1978).
2. Yu. V. Mironov, Teplofiz. Vys. Temp., 13, No. 1, 121 (1975).
3. Yu. V. Mironov, Vopr. At. Nauki Tekh., Ser. Reaktorostr., No. 1(8), 21 (1974).
4. A. I. Ivandaev and B. I. Nigmattulin, Teplofiz. Vys. Temp., 15, No. 3, 573 (1977).
5. I. Travis, C. Hirt, and W. Rivard, Nucl. Sci. Eng., 68, No. 3, 333 (1978).
6. H. Fauske, Nucl. Sci. Eng., 17, No. 1, 5 (1963).
7. F. Moody, J. Heat Transf., Trans. ASME Ser. C, No. 3, 57 (1966).
8. D. A. Khlestkin, A. S. Korshunov, and V. P. Kanishchev, Izv. Akad. Nauk SSSR, Energ. Trans., No. 5, 126 (1978).
9. D. A. Khlestkin, Izv. Akad. Nauk SSSR, Energ. Trans., No. 4, 147 (1979).

DYNAMIC MODEL OF A MIXTURE OF NONEQUILIBRIUM
STEAM—WATER FLOW, UNCONDENSED GAS, AND BORIC ACID

N. I. Kolev
<div align="right">UDC 621.039.534.2</div>

It is known that the heat carrier (water) of PWR and BWR reactors includes a known quantity of dissolved uncondensed gas (the true volume gas content is approximately 0.001–0.005 [1]) and also the solid phase, boric acid. In determining the critical density of the mass flow of heated heat carrier and the impact load on the equipment with desealing of the loop, the presence of gases dissolved in the liquid in the initial state is of great importance. Therefore, in modeling the transient and emergency conditions in the primary loop of atomic power plants and atomic heating stations, it must be taken into account that the heat-carrier components are flows of water (liquid or liquid and vapor or vapor), air, and boric acid. Taking account of the amount of uncondensed gas and boric-acid solid phase complicates the dynamic model.

In view of the complexity of realization of the model of such fluxes in program form it is important to develop a simple model with a minimum of simplifying assumptions. In the model of nonequilibrium flow realized in the RELAP-5 program [2], account is taken of the uncondensed gas and boric acid. However, it is assumed in the model that one of the phases is at the saturation line, and precisely which one, and the value of the true volume vapor content is determined. In the model, there is no agreement between the local conditions of appearance of critical flow conditions of three-phase flow and the assumptions made. There are works in which the presence of uncondensed gas is taken into account in the model of a homogeneous equilibrium flow [3], a homogeneous nonequilibrium flow [4], and an inhomogeneous equilibrium flow [5]. In these works, corresponding local conditions of the appearance of critical heat-carrier flow are formulated.

The aim of the present work is to construct a mathematical model of the dynamics of inhomogeneous nonequilibrium heat-carrier flow, in which the gaseous phases may be in an arbitrary stable or metastable state, while the solid phase is in thermodynamic and mechanical equilibrium with the liquid phase, and the local conditions for the appearance of critical heat-carrier flow are determined in accordance with the above assumptions.

Mathematical Model

In constructing the mathematical model of heat-carrier flow, the following assumptions are employed:

1) the liquid and gas phases are in an arbitrary stable or metastable state;

2) there is thermal equilibrium between the liquid and boric acid;

3) the uncondensed gas has the properties of an ideal gas;

4) for the water–vapor—ideal-gas mixture, Dalton's law holds;

5) the gas phase, if it exists, consists of water vapor or of water vapor and uncondensed gas;

6) the pressure of the liquid and gas phases is the same;

7) the velocity of the liquid and solid phases is the same;

8) the inequality of the gaseous and liquid velocities is taken into account using the empirical slip coefficient $S = w_g/w_F$, which is determined as a function of the local values of the dependent variables.

The following notation and relations are introduced, permitting considerable simplification of the description of the model:

$$p = p_L + p_D; \tag{1}$$

$$\rho_g = \rho_L + \rho_D; \tag{2}$$

$$v_g = 1/\rho_g; \tag{3}$$

$$\rho_F = \frac{\alpha_f}{1-\alpha}\rho_f + \frac{\alpha_B}{1-\alpha}\rho_B; \tag{4}$$

$$v_F = 1/\rho_F; \tag{5}$$

$$\rho = \alpha\rho_g + (1-\alpha)\rho_F; \tag{6}$$

$$G = \alpha\rho_g w_g + (1-\alpha)\rho_F w_f; \tag{7}$$

$$S = w_g/w_f; \tag{8}$$

$$x = \dot{m}_g/\dot{m}; \tag{9}$$

$$v_S = x v_g + S(1-x)v_F; \tag{10}$$

$$x_L = \dot{m}_L/\dot{m}; \tag{11}$$

$$x_B = \dot{m}_B/\dot{m}; \tag{12}$$

$$\bar{x}_L = \frac{x_L}{x-x_L}; \quad (x \neq 0; \ 0 \leqslant x_L < x); \tag{13}$$

$$T_g \rho_g ds_g = \rho_L dh_L + \rho_D dh_D - dp; \tag{14}$$

$$T_f \rho_F ds_F = \frac{\alpha_f}{1-\alpha}\rho_f dh_f + \frac{\alpha_B}{1-\alpha}\rho_B dh_B - dp; \tag{15}$$

$$\alpha = x v_g/v_S; \tag{16}$$

$$1-\alpha = S(1-x)v_F/v_S; \tag{17}$$

$$w_g = G v_S; \tag{18}$$

$$w_f = \frac{1}{S} G v_S; \tag{19}$$

$$\alpha\rho_L = x_L/v_S; \tag{20}$$

$$\alpha_B \rho_B = S x_B/v_S; \tag{21}$$

$$\rho_L = \rho_D \bar{x}_L; \tag{22}$$

$$v_I = \left[1 + x(1-x)\frac{(S-1)^2}{S}\right]/\rho; \tag{23}$$

$$s_g^* = \{\dot{q}_g'' + \mu[h_{ex} - h_D + \Delta w_g(\bar{w}_g - w_g)]\}/T_g; \tag{24}$$

$$S_F^* = \{\dot{q}_F'' - \mu[h_{ex} - h_f + \Delta w_f(\bar{w}_f - w_f)]\}/T_f; \tag{25}$$

$$v_S = [S - x(S-1)]/\rho; \tag{26}$$

$$S - \text{const.} \tag{27}$$

The equations of mass, momentum, and energy conservation for each phase and component separately are taken as the starting point:

$$\frac{\partial}{\partial\tau}(\alpha\rho_L A) + \frac{\partial}{\partial z}(\alpha\rho_L w_g A) = 0; \tag{28}$$

$$\frac{\partial}{\partial\tau}(\alpha\rho_D A) + \frac{\partial}{\partial z}(\alpha\rho_D w_g A) = \mu A; \tag{29}$$

$$\frac{\partial}{\partial\tau}(\alpha_f\rho_f A) + \frac{\partial}{\partial z}(\alpha_f\rho_f w_f A) = -\mu A; \tag{30}$$

$$\frac{\partial}{\partial\tau}(\alpha_B\rho_B A) + \frac{\partial}{\partial z}\alpha_B\rho_B w_f A) = 0; \tag{31}$$

$$\frac{\partial}{\partial\tau}(\alpha\rho_L w_g A) + \frac{\partial}{\partial z}(\alpha\rho_L w_g^2 A) + \alpha A\frac{\partial p_L}{\partial z} + \alpha\rho_L g A\cos\varphi + \frac{F_{RL}}{\Delta z} = 0; \tag{32}$$

$$\frac{\partial}{\partial\tau}(\alpha\rho_D w_g A) + \frac{\partial}{\partial z}(\alpha\rho_D w_g^2 A) + \alpha A\frac{\partial p_D}{\partial z} + \alpha\rho_D g A\cos\varphi + \frac{F_{RD}}{\Delta z} = \mu w_{ex} A; \tag{33}$$

$$\frac{\partial}{\partial\tau}(\alpha_f\rho_f w_f A) + \frac{\partial}{\partial z}(\alpha_f\rho_f w_f^2 A) + \alpha_f A\frac{\partial p}{\partial z} + \alpha_f\rho_f g A\cos\varphi + \frac{F_{Pf}}{\Delta z} = -\mu w_{ex} A; \tag{34}$$

$$\frac{\partial}{\partial\tau}(\alpha_B\rho_B w_f A) + \frac{\partial}{\partial z}(\alpha_B\rho_B w_f^2 A) + \alpha_B A\frac{\partial p}{\partial z} + \alpha_B\rho_B g A\cos\varphi + \frac{F_{RB}}{\Delta z} = 0; \tag{35}$$

$$\frac{\partial}{\partial\tau}\left[\alpha\rho_L\left(u_L\frac{w_g^2}{2}\right)A\right] + \frac{\partial}{\partial z}\left[\alpha\rho_L w_g\left(h_L + \frac{w_g^2}{2}\right)A\right] + \alpha\rho_L w_g A g\cos\varphi + \frac{E_{RL}}{\Delta z}w_g = \frac{\dot{Q}_L}{\Delta z}; \tag{36}$$

223

$$\frac{\partial}{\partial \tau}\left[\alpha\rho_D\left(u_D+\frac{w_g^2}{2}\right)A\right]+\frac{\partial}{\partial z}\left[\alpha\rho_D w_g\left(h_D+\frac{w_g^2}{2}\right)A\right]+\alpha\rho_D w_g Ag\cos\varphi+\frac{F_{RD}}{\Delta z}w_g=\frac{\dot{Q}_D}{\Delta z}+\mu\left(h_{ex}+\frac{w_{ex}^2}{2}\right)A; \tag{37}$$

$$\frac{\partial}{\partial \tau}\left[\alpha_f\rho_f\left(u_f+\frac{w_f^2}{2}\right)A\right]+\frac{\partial}{\partial z}\left[\alpha_f\rho_f w_f\left(h_f+\frac{w_f^2}{2}\right)A\right]+\alpha_f\rho_f w_f Ag\cos\varphi+\frac{F_{Rf}}{\Delta z}w_f=\frac{\dot{Q}_f}{\Delta z}-\mu\left(h_{ex}+\frac{w_{ex}^2}{2}\right)A; \tag{38}$$

$$\frac{\partial}{\partial \tau}\left[\alpha_B\rho_B\left(u_B+\frac{w_f^2}{2}\right)A\right]+\frac{\partial}{\partial z}\left[\alpha_B\rho_B w_f\left(h_B+\frac{w_f^2}{2}\right)A\right]+\alpha_B\rho_B w_f Ag\cos\varphi+\frac{F_{RB}}{\Delta z}w_f=\frac{\dot{Q}_B}{\Delta z}. \tag{39}$$

The equations of momentum and energy conservation are differentiated so as to obtain the left-hand side of the mass-conservation equation. The corresponding right-hand side of the mass-conservation equation is replaced, to give

$$\alpha\rho_L\left(\frac{\partial w_g}{\partial \tau}+w_g\frac{\partial w_g}{\partial z}\right)+\alpha\frac{\partial p_L}{\partial z}+\alpha\rho_L g\cos\varphi+f_{RL}=0; \tag{40}$$

$$\alpha\rho_D\left(\frac{\partial w_g}{\partial \tau}+w_g\frac{\partial w_g}{\partial z}\right)+\alpha\frac{\partial p_D}{\partial z}+\alpha\rho_D g\cos\varphi+f_{RD}=\mu\left(w_{ex}-w_g\right); \tag{41}$$

$$\alpha_f\rho_f\left(\frac{\partial w_f}{\partial \tau}+w_f\frac{\partial w_f}{\partial z}\right)+\alpha_f\frac{\partial p}{\partial z}+\alpha_f\rho_f g\cos\varphi+f_{Rf}=-\mu\left(w_{ex}-w_f\right); \tag{42}$$

$$\alpha_B\rho_B\left(\frac{\partial w_f}{\partial \tau}+w_f\frac{\partial w_f}{\partial z}\right)+\alpha_B\frac{\partial p}{\partial z}+\alpha_B\rho_B g\cos\varphi+f_{RB}=0; \tag{43}$$

$$\alpha\rho_L\left(\frac{\partial h_L}{\partial \tau}+w_g\frac{\partial h_L}{\partial z}\right)+\alpha\rho_L w_g\left(\frac{\partial w_g}{\partial \tau}+w_g\frac{\partial w_g}{\partial z}\right)-\frac{\partial}{\partial \tau}(\alpha p_L)+w_g(\alpha\rho_L g\cos\varphi+f_{RL})=\dot{q}_L'''; \tag{44}$$

$$\alpha\rho_D\left(\frac{\partial h_D}{\partial \tau}+w_g\frac{\partial h_D}{\partial z}\right)+\alpha\rho_D w_g\left(\frac{\partial w_g}{\partial \tau}+w_g\frac{\partial w_g}{\partial z}\right)-\frac{\partial}{\partial \tau}(\alpha p_D)+w_g(\alpha\rho_D g\cos\varphi+f_{RD})=\dot{q}_D'''+\mu\left(h_{ex}+\frac{w_{ex}^2}{2}-h_D-\frac{w_g^2}{2}\right); \tag{45}$$

$$\alpha_f\rho_f\left(\frac{\partial h_f}{\partial \tau}+w_f\frac{\partial h_f}{\partial z}\right)+\alpha_f\rho_f w_f\left(\frac{\partial w_f}{\partial \tau}+w_f\frac{\partial w_f}{\partial z}\right)-\frac{\partial}{\partial \tau}(\alpha_f p)+w_f(\alpha_f\rho_f g\cos\varphi+f_{Rf})=\dot{q}_f'''-\mu\left(h_{ex}+\frac{w_{ex}^2}{2}-h_f-\frac{w_f^2}{2}\right); \tag{46}$$

$$\alpha_b\rho_B\left(\frac{\partial h_B}{\partial \tau}+w_f\frac{\partial h_B}{\partial z}\right)+\alpha_B\rho_B w_f\left(\frac{\partial w_f}{\partial \tau}+w_f\frac{\partial w_f}{\partial z}\right)-\frac{\partial}{\partial \tau}(\alpha_B p)+w_f(\alpha_B\rho_B g\cos\varphi+f_{RB})=\dot{q}_B'''. \tag{47}$$

By algebraic manipulations, on the basis of the above notation and relations but without taking account of the components of the entropy change $-p(\partial\alpha/\partial z)/T_g$, $+p(\partial\alpha/\partial z)/T_f$, a system of equations with one time derivative in each is obtained:

$$\frac{\partial\rho}{\partial \tau}+\frac{1}{A}\frac{\partial}{\partial z}(GA)=0; \tag{48}$$

$$\frac{\partial x}{\partial \tau}+Gv_g\frac{S-x(S-1)}{S}\frac{\partial x}{\partial z}=\frac{S-x(S-1)}{S}v_g\left[\mu-x(1-x)\frac{S-1}{S-x(S-1)}\frac{1}{A}\frac{\partial}{\partial z}(GA)\right]; \tag{49}$$

$$\frac{\partial x_L}{\partial \tau}+Gv_g\frac{\partial x_L}{\partial z}=-x_L\frac{S-1}{S}v_g\left[\mu-G\frac{\partial x}{\partial z}+(1-x)\frac{1}{A}\frac{\partial}{\partial z}(GA)\right]; \tag{50}$$

$$\frac{\partial x_B}{\partial \tau}+\frac{1}{S}Gv_g\frac{\partial x_B}{\partial z}=-x_B\frac{S-1}{S}v_g\left[\mu-G\frac{\partial x}{\partial z}-x\frac{1}{A}\frac{\partial}{\partial z}(GA)\right]; \tag{51}$$

$$\frac{\partial G}{\partial \tau}+2Gv_I\frac{\partial G}{\partial z}=-\frac{G^2}{A}\frac{\partial}{\partial z}(v_I A)-\frac{\partial p}{\partial z}-Z; \tag{52}$$

$$\frac{\partial s_g}{\partial \tau}+Gv_g\frac{\partial s_g}{\partial z}=s_g^*v_g/x,\quad x\neq 0; \tag{53}$$

$$\frac{\partial s_F}{\partial \tau}+\frac{1}{S}Gv_g\frac{\partial s_F}{\partial z}=s_F^*v_g/[S(1-x)],\quad(1-x)\neq 0. \tag{54}$$

Numerical Integration of the System of Differential Equations

The auxiliary dependent-variable vector is taken in the form

$$\mathbf{U}^T=(G,\rho,x,x_L,x_B,s_g,s_F). \tag{55}$$

Consider a heat-carrier circulation loop of length L, divided into J — 1 sections over the length. The subscript j denotes the spatial position and the superscript n the time position. The equation of momentum conservation — Eq. (52) — may be integrated using an explicit or semiexplicit scheme if $(p, v_I, z, G)_j^n$, p_1^{n+1}, p_j^{n+1} are known. As a result, $G_j^{n+1}(j=1, j)$

224

TABLE 1. Partial Derivatives of the Air Pressure and Gas Density

Y	$(\partial Y/\partial T_g)_{p,\bar{x}_L}$	$(\partial Y/\partial p)_{T_g,\bar{x}_L}$	$(\partial Y/\partial \bar{x}_L)_{p,T_g}$
$p_L = \bar{x}_L R_L T_g \rho_D$	$\bar{x}_L R_L \dfrac{\rho_D + T_g \frac{\partial \rho_D}{\partial T_g}}{1 + \bar{x}_L R_L T_g \frac{\partial \rho_D}{\partial p_D}}$	$\bar{x}_D R_L \dfrac{T_g \frac{\partial \rho_D}{\partial p_D}}{1 + \bar{x}_L R_L T_g \frac{\partial \rho_D}{\partial p_D}}$	$\dfrac{\rho_D R_L T_g}{1 + \bar{x}_L R_L T_g \frac{\partial \rho_D}{\partial p_D}}$
$\rho_g = (1 + \bar{x}_L)\,\rho_D$	$(1 + \bar{x}_L)\left(\dfrac{\partial \rho_D}{\partial T_g} - \dfrac{\partial \rho_D}{\partial p_D}\dfrac{\partial p_L}{\partial T_g}\right)$	$(1 + \bar{x}_L)\dfrac{\partial \rho_D}{\partial p_D}\left(1 - \dfrac{\partial p_L}{\partial p}\right)$	$\rho_D - (1 + \bar{x}_L)\dfrac{\partial \rho_D \partial p_L}{\partial p_D \partial \bar{x}_L}$
$v_g = 1/\rho_g$	$-\dfrac{1}{\rho_g^2}\dfrac{\partial \rho_g}{\partial T_g}$	$-\dfrac{1}{\rho_g^2}\dfrac{\partial \rho_g}{\partial p}$	$-\dfrac{1}{\rho_g^2}\dfrac{\partial \rho_g}{\partial \bar{x}_L}$

is obtained. Using the result for G_j^{n+1}, it is simple to find all the increments of the vector U:

$$(\delta U)_j^T = (U_j^{n+1} - U_j^n)^T = (\delta G,\ \delta\rho,\ \delta x,\ \delta x_L,\ \delta x_B,\ \delta s_g,\ \delta s_F). \tag{56}$$

Explicit or implicit schemes may be used for this purpose, with the following order of integration of the equations: Eqs. (48), (49), (50), (51), (53), (54). If the discretization scheme is of second-order accuracy, a tridiagonal matrix is formed for each equation in the implicit method; this matrix may be transformed using recurrence relations. Thus, the transformation of higher-order matrices is eliminated, and less machine memory and machine time is required.

The principal dependent-variable vector is chosen in the form

$$U^T = (G,\ p,\ x,\ x_L,\ x_B,\ T_g,\ T_f). \tag{57}$$

Using the equations of state given below, the following transformation is made

$$\delta U = M\delta U. \tag{58}$$

Hence, the values of U in the new time plane are obtained

$$U_j^{n+1} = U_j^n + \delta U_j, \quad j = 1,\ J. \tag{59}$$

Equations of State

The derivation of the equations of state is too cumbersome, and so only the final result is given here

$$dp = f_0 G^{*2}\left[x\left(\frac{\partial v_g}{\partial T_g}\frac{T_g \bar{ds}_g}{c_{pg}} + \frac{\partial v_g}{\partial x_L}\,d\bar{x}_L\right) + S(1-x)\frac{\partial v_F}{\partial T_f}\frac{T_f ds_F}{c_{pF}} - \Delta\right]; \tag{60}$$

where

$$\bar{ds}_g = ds_g + \frac{\rho_D}{T_g \rho_g}\frac{\partial h_D}{\partial p_D}\frac{\partial p_L}{\partial \bar{x}_L}\,d\bar{x}_L; \tag{61}$$

$$d\bar{x}_L = (x\,dx_L - x_L\,dx)/(x - x_L)^2; \tag{62}$$

$$\Delta = -\frac{v_S}{\rho}\,d\rho - \left[\frac{S-1}{\rho} - \frac{\partial v_S}{\partial x}\right]dx;\quad \frac{\partial v_S}{\partial x} = v - Sv_f; \tag{63}$$

$$dT_g = -\frac{\rho_g(\partial h_g/\partial p) - 1}{\rho_g c_{pg}}\,dp + \frac{T_g ds_g}{c_{pg}}; \tag{64}$$

$$dT_f = -\frac{\rho_f(\partial h_f/\partial p) - 1}{\rho_F c_{pF}}\,dp + \frac{T_f ds_F}{c_{pF}}; \tag{65}$$

$$\rho_g c_{pg} = \rho_L c_{pL} + \rho_D\left(c_{pD} - \frac{\partial h_D}{\partial p_D}\frac{\partial p_L}{\partial T_g}\right); \tag{66}$$

$$\rho_F c_{pF} = \rho_f c_{pf} + \rho_B c_{pB}; \tag{67}$$

$$\rho_g \frac{\partial h_g}{\partial p} = \rho_D \frac{\partial h_D}{\partial p_D}\left(1 - \frac{\partial p_L}{\partial p}\right); \tag{68}$$

$$1/G^{*2} = f_0\left[\frac{x}{G_g^{*2}} + \frac{S(1-x)}{G_g^{*2}}\right]; \tag{69}$$

225

$$f_0 = \frac{1 + x(S-1)}{S}.\tag{70}$$

Here G^* is the local critical flux density and

$$\frac{1}{G_i^{*2}} = \frac{\partial v_i}{\partial p} + \frac{\partial v_i}{\partial T_i} \frac{\rho_i(\partial h_i/\partial p) - 1}{\rho_i c_{p_i}},\tag{71}$$

where

$$i = g, F,\tag{72}$$

determines the local values of the critical mass-flux density for the gas phase and for a mixture of liquid + solid phase (water + boric acid), respectively. The necessary derivatives of p_L and v_g are shown in Table 1.

Steady State

Consider the local conditions for the appearance of critical flow. For the steady state, from Eqs. (48)-(54), the following result is obtained using the vector U^T as the dependent-variable vector and the above notation and relations

$$GA = \text{const};\tag{73}$$

$$\frac{dx}{dz} = \mu/G;\tag{74}$$

$$x_L = \text{const};\tag{75}$$

$$x_B = \text{const};\tag{76}$$

$$\frac{dp}{dz} = \left[-Z + G^2 v_I \frac{1}{A}\frac{dA}{dz} - G\left(f_0 G \frac{d\Delta_1}{dz} + \mu \frac{\partial v_I}{\partial x}\right)\right]\Big/(1 - G^2/G^{*2});\tag{77}$$

$$\frac{\partial v_I}{\partial x} = \frac{S-1}{S} v_g + f_0(v_g - S v_F);\tag{78}$$

$$G \frac{d\Delta_1}{\partial z} = \frac{\partial v_g}{\partial T_g}\frac{T_g s_g^*}{c_{pg}} + S\frac{\partial v_f}{\partial T_f}\frac{T_f s_F^*}{c_{pF}} - \mu\frac{x x_L}{(x - x_L)^2}\left(\frac{\partial v_g}{\partial x_L} + \frac{\partial v_L}{\partial T_g}\frac{\rho_D}{\rho_g c_{pg}}\frac{\partial h_D}{\partial p_D}\frac{\partial p_L}{\partial x_L}\right);\tag{79}$$

$$\frac{dT_g}{dz} = -\frac{\rho_g(\partial h_g/\partial p) - 1}{\rho_g c_{pg}}\frac{dp}{dz} + \frac{T_g \widetilde{ds}_g/dz}{c_{pg}};\tag{80}$$

$$\frac{dT_f}{dz} = -\frac{\rho_f(\partial h_f/\partial p) - 1}{\rho_F c_{pF}}\frac{dp}{dz} + \frac{T_f ds_F/dz}{c_{pF}}.\tag{81}$$

It is evident from Eq. (77) that the local condition for the appearance of critical flow may be denoted by

$$G = G^* \ (dp \rightarrow -\infty).\tag{82}$$

Conclusions

The system in Eqs. (48)-(54) has a series of advantages. Two are that it is simple and continuous on passing through phase boundaries. In the case where an explicit scheme is used for the integration of Eqs. (53)-(54), the spatial derivative of the entropy may be calculated from the equation of state for the entropy with known temperature and pressure, employing the usual set of approximations of the thermodynamic properties for the individual phases and components, which leads to considerable economy of computer time.

The system in Eqs. (48)-(54) as well as Eqs. (60), (64), (65), (69), (74), (78), (79), and (83) and the steady system in Eqs. (73)-(81) satisfactorily reproduces the limiting case of lack of uncondensed gas or gas phase or liquid and solid phase. Note that the given model does not work in the limiting case of a flow of uncondensed gas or of uncondensed gas and liquid in accordance with the assumptions; see the section on the mathematical model. The explanation for this is that the equations of state of the mixture were derived using Eq. (22), which is not defined for this case. However, it must be taken into account that, in the presence of the gas phase, a known amount of vapor is always present; this means that the model is applicable in many practical cases.

NOTATION

A, area; c_p, specific heat; F_R, frictional force; f_R, frictional force of the phase or component per unit volume of flow; G, mass flux density; G^*, critical mass flux density; g, acceleration due to gravity; h, specific enthalpy; M, mass; $\dot{m}$, mass flow rate; p, pressure; Q, thermal power; $\dot{q}'''$, thermal power per unit volume of flow; R_L, gas constant of air; R,

226

frictional force of the flow as a whole per unit volume of flow; S, slip coefficient; s, specific entropy; T, absolute temperature; U, dependent-variable vector; $\underline{u}$, specific internal energy; v, specific volume; w, velocity; $\Delta w_f = w_{ex} - w_f$; $\Delta w_g = w_{ex} - w_g$; $\overline{w}_f = (w_{ex} + w_f)/2$; $\overline{w}_g = (w_{ex} + w_f)/2$; $Z = f_R + \rho g \cos \varphi$; x, mass flow-rate gas content; z, linear coordinate; φ, angular coordinate; α, volume gas content; μ, rate of phase transition; μ, density; τ, time; d, ∂, total and partial differentials. Indices: L, air; D, vapor; B, boric acid; f, water; F, water + boric acid; g, gas; ex, phase returning the mass.

LITERATURE CITED

1. D. Malnes and K. Solberg, Fundamental Solution of the Critical Two-Phase Flow Problem, Applicable to Loss-of-Coolant Accident Analysis, Institute for Atomic Energy (1973), SD-119.
2. V. Ransom et al., RELAP 5/MOD1 Code Manual, Vol. 1, System Models and Numerical Methods, EG&G, Idaho (March 1981), NUREG/CR-1926, EGG-2070.
3. N. I. Kolev, Nucl. Sci. Eng., 85, 209 (1983).
4. N. I. Kolev, Atomkernenerg., 42, No. 3, 201 (1983).
5. N. I. Kolev, Nucl. Eng. Design, 74, 265 (1983).

PASSIVE STABILIZATION OF VERTICAL INSTABILITY
IN A TOKAMAK REACTOR

S. G. Bespoludennov, S. A. Galkin,
L. M. Degtyarev, and V. I. Pistunovich

In the thermonuclear tokamak reactors being designed at the present time, the plasma has a cross section which is elongated in the vertical direction. The elongation permits increasing the limiting pressure of the plasma and the plasma volume for a specified value of the stability reserve q as well as economically utilizing the space inside the D-shaped toroidal coils (the D-shape of the coils is caused by minimization of the mechanical stresses in them when a high current is flowing). The presence of a poloidal diverter in a tokamak reactor can also lead to an elongation of the plasma filament. However, the configuration of the poloidal field which permits forming an elongated D-shaped cross section is unstable with respect to vertical shifts of the plasma. The forces elongating the plasma cross section tend to increase a small shift from the equilibrium position without limit. In the absence of a plasma sheath or other stabilizing elements this instability develops in Alfvén times (the instability increment $\gamma \approx 10^6$ sec^{-1}).

In order not to permit deviations of the plasma from the equilibrium position of more than 3-5 cm, it is necessary to use a system of active feedback which reacts to a shift of the plasma. The currents in the active coupling loops should create a compensating field which returns the plasma to its original state. The rate of growth of the controlling field is determined both by the characteristics of the active system itself and by the time for it to penetrate through the conducting structures between the plasma and the loops. It is assumed at present that the slave system will be able to catch the plasma and control its position in 50-100 msec after the start of a shift. Therefore the instability increment should not exceed 20-10 sec^{-1}. Such a value of γ can be expected in the presence of passive feedback, i.e., currents which are induced in the conducting structures upon a shift of the plasma. The first wall, blanket, and shielding of the reactor as well as the conducting structures specially used to suppress rapid vertical instability can serve as the elements of such a system. Thus at INTOR they use aluminum loops 6-10 cm in radius separated in the toroidal direction by frames (INTOR, Phase One, Vienna, 1982, p. 109) with this aim. The passive stabilization system should not significantly decrease the flux of neutrons from the plasma into the blanket; therefore the alternative of using the structures of the blanket itself for stabilization seems very attractive. The results of a numerical investigation of instability stabilization using a case with an effective thickness of 5 cm to simulate the first wall of the reactor and the blanket are given in this paper.
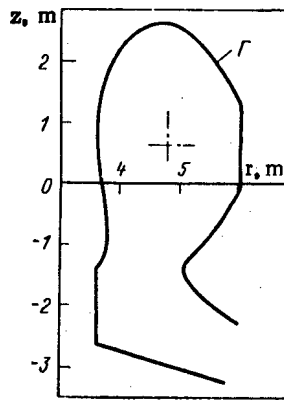
Fig. 1. Configuration of the case Γ formed by the first wall of the tokamak reactor and the lithium layer of the blanket.
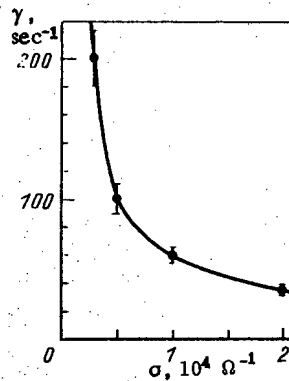
Fig. 2. Dependence of the vertical instability increment γ on the linear conductivity of the case σ.

The stabilization problem is investigated in the approximation of a rigid shift of the plasma filament. A toroidal coordinate system (r, φ, z) is introduced. In the following we shall use the symmetry in the toroidal angle φ. We shall simulate the plasma with a filamentary current I_p having the coordinates $[r_p, z_p(t)]$. We shall assume that the plasma loop can undergo only vertical shifts $\xi = (0, 0, \xi)$. Variation of the poloidal magnetic flux upon a shift of the plasma is cause for the appearance in the case of an emf in the toroidal direction which one can express in the thin-case approximation in terms of the electric field intensity:

$$\mathcal{E}(r, z, t) = \oint E(r, z, t) \, r d\varphi = 2\pi r E(r, z, t), \tag{1}$$

where r and z are the coordinates of the case Γ (Fig. 1).

Having made use of Ohm's law, we obtain an equation for the linear density of the currents induced in the case:

$$i(r, z, t) = -\frac{\sigma}{r} \frac{\partial \psi(r, z, t)}{\partial t}. \tag{2}$$

The poloidal magnetic flux ψ at any point of the case is comprised of the flux

$$\psi_p = \mu_0 I_p G(r, z; r_p, z_p), \tag{3}$$

228

TABLE 1. Coordinates of the Equilibrium Coils and the Currents in Them

Parameter	Coil number									
	1	2	3	4	5	6	7	8	9	10
r, m	11,5	7,5	3,0	1,2	1,2	1,2	1,2	3,0	7,5	11,5
z, m	5,0	7,0	7,0	3,25	1,0	−1,2	−3,35	−7,2	−7,0	−5,5
I, MA	0,05	−2,05	1,8	8,0	−18,2	−16,55	12,25	18,7	14,0	−22,3

created by the plasma loop, the flux

$$\psi\mathrm{r} = \mu_0 \int_\Gamma i\,(r',\ z',\ t)\,G\,(r,\ z;\ r',\ z')\,dl', \tag{4}$$

which arises due to the induced currents, and the flux ψ_{equil} caused by the external equilibrium currents. The function $G(r,\ z;\ r',\ z')$ determines the field of a single loop with the current

$$G\,(r,\ z;\ r',\ z') = \frac{\sqrt{rr'}}{\pi\rho}\left[\left(1 - \frac{\rho^2}{2}\right)K\,(\rho) - E\,(\rho)\right];$$

$$\rho^2 = \frac{4rr'}{(r+r')^2 + (z-z')^2}\,. \tag{5}$$

Here $K(\rho)$ and $E(\rho)$ are the complete elliptical integrals of the first and second kind. Since the equilibrium loops are located far from the plasma and are shielded by the blanket, the shielding, and the cryostat, the currents induced in them upon a shift of the plasma are negligibly small. Therefore we shall assume that ψ_{equil} does not vary in time.

Having combined expressions (2)–(4) on the assumption of the constancy of the plasma current I_p, we obtain the following integrodifferential equation:

$$i\,(r,\ z,\ t) = -\frac{\mu_0 \sigma I_p}{r}\frac{\partial G\,(r,\ z;\ r_p z_p)}{\partial z_p}\frac{\partial \xi}{\partial t} - \frac{\mu_0 \sigma}{r}\int_\Gamma \frac{\partial i\,(r',\ z',\ t)}{\partial t}\,G\,(r,\ z;\ r',\ z')\,dl', \tag{6}$$

where σ is the conductivity of a unit length of the case Γ, i.e., the product of the specific conductivity by the case thickness.

The shift of the plasma $\xi(t)$ satisfies the equation

$$m_p\frac{\partial^2 \xi}{\partial t^2} = F_1 + F_2, \tag{7}$$

where m_p is the mass of the plasma and F_1 is the force acting on the plasma on the part of the poloidal restraining field upon deviations from the equilibrium position. Its value is determined by the radial component of the magnetic field created by the currents I_i at the point $[r_p,\ z_p(t) = z_{p0} + \xi(t)]$, at which a plasma filament with the current I_p is located:

$$F_1 = 2\pi r I_p B_r = 2\pi\mu_0 I_p\sum_{i=1}^{N} I_i\frac{\partial G\,(r_i,\ z_i;\ r_p,\ z_p)}{\partial z_p}\,. \tag{8}$$

Here $(r_i,\ z_i)$, $i = 1, 2, \ldots, N$ are the coordinates of the equilibrium coils I_i. The restoring force F_2 is determined by the Foucault currents in the case:

$$F_2 = 2\pi\mu_0 I_p\int_\Gamma i\,(r',\ z',\ t)\frac{\partial G\,(r',\ z';\ r_p z_p)}{\partial z_p}\,dl'. \tag{9}$$

The system of equations (5)–(9) is closed and is numerically integrated to determine the dependence of the vertical shift ξ on time. The algorithm for the numerical solution of the system (5)–(9) consists of successively finding the induced currents from the solution of Eq. (6) and calculating the forces from the expressions (8) and (9) and the shift ξ from Eq. (7). The matrix of the difference analogue of Eq. (6) is inverted by Gauss' method with the selection of the principal element; at each time step iterations are provided for refinement of the unknown quantities.

229

Knowing how the position of the plasma varies in time, one can estimate the instability increment γ by the formula

$$\xi(t) = \xi_0 e^{\gamma(t-t_0)},\qquad(10)$$

where ξ_0 is the shift of the plasma at time t_0.

The following parameters were used in the calculations of the vertical instability of the plasma in the reactor: plasma current I_p = 5.4 MA, coordinates of the equilibrium position of the plasma r_p = 4.8 m, z_{p0} = 0.581 m (the z-coordinate was figured from the center of the toroidal coil), and mass of the plasma m_p = 10^{-4} kg. The coordinates of the equilibrium of the coils and the values of the current in them are given in Table 1.

In the induction method of maintaining the current in the plasma filament the resistance of the conducting structures surrounding the plasma should be no less than a specified value; therefore one can obtain an upper limit for the conductivity of the case. For the case shown in Fig. 1 R_{cr} = 0.2 mΩ corresponds to σ_{cr} = $1.1 \cdot 10^4$ Ω^{-1} (for a case thickness of 5 cm its specific conductivity should not exceed $2.2 \cdot 10^5$ $\Omega^{-1} \cdot m^{-1}$). The dependence of the instability increment γ on the case conductivity is given in Fig. 2. The error in the determination of the increment is caused by the fact that the dependence $\xi(t)$ as found from the calculation is only approximately of an exponential nature. The values of γ calculated from formula (10) are different at the different times t_0 and t. The error in all the calculations does not exceed 10%, which is reflected in Fig. 2. Even with σ = $2 \cdot 10^4$ Ω^{-1} the value of the increment remains at the level of 35 sec^{-1}. We note that the calculated points are located with good accuracy on the straight line log γ = 5.5 $-$ 0.9 logσ.

The calculations performed permit concluding that the structure of the first wall and the blanket with an effective conductivity σ = $(2-1) \cdot 10^4$ Ω^{-1} decreases the increment of the development of vertical instability to the value γ = 30-60 sec^{-1}. This permits us to do without additional structures of passive feedback. However, the active feedback system should provide a response speed of 30-15 msec. According to the estimate, the rate of penetration of the field from the active feedback coils through the case is $\sim$5 msec, which is sufficient to provide for control of vertical instability of plasma in the reactor.

THERMAL-NEUTRON FISSION CROSS SECTION OF THE SHORT-LIVED

ISOMER OF ^{236}Np

E. A. Gromova, S. S. Kovalenko,
Yu. A. Nemilov, Yu. A. Selitskii,
A. V. Stepanov, A. M. Fridkin,
V. B. Funshtein, V. A. Yakovlev,
G. V. Val'skii, and G. A. Petrov

In nuclear reactors (particularly in fast reactors) ^{236}Np is formed in the reaction ^{237}Np(n, 2n)^{236}Np in two states: long-lived ^{236}Np(l) with a half-life $T_{1/2}$ = $1.55 \cdot 10^5$ yr [1], and short-lived ^{236}Np(s) with $T_{1/2}$ = 22.5 ± 0.4 h [2]. The ^{236}Np(l) thermal-neutron fission cross section is 2500 ± 150 b [3] (1 b = 10^{-28} m^2). There are no published data on the ^{236}Np(s) fission cross section. According to systematics [4], the thermal-neutron fission cross sections of odd—odd heavy nuclei are larger, and in view of this the measurement of the ^{236}Np(s) cross section is important for the solution of many applied problems. From the scientific point of view such work would supplement the very limited information on the fissionability of odd—odd nuclei, and would help to determine the effect of spin, parity, and other characteristics of nuclear isomers on the thermal-neutron fission cross section.

Experimental Arrangement. The experiment was performed in three successive stages: the accumulation of ^{236}Np(s) in an appropriate nuclear reaction; the separation of the ^{236}Np from the irradiated sample, the removal of admixtures of heavy nuclides fissionable by thermal neutrons, and the preparation of a target; the bombardment of the target by thermal re-
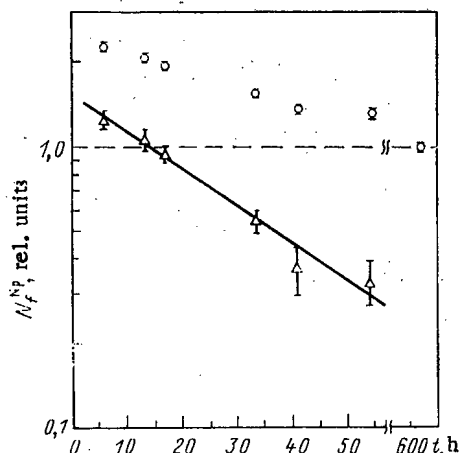
Fig. 1. Time dependence of
rate of fission of nuclei
measured from the instant of
preparation of the neptunium
target: $\bigcirc$) experimentally ob-
served fission of ^{236}Np and
impurity elements; ——) count-
ing efficiency on plateau,
taken as unity; $\triangle$) fission of
^{236}Np(s); ——) $T_1/_2$ = 22.5 h.

actor neutrons. Because of the relatively short half-life of ^{236}Np(s), all stages of the
work had to be performed quickly.

The ^{236}U(d, 2n)^{236}Np reaction was chosen for the accumulation of ^{236}Np(s) because it has
a rather large cross section at E_d = 12.6 MeV [5], and eliminates the formation of dangerous
amounts of other neptunium isotopes. A 1.3-mg/cm^2 ^{236}U target was made by the thermal de-
composition of an organometallic compound on an aluminum substrate. The ^{235}U admixture in
the uranium target was 0.05 wt. %. The target was bombarded with a 10-µA current of deuterons
for 20 h at the Leningrad University cyclotron.

The bombarded uranium was dissolved in a mixture of concentrated nitric acid and hydro-
gen peroxide. In the chemical separation process 40 ng of ^{237}Np were added to the solution
to serve as a carrier and to monitor the ^{236}Np yield. The neptunium was freed of uranium,
fission products, and the ^{236}Pu that formed in decay of ^{236}Np(s) by extraction chromatography.
Methyl trioctylammonium nitrate deposited on Teflon powder was used as an extractant [6].
The threefold chromatographic purification made it possible to obtain decontamination factors
of $\sim$10^6 and $\sim$10^4 for the removal of uranium and plutonium respectively from the neptunium.
The purified neptunium, containing isotopes with mass numbers 237 and 236, was deposited on
a platinum substrate electrolytically. The yield of neptunium in the chemical purification
was 20%.

Eleven hours elapsed between the end of the bombardment of the ^{236}U at the cyclotron
and the beginning of the measurement of the ^{236}Np(s) fission cross section at the reactor.
This time was spent in the chemical processing of the material and the transport of the tar-
get. During this time the ^{236}Np(s) decayed by 30%. The mass of ^{236}Np(s) bombarded at the
reactor was calculated from the alpha activity of the ^{236}Pu accumulated in the target after
its long cooling. At the beginning of the measurements at the reactor the mass of ^{236}Np(s)
in the target was 0.016 ng.

The ^{236}Np(s) fission cross section was measured by a relative method. A thin-walled
evacuated chamber in the form of a Duralumin tube was placed in a horizontal beam of 10^9
neutrons/cm^2·sec extracted from the reactor. A natural uranium target containing 175 ng of
^{235}U was located on the bottom of the tube. A neptunium target of the same diameter was
mounted up against the outside of the bottom of the chamber. The fission products were re-
corded by mica track detectors. The mica was placed in contact with the ^{236}Np, ensuring the
recording of 96 ± 1% [7] of the fission products. The uranium fission products were recorded
in a solid angle of 10^{-3}-10^{-2} sr, depending on the duration of the bombardment. The cadmium
ratio for ^{235}U was R = 10.0 ± 0.3 for a cadmium thickness of 2 mm; i.e. 22% of the total
neutron flux was in the energy range >0.6 eV.

231

Experimental Results. The bombardment of the ^{236}U target by deuterons led not only to the production of ^{236}Np(s), but also to the formation of the long-lived isomer ^{236}Np(l). The ratio of the numbers of ^{236}Np(s) and ^{236}Np(l) nuclei formed was 4-6 [8, 9]. In addition to the admixture of the long-lived neptunium isomer with a large fission cross section, the target may also contain fragments of such heavy nuclides as ^{235}U and ^{239}Pu which are difficult to monitor. To find the effect of the contaminants on the measurement of the number of fissions of target nuclei, we determined the time dependence of the number of fissions. Figure 1 shows that the number of fissions of target nuclei per unit time decreased and approached a constant value. It was noted earlier that ^{236}Np(s) decays partly into ^{236}Pu, which also is fissioned by thermal neutrons. Taking account of the small contribution from the fission of ^{236}Pu, the semilog graph of the time dependence of the number of fissions in the neptunium target minus the counting efficiency on the plateau has a slope corresponding to the known half-life of ^{236}Np(s), $T_{1/2} = 22.5$ h.

Since the neutron spectrum contains an epithermal component, at the start of the series of experiments and after reaching the plateau, the target was covered with cadmium and bombarded further. The ^{236}Np(s) thermal-neutron fission cross section was calculated from the formula

$$\sigma_f^{Np} = \sigma_f^U N^U \frac{FRK - F^{Cd}}{RK - 1} + \sigma_f^{Pu} W, \tag{1}$$

where

$$F = \frac{1}{N^{Np}(t)} [(N_f^{Np}/N_f^U)_t - (N_f^{Np}/N_f^U)_{pl}]. \tag{2}$$

Here σ_f^U and σ_f^{Pu} are the ^{235}U and ^{236}Pu thermal-neutron fission cross sections, taken equal to 583.5 ± 1.3 b [10] and 165 ± 20 b [3] (1 b = 10^{-28} m^2); $(N_f^{Np}/N_f^U)_t$ and $(N_f^{Np}/N_f^U)_{pl}$ are the ratios of the numbers of fissions in the neptunium and uranium targets at time t from the instant of preparation of the neptunium target, and on the plateau; N^U and $N^{Np}(t)$ are the numbers of ^{235}U and ^{236}Np(s) nuclei in the uranium and neptunium targets, F^{Cd} is a quantity referring to experiments with a cadmium cover, K is a correction for the absorption of resonance neutrons by cadmium, W is the probability of the β^- decay of ^{236}Np(s), assumed equal to 0.48 ± 0.01 [2]. The value of σ^{Np} calculated from the results of all the measurements is 2740 ± 140 b. The main contribution to the mean-square error of the cross section (5%) comes from the random component of the errors of the parameter F (4%) and the error of the number of ^{235}U nuclei in the uranium target (3%).

The experiments with a cadmium cover made it possible to estimate the epicadmium ($E_n > 0.6$ eV) resonance fission integral of ^{236}Np(s):

$$I_f^{Np} = I_f^U N^U F^{Cd} + I_f^{Pu} W, \tag{3}$$

where I_f^U and I_f^{Pu} are the resonance fission integrals of ^{235}U (275± 5 b) [3] and ^{236}Pu, respectively. It is clear from Eq. (3) that the calculated value of I_f^{Np} depends strongly on I_f^{Pu}:

$$I_f^{Np} = 200 + 0.48 I_f^{Pu} (b). \tag{4}$$

If we take the published estimated value of $I_f^{Pu} = 960$ b [11], $I_f^{Np} = 700 ± 400$ b. The error of the estimate of I_f^{Pu} is not reported in [11]. The error indicated for I_f^{Np} is mainly random, and does not include the error of I_f^{Pu}.

The values of the fission cross sections of the long-lived and short-lived isomers of ^{236}Np, having spins of 6$^-$ and 1$^-$, respectively [1], turned out to be nearly the same. This does not agree with the statement in [4] that isomers with large spin have a substantially larger fission cross section.

In conclusion, the authors thank S. M. Solov'ev and A. S. Voronin for preparing the ^{236}U targets.

LITERATURE CITED

1. M. Lindner et al., J. Inorg. Nucl. Chem., 43, 3071 (1981).
2. M. Schmorak, Nucl. Data Sheets, 36, No. 3, 367 (1982).
3. V. M. Gorbachev, Yu. S. Zamyatnin, and A. A. Lbov, Interaction of Radiation with Nuclei of Heavy Elements and Nuclear Fission [in Russian], Atomizdat, Moscow (1976).

4. H. Diamond et al., J. Inorg. Nucl. Chem., 30, 2553 (1968).
5. R. Lessler, W. Gibson, and R. Glass, Nucl. Phys., 81, 401 (1966).
6. V. K. Markov, A. N. Usolkin, and A. I. Ternovskii, Radiokhimiya, 21, 862 (1979).
7. O. V. Rumyantsev, Yu. A. Selitskii, and V. B. Funshtein, Prib. Tekh. Eksp., No. 1, 51 (1968).
8. M. Studier, J. Gindler, and C. Stevens, Phys. Rev., 97, 88 (1955).
9. J. Gindler, J. Huizenga, and D. Engelkemeir, Phys. Rev., 109, 1263 (1958).
10. H. Lemmel, in: Proc. Fourth Conf. Nucl. Cross Sections and Technology, Vol. 1, Washington (1975), p. 286.
11. B. Hinkelmann, in: Nucl. Data for Reactors, Vol. 2, Vienna (1970), p. 721.

MEASUREMENT OF BURNUP OF NUCLEAR FUEL IN A REACTOR

BY NEUTRINO EMISSION

V. A. Korovkin, S. A. Kodanev,
A. D. Yarichin, A. A. Borovoi,
V. I. Kopeikin, L. A. Mikaélyan,
and V. D. Sidorenko

UDC 539.12.08.126.5

By the mid 1970s methods of recording nuclear radiations had improved enough to permit the beginning of the development of methods for diagnosing in-pile processes from the neutrinos emitted* in the beta decay of fission fragments [1, 2]. The intensity of the $\tilde{\nu}_e$ flux, its spectral (energy) composition, and its spatial and temporal variations contain abundant information on the state and dynamics of the reactor core.

In our opinion neutrino diagnostic methods are expedient, since they do not require direct contact with the core, and are carried out remotely. In the last analysis the actual field of application and the ability to compete are determined by how well these methods and the technology are perfected. At the same time it is easy to imagine conditions under which neutrino methods offer the only way of obtaining the necessary information.

The present article describes the first step toward the practical use of neutrinos. The work was performed within the framework of a general program of applied and fundamental research [3] at the neutrino laboratory which began operating at the Roven nuclear power plant in 1982 [4].

Neutrino Diagnostics Method. The process of recording $\tilde{\nu}_e$ is based on its interaction with hydrogen

$$\tilde{\nu}_e + p \to n + e^+, \tag{1}$$

which leads to the formation of a neutron and a positron. The total cross section for this reaction ($\sim 6\cdot 10^{-43}$ cm^2/fission) is very large on the neutrino scale. The threshold of the reaction is 1.8 MeV. The neutrons formed have an energy of ~ 10 keV, so that practically all the excess of $E_{\tilde{\nu}}$ above the threshold is carried off by the positron. The cross section $\sigma_{\tilde{\nu}}$ of reaction (1) for $\tilde{\nu}_e$ of energy $E_{\tilde{\nu}}$ is determined by the same combination of weak-interaction constants as in the beta decay of the free neutron. Thus, $\sigma_{\tilde{\nu}}$ can be expressed directly in terms of the characteristics of beta decay and the kinetic energy $E_{\beta+}$ of the positron formed:

$$\sigma_{\tilde{\nu}} = \frac{2.63}{fT_{1/2}} 10^{-41} (E_{\beta+}/m_0 c^2 + 1) \, [(E_{\beta+}/m_0 c^2 + 1)^2 - 1]^{1/2}, \text{ cm}^2, \tag{2}$$

where $T_{1/2}$ is the half-life of the free neutron (630 ± 20 sec), $m_0 c^2$ is the rest energy of the positron, and $f = 1.715$.

The cross section σ_f per fission is given by the expression

$$\sigma_f = \int f(E_{\tilde{\nu}}) \sigma_{\tilde{\nu}} dE_{\tilde{\nu}}, \tag{3}$$

_____

*In VVÉR-440 reactors, for example, the power carried off by neutrinos is ~ 65 MW.

TABLE 1. Contribution of Individual Actinides to the Number of Fissions during the First and Second Runs of the VVÉR-440, and the Change in the Correction Term 1 + K

Parameter	Run		
	start	middle	end
α^5	0,861* / 0,681	0,681 / 0,587	0,526 / 0,486
α^8	0,071 / 0,073	0,074 / 0,076	0,078 / 0,078
α^9	0,068 / 0,223	0,235 / 0,30	0,355 / 0,37
α^1	0 / 0,023	0,01 / 0,037	0,041 / 0,066
$1+K$	1,015 / 0,97	0,97 / 0,95	0,94 / 0,93

*Values for the first run are in the numerator, and those for the second run are in the denominator.
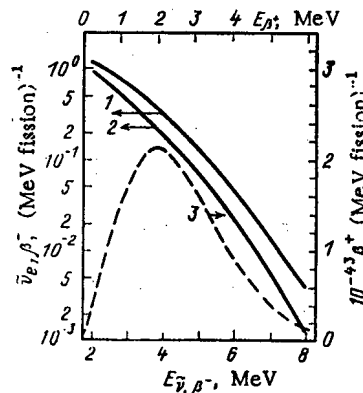
Fig. 1. Spectrum of $\tilde{\nu}_e$ generated by the reactor; 2) spectrum of β^- electrons from fission products; 3) spectrum of positrons from reaction (1).

where $f(E_\nu^-)$ (MeV·fission)$^{-1}$ is the spectral density of the $\tilde{\nu}_e$. Figure 1 shows spectra of the $\tilde{\nu}_e$ and positrons from reaction (1).

The diagnostic method being described uses the relation between the number $N_{\tilde{\nu}}$ of counts of the neutrino detector and the number N_f of fissions in the reactor:

$$N_{\tilde{\nu}} = \frac{N_f N_p}{R^2} \frac{1}{4\pi} \sigma_f \varepsilon; \quad N_f = N_{\tilde{\nu}} 4\pi R^2 \frac{1}{N_p \sigma_f \varepsilon}, \tag{4}$$

where N_p is the number of hydrogen atoms in the detector, R is the distance from the reactor to the detector in m,* and ε is the efficiency, i.e., the ratio of the number of recorded events to the total number occurring in the detector. For definiteness we note that in a detector containing 1 m³ of organic scintillation material, the neutrino effect for the VVÉR-440 is $N_{\tilde{\nu}} \approx 10^6 \varepsilon/R^2$ events per day. The main problem is the determination of the number N_f of fissions from the "responses" $N_{\tilde{\nu}}$ of the neutrino instrument. After determining N_f, the burnup M and the energy production W can be determined sufficiently accurately.

*We assume a point source and a point detector.
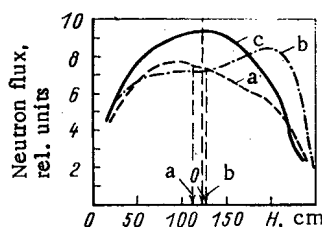
Fig. 2. Energy density distribution along height of core: a, b) middle and end of first run; c) start of second run; 0, geometric center of core; arrows a and b indicate "centers of gravity."

The neutrino detector can be used to make absolute measurements of N_f, M, and W (in this case it is necessary to know σ_f, ε, and N_p which enter Eq. (4)), and as a device whose scale must be calibrated beforehand. In this case measurements of $N_{\tilde{\nu}}$ must be made in the flux of a reactor with known characteristics to determine the constant $1/N_p\sigma_f\varepsilon$. We note that at the present time the error of the absolute measurements is larger, mainly because of the uncertainty in the value of σ_f. We used both methods.

Let us discuss the error in σ_f and the reasons for the failure of a linear relation between N_f and $N_{\tilde{\nu}}$ in Eq. (4). In experiments performed at the I. V. Kurchatov Institute of Atomic Energy it was noticed for the first time that the spectrum $f(E_{\tilde{\nu}})$, and therefore also the cross section σ_f, depends on which actinide is fissioned [1-3, 5, 6]. In reactors with fuel highly enriched in ^{235}U this is unimportant. In reactors of the VVÉR type, and in a number of others, several actinides (^{235}U, ^{238}U, ^{239}Pu, and ^{241}Pu) are burned up simultaneously. Introducing their fractions α^i of the number of fissions, we can write

$$\sigma_f = \Sigma\alpha^i\sigma_f^i; \quad \sigma_f^i = \int f_i\sigma_{\tilde{\nu}}dE_{\tilde{\nu}}; \quad \Sigma a^i = 1, \tag{5}$$

where f_i is the $\tilde{\nu}_e$ spectrum of the given isotope. Separating out the ^{235}U contribution, we obtain

$$\sigma_f = \sigma_f^5(1+K); \quad 1+K = 1 + \Sigma\alpha^i(\sigma_f^i/\sigma_f^5 - 1). \tag{5a}$$

In order to find σ_f^5 and the ratios of the cross sections appearing in Eq. (5a), it is necessary to know the spectra f_i.

The spectrum f_i of a given actinide can be found by summing the individual spectra of the fission products, taking account of their yields. Research in this direction is being developed intensively. However, because of a lack of part of the input data, different results are obtained by different authors. In the last three years five values have been obtained for σ_f^5 ([7] and references cited in it).

Henceforth, we assume

$$\sigma_f^5 = (6.60 \pm 0.7)\cdot 10^{-43}\,cm^2/fission. \tag{6}$$

All the values of σ_f^5 cited lie within the limits given in Eq. (6).

The error of the value of σ_f^5 can be decreased by using measurements of the beta spectra of the mixture of fission products of this isotope. This idea, which arose long ago [1, 8], was developed further in [9-11]. In those papers a rule was found for determining the $\tilde{\nu}_e$ spectrum directly from the integrated beta electron spectrum of the fission products. Recent measurements of the beta spectra of ^{235}U and ^{239}Pu performed at the I. V. Kurchatov Institute of Atomic Energy [11] and measurements reported in [12] so far have not enabled us to decrease the error under consideration; new measurements are needed. The correction term $1 + K$ in Eq. (5a) is much more accurately known than σ_f^5, since the ratios of the cross sections appearing in it are relatively insensitive to the details of the calculation of neutrino spectra. According to [10, 13], $\sigma_f^9/\sigma_f^5 = 0.69 \pm 0.03$, $\sigma_f^8/\sigma_f^5 = 1.55 \pm 0.15$, and $\sigma_f^1/\sigma_f^5 = 1.0 \pm 0.1$.

235
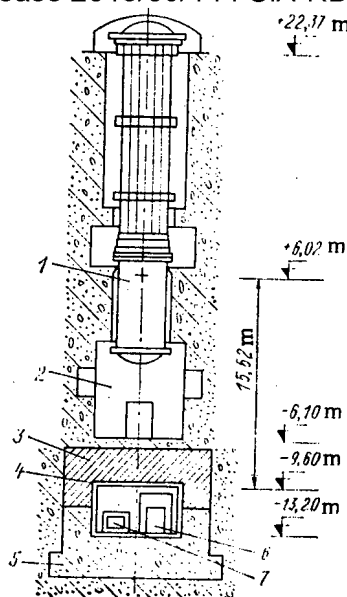
Fig. 3. Schematic diagram of arrangement of equipment and measuring instruments: 1) center of core; 2) technological room; 3) heavy-concrete shield; 4) steel lining of room; 5) concrete slab; 6) neutrino spectrometer; 7) antineutrino flux integrator.

Let us consider now the change of contributions of individual actinides, and the correction term 1 + K during the first two runs of the VVÉR-440 (Table 1). The data on α_i are from [14, 15]. Table 1 shows that the nonlinearity determined by the change in the core composition is not large. This correction can be introduced if the core composition is very inaccurately known. If we leave out the first months after the first startup of the reactor, all the changes in 1 + K amount to 0.96 ± 0.03. In the preliminary stage of the work we neglect these changes and take 1 + K = 0.96.

We now consider briefly the expression relating the fuel burnup M* and the energy production W to the number N_f of fissions.

Clearly,

$$M = N_f \overline{m}_a = N_f \frac{\overline{A}}{N_A}; \quad W = N_f \overline{E}_f, \tag{7}$$

where $\overline{m}_a$ and $\overline{A}$ are the average mass and atomic weight of the fissionable actinide, $\overline{E}_f$ is the average energy released in the reactor per fission, and N_A is Avogadro's number. It is easy to confirm that in the VVÉR-440 $\overline{A}$ and $\overline{E}_f$ do not vary more than ±1% during a run. It was assumed that $\overline{A} = 237 ± 1.5$ and $\overline{E}_f = 202 ± 2$ MeV. Using these values, we obtain $N_f = 2.55 \cdot 10^{24} \cdot$ M (kg);

$$N_f = 2.67 \cdot 10^{21} W \quad \text{MW days.} \tag{7a}$$

Finally let us consider the effect of the finite core size on the error of the method. If the distance R in Eq. (4) is at least five times as large as the core dimensions, it is sufficient to restrict ourselves to the dipole approximation. Then it is easy to show that the neutrino source can be considered a point, but R must be understood as the distance to the "center of gravity" of the energy during a run. In the measurements of the energy density distribution by the activation method (Fig. 2), it was established that the displacement actually was approximately 10 cm from the geometric center of the core, which for the actual

---

*Burnup is the total mass of actinides undergoing fission.

236
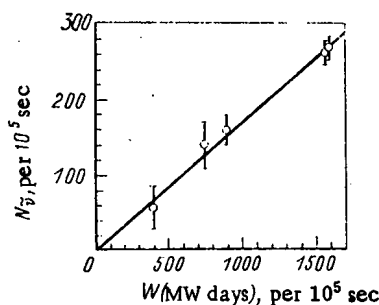
Fig. 4. Calibration of
instrument scale.
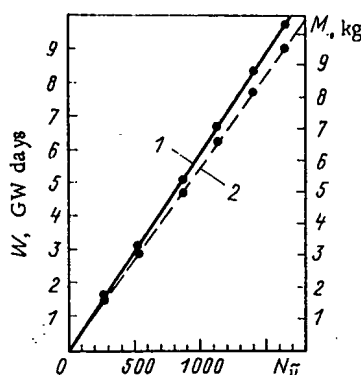
Fig. 5. Measurement of
energy production W and
burnup M: 1) calibra-
tion of scale (cf. Fig.
4); 2) absolute scale
of instrument; •, mea-
sured values of $N_{\tilde{\nu}}$.

distance R = 18.4 m (cf. later) leads to a correction of ∿1.2%. At the present stage of the
work we neglect this effect. In order that this effect not exceed 1%, the distance from the
detector to the center of the VVÉR-440 core should be at least 25 m for the detector located
close to the reactor axis, and ∿15 m in the transverse direction.

Measurements and Results. The measurements of $\tilde{\nu}_e$ were performed with a scintillation
spectrometer. The general arrangement is shown in Fig. 3. The target for the $\tilde{\nu}_e$ and the
moderator of the neutrons formed was a liquid organic scintillator based on decalin ($C_{10}H_{18}$)
with the addition of ∿0.5 g/liter of gadolinium. The scintillator (235.5 liters) was con-
tained in a 0.5 × 0.7 × 0.7 m tank, and was scanned by 24 FÉU-49 photomultipliers. The life-
time of thermal neutrons in the scintillator was ∿54 µsec (195 µsec without gadolinium).

The criteria for selecting events from reaction (1) are the following: starting pulse
in the energy range 1.0-9.5 MeV (positron); second pulse in the time interval up to 200 µsec
after the first in the energy release range 3-10 MeV (neutron). The background of random
coincidences was measured continuously by the method of delayed coincidences, and was sub-
tracted.

The efficiency of counting neutrino events was calculated by the Monte Carlo method.
The main units of the program were tested by comparing the calculations with the results of
check experiments with various gamma and neutron sources. The value of the efficiency ob-
tained in this way was ε = 0.285 ± 6%. A decrease of the error in ε to 1-1.5% is projected.
The procedure is described in more detail in [16].

With the chosen selection criteria the detector records a certain number of events (back-
ground) even in the absence of a neutrino flux. This determines the position of the "zero"
of the instrument. In most cases these events are initiated by fast neutrons accompanying
cosmic muons. The zero of the instrument is determined by measurements during the time the
reactor is shut down for routine maintenance. The measurements required 24.2 days. It was
found that the zero of the instrument corresponded to 94.2 ± 3.5 counts/day. During almost

237

two months no drift of the zero was observed within the limits of error. It is assumed that in the future the zero level of the instrument can be substantially reduced by more stringent selection criteria.

The instrument scale was calibrated at various values of the average thermal power of the reactor. We list below values of the energy production in 10^5 sec, determined by a thermal method, and the instrument reading during that same time (Fig. 4):

W, MW days	1590	1567	900	747	397
$N_{\tilde{\nu}}$	267 ± 16	261 ± 18	160 ± 20	141 ± 35	58 ± 32

The relatively large error at low power is a result of the short operating time of the reactor under these conditions. The results obtained for calibrating the scale are well described by the linear relations W^{cal} (MW days) $= 5.92 \pm 0.26)N_{\tilde{\nu}}$ and M^{cal} (kg) $= (6.21 \pm 0.28)10^{-3} N_{\tilde{\nu}}$.

The absolute scale of the instrument was found from relations (4), (5a) and (7a): M^{abs} (kg) $= 5.74 \cdot 10^{-3} N_{\tilde{\nu}}$, W^{abs} (MW days) $= 5.47 N_{\tilde{\nu}}$; the error of the proportionality factor is 12%. In calculating the absolute scale the following values were used: $N_p = (1.59 \cdot 10^{28}) \pm 2\%$, $R = (1.84 \cdot 10^3$ cm$) \pm 0.5\%$, $\varepsilon = (0.285) \pm 6\%$, $\sigma_f^5 = (6.6 \cdot 10^{-43}$ cm^2/fission$) \pm 10\%$, and $1 + K = (0.96) \pm 2\%$. Within the limits of error good agreement was found between the absolute and relative scales. Figure 5 shows M and W as functions of $N_{\tilde{\nu}}$.

In the last stage the burnup and energy production were measured during $6 \cdot 10^5$ sec (6.94 days) of reactor operation. During this time the thermal measurements were performed with particular care. The accumulation of $N_{\tilde{\nu}}$ was measured over a sequence of 10^5-sec intervals: $N_{\tilde{\nu}} = 266$, 532, 860, 1127, 1399, and 1653. These values were plotted on the straight calibration lines for W^{abs} and W^{cal} (Fig. 5). As a result the following values were obtained at this stage of the work: $W^{cal} = 9.79$, $W^{abs} = 9.04$, $W^T = 9.64$, $M^{cal} = 10.3$ kg, $M^{abs} = 9.5$ kg (energy production per thousand MW days).

Let us discuss briefly the prospects for improved accuracy of the method. In the not very distant future the error of the absolute method may be reduced to 3–4%. To do this it is necessary to obtain a more accurate spectrum of the ν_e arising in the fission of ^{235}U. A further decrease in the errors requires more accurate values of the weak-interaction constants. This information can be obtained from experiments on the decay of the free neutron. The errors in calibrating the scale are determined mainly by the limiting accuracy which can be achieved in determining the thermal power of the reactor during the calibration period. This limit will probably be $\pm 1.5\%$ in the forseeable future.

We were not concerned earlier with the statistical errors related to fluctuations of the number of counts $N_{\tilde{\nu}}$. The model used in the present work ensures a statistical error of 1% only during 2–3 months of measurements. In determining the energy production for one week, for example, the error is three to five times as large. The fast response of the detector can be increased by a factor of ten, for example, by a corresponding increase in its dimensions, and thus also in the counting rate. Scintillation devices used in other fields of neutron physics and in astrophysics have an effective target mass 10^3–10^4 times as large as that in our experiments. Therefore, after such an increase the detector would still be small on the neutrino scale.

The authors thank M. A. Markov for showing great interest in the work and stimulating it at all stages; V. A. Legasov for giving substantial help in establishing the general course of the research; A. G. Zelenkov for interesting discussions; colleagues of the physical and thermophysical laboratories for discussions and for assisting with the measurements.

LITERATURE CITED

1. A. A. Borovoi and L. A. Mikaélyan, Preprint IAÉ-2546, Moscow (1975).
2. A. A. Borovoi and L. A. Mikaélyan, At. Energ., 44, 508 (1978).
3. L. Mikaélyan, in: Proc. Int. Conf. "Neutrino 77," Vol. 2, Nauka, Moscow (1978), p. 383.
4. A. A. Borovoi and L. A. Mikaélyan, At. Energ., 54, 143 (1983).
5. A. A. Borovoi, Yu. L. Dobrynin, and V. I. Kopeikin, Yad. Fiz., 25, 264 (1977).
6. S. Fayans, L. Mikaélyan, and Yu. Dobrynin, [3], p. 391.
7. A. I. Afonin et al., Pis'ma Zh. Eksp. Teor. Fiz., 38, 361 (1983).
8. R. Carter et al., Phys. Rev., 113, 280 (1959).
9. A. A. Borovoi et al., Yad. Fiz., 36, 400 (1982).

10. P. Vogel et al., Phys. Rev., C24, 1543 (1981).
11. A. A. Borovoi, Yu. V. Klimov, and V. I. Kopeikin, Yad. Fiz., 37, 1345 (1983).
12. K. Schreckenbach et al., Phys. Lett., B99, 251 (1981).
13. V. I. Kopeikin, Yad. Fiz., 32, 1507 (1980).
14. F. Ya. Ovchinnikov et al., Operating Conditions of Water-Cooled-Water-Moderated Power Reactors [in Russian], Atomizdat, Moscow (1979).
15. A. K. Kruglov and A. P. Rudik, Artificial Isotopes and Methods for Calculating Their Formation in Nuclear Reactors [in Russian], Atomizdat, Moscow (1977).
16. L. I. Afonin et al., Preprint IAÉ-3676/2, Moscow (1982).

IRRADIATION OF THE USSR POPULATION IN MEDICAL DIAGNOSTIC PROCEDURES

E. I. Vorob'ev, R. V. Stavitskii,   UDC 616.07.75
V. A. Knizhnikov, R. M. Barkhudarov, V. N. Korsunskii,
V. I. Popov, Yu. I. Tarasenko, V. A. Postnikov,
N. V. Frolov, and V. P. Sidorin

Medical radiology and radionuclide studies represent leading diagnosis methods. Their high performance has meant that they have become widely used, which has involved improvements in apparatus and researches designed to provide new methods to increase the informativeness. On the other hand, medical diagnosis is one of the principal man-made radiation factors for the population, and therefore patient exposure levels have latterly attracted considerable attention from the viewpoint of radiation safety. This is due on the one hand to the assumption that there is no threshold in the effects of ionizing radiation, according to which any dose is not a matter of indifference to the body, and on the other the substantial scope for reducing population doses, which to a substantial extent can compensate for the effects from other sources such as nuclear-power installations. In particular, the average population dose is reduced by reducing the number of fluoroscopic examinations and increasing the numbers of radiographic and fluorographic ones. For this reason, there have recently been substantial changes in the structure of x-ray examinations, although the total number has increased (Table 1). Age features have been taken into account, and the number of young persons undergoing radiology has been reduced, which also reduces the possible remote effects (especially genetic ones).

Radioisotope diagnosis is used in this country in 320 laboratories in the Ministry of Health of the USSR system. In 1981, about one million people were examined in this way. It is planned to make more controlled use of radiopharmaceuticals (RP) and to increase the use of short-lived nuclides. This reflects the tendency to reduce the patient irradiation level, which is envisaged in current rules for patient irradiation in diagnostic procedures [1], which represent the first such rules in world practice. It was planned for 1982 that the total number of persons examined should increase by 25% by comparison with the previous year, while at the same time it was proposed to reduce the consumption of RP such as ^{131}I-sodium iodide by 16%, ^{51}Cr-sodium chromate by 20%, ^{169}Yb-DTPA by 31%, and to increase the use of other preparations such as ^{99m}Tc generators by more than a factor two and of ^{133}Xe by 11%. The most widely used radiopharmaceuticals in the USSR are ^{131}I-hippuran (293 laboratories), ^{131}I-sodium iodide (280 laboratories), ^{131}I-Bengal red (250 laboratories), ^{131}I-albumen (155 laboratories), ^{131}I-MAA (130 laboratories), ^{198}Au colloid (265 laboratories), ^{197}Hg-promeran (226 laboratories), ^{32}P-sodium salt (134 laboratories), and ^{99m}Tc generators (110 laboratories).

This paper gives estimates of the mean irradiation levels for the USSR population in 1981 due to radiological and radionuclide examinations. A difference from [2] is that the estimates are based on a fuller analysis of the types of procedure and forms of radiopharmaceutical, and also they are represented in units of effective equivalent dose (EED), in accordance with the ICRP recommendations [3]. Note that we have not considered repeated procedures performed in accordance with indications or in order to refine the diagnosis.

TABLE 1. Dynamics of Radiological Exam-
ination Structure in the USSR

Examination	Number of examinations per 1000 people		Percent change
	1964	1981	
Fluoroscopy	439	220	—50%
Radiography	171	235	+37%
Fluorography	183	503	+175%
Total	793	958	+21%

TABLE 2. Mean Individual Radiation Dose to the USSR Population Due to X-Ray Diagnosis, mSv/yr

Organ	Equivalent dose due to				Effective equivalent dose due to			
	radiography	fluoroscopy	fluorography	all forms	radiography	fluoroscopy	fluorography	all forms
Active bone marrow	0,39	1,42	0,37	2,18	0,047	0,17	0,04	0,26
Lungs	0,33	1,40	0,63	2,36	0,04	0,17	0,08	0,29
Mammary glands	0,17	0,36	0,11	0,64	0,026	0,054	0,017	0,097
Thyroid	0,52	0,33	0,09	0,94	0,016	0,01	0,003	0,029
Gonads	0,35	0,36	0,004	0,71	0,087	0,091	0,001	0,179
Others	0,54	0,95	0,36	1,85	0,162	0,285	0,108	0,555
Total					0,378	0,778	0,249	1,41

We used the data on the structures and frequencies of procedures in 1981–1982 provided by official statistics and questionnaire results obtained in five regions of the country in order to estimate the radiation doses arising from radiological examinations. This enabled us to estimate the frequencies of the 12 major dose-forming types of examination. The average number of examinations is 958 a year per 1000 population, with fluctuations between republics from 464 to 1350. Here 24.5% are accounted for by radiography, 23% by fluoroscopy, and 52.5% by fluorography. The absorbed doses in various organs have been measured on a tissue-equivalent bone-wax phantom by means of thermoluminescent LiF dosemeters (made by Victoreen, USA), which were placed in the organs in numbers of 5–150 in accordance with the volume. We simulated the usual radiological examination conditions: voltage, field size, and focus-detector distance. The voltages were 60–120 kV. The mean equivalent dose to active bone marrow was calculated as the weighted mean by mass over the four sections: head 0.13 M, neck 0.04 M, thorax 0.33 M, and pelvis 0.49 M, where M is the total mass of bone marrow [4]. In other cases, the mean doses were determined as the arithmetic-mean values of the readings of dosemeters in the organ. The error in determining the average tissue doses was not more than 20%.

Table 2 shows that the main doses are to the lungs (2.36 mSv/yr) and the active bone marrow (2.18 mSv/yr). The main contributions to the EED come from the stomach, liver, spleen, kidneys, and pancreas. The average individual EED to the population due to x-ray diagnosis is 1.4 mSv/yr (140 mber/yr), with fluoroscopy accounting for 55.4% (0.78 mSv/yr), radiography for 26.9% (0.38 mSv/yr), and fluorography 17.7% (0.25 mSv/yr).

We calculated the radiation dose to the population from diagnostic radioisotope examinations on the basis of the total activity for each particular nuclide and compound together with the data of [5, 6], whose results are derived from a unified scheme [7] based on a heterogeneous model for a standard man [8] and clinical data on RP biokinetics. This approach to estimating doses from diagnostic RP was developed by the MIRD committee in the USA, and it has some substantial advantages over traditional methods used up to the 1970s and provides more correct estimation of the radiation burden.

The total activity of radionuclides administered to patients in 1981 was 1050730 GBq (28.4 kCi), with ^{131}I-hippuran accounting for 46%, ^{131}I-sodium iodide 28%, and [198]Au colloid about 10%. Table 3 gives the average doses to the USSR population from RP, which shows that

240

TABLE 3. Mean Individual Doses to the USSR Population Due to Radiopharmaceutical Procedures, mSv/yr

Organ	Equiv. dose	Effective equivalent dose
Active bone marrow	$4,9 \cdot 10^{-3}$	$0,59 \cdot 10^{-3}$
Lungs	$0,98 \cdot 10^{-3}$	$0,12 \cdot 10^{-3}$
Thyroid	$507,0 \cdot 10^{-3}$	$15,2 \cdot 10^{-3}$
Gonads	$1,1 \cdot 10^{-3}$	$0,28 \cdot 10^{-3}$
Whole body	$3,5 \cdot 10^{-3}$	$3,51 \cdot 10^{-3}$
Other organs	$20,5 \cdot 10^{-3}$	$12,3 \cdot 10^{-3}$
Total		$32,0 \cdot 10^{-3}$

TABLE 4. Mean Individual Radiation Doses to the Populations of Certain Countries due to Medical Diagnostic Procedures, mSv/yr

Country	X-ray diagnosis	Radioisotope diagnosis
USSR	1,41	0,032 (our results)
Poland	0,6 [9]	—
Japan	1,8 [9]	0,02 [9]
Australia	0,4 [10]	0,02 [9]
Sweden	0,45 [10]	0,08 [9]
Denmark	—	0,06 [9]
Britain	0,29 [10]	—
USA	—	0,15 [9]
Finland	1,16 [10]	—

TABLE 5. Irradiation of the USSR Population in Medical Diagnostic Procedures

Examination	Effective equiv. dose	
	individual, mSv/yr	collective, man-Sv/yr
Radiography	0,38	$1,03 \cdot 10^5$
Fluoroscopy	0,78	$2,12 \cdot 10^5$
Fluorography	0,25	$0,68 \cdot 10^5$
Radionuclide	0,03	$0,09 \cdot 10^5$
Total	1,44	$3,92 \cdot 10^5$

the largest contribution to the EED comes from irradiation of the thyroid (about 50%), with the other organs and the whole body accounting for the rest.

The doses to the USSR population are characteristic of those for industrially developed countries (Table 4), in which diagnostic x rays on average account for 1 mSv/yr with procedure frequencies from 300 to 900 a year per thousand people [9]. The frequency of radiological examinations in the USSR is 958 per year per thousand people, and the 40% excess over the average for developed countries in the EED is due to differences in procedure frequency. The irradiation of the USSR population from radioisotope diagnosis is less than the mean. The frequencies of radionuclide procedures vary from 4 to 400 a year per thousand people in developed countries [10]. In the USSR, the frequency is about 4 a year per thousand people, i.e., is minimal for such countries.

Table 5 gives data on the USSR population irradiation from medical diagnosis, which shows that the exposure is approximately equal to the average radiation background, which is 1.1-2.0 mSv/yr in normal regions [9, 11]. The current level of development in world nuclear engineering is responsible for a mean annual dose of about 0.1 μSv [9], i.e., only about 0.007% of the medical dose. The developments envisaged in nuclear power up to the year 2000 lead one to expect an increase in this proportion to 0.07%, and to 1.4% by the year 2100, on the assumption that medical irradiation remains unchanged. This makes it clear how important it

is to reduce irradiation for medical purposes even by a fraction of a percent. Of the other man-made sources, only irradiation in buildings due to natural radionuclides in the materials makes a contribution approximately equal to that from medical diagnosis [11], the contributions from other sources being less by factors of 10–100.

The data show that it is necessary and possible to improve diagnosis in order to reduce radiation burdens. The doses can be reduced by introducing new apparatus and methods together with individual protection facilities, and also by controlling the numbers and forms of the examinations. A study should be made of the actual diagnostic value of the various methods, which should be evaluated on the basis of a utility-damage criterion, i.e., by comparing the advantage in socially significant health parameters resulting from the diagnostic information with the possible unfavorable consequences in order to refine the indications for various procedures.

LITERATURE CITED

1. V. Z. Agranat, V. A. Knizhnikov, and F. M. Lyass, Med. Radiologiya, No. 6, 3 (1971).
2. V. A. Knizhnikov et al., Collective Doses to the USSR Population as a Result of the Use of Ionizing-Radiation Sources for Medical Purposes [in Russian], GKIAÉ, ICRP (1978).
3. Radiological Protection: ICRP Recommendations, Publication 26 [in Russian], Atomizdat, Moscow (1978).
4. R. Ellis, in: Department of Health, Education and Welfare, Public Health Service, Food and Drug Administration, USA (1980), p. 23.
5. "MIRDO Dose Estimate Report," J. Nucl. Medicine, 14, 4950, 755 (1973); 16, 1084, 173, 857, 1095, and 1277 (1975); 17, 74 (1976).
6. H. Roedler, A. Kaul, and G. Hine, Internal Radiation Dose in Diagnostic Nuclear Medicine, Verlag H. Hoffman, Berlin (1978).
7. R. Loevinger and M. Berman, J. Nucl. Medicine, Suppl. No. 1, 7 (1968).
8. W. Snyder, J. Nucl. Medicine, Suppl. No. 3, 5 (1969).
9. Ionizing Radiation: Sources and Biological Effects, UN SCEAR, N.Y. (1982).
10. "Medical irradiation": Paper SCEAR UN A/AS, 82/R, 401 (1981).
11. E. I. Vorob'ev et al., At. Energ., 43, No. 5, 374 (1977).

BEHAVIOR OF THORIUM IN THE LATERITE PROCESS

V. A. Kopeikin   UDC 550.43:550.424:550.551.3

It follows from the data of [1–7] that thorium is an abundant element in bauxites and, according to [8], its concentration coefficient in them is equal to 4.2, but according to [6] it is 3.4. Laterite bauxites differ from sedimentary and sedimentary-alluvial bauxites in the higher thorium content (46, 29, and 41 g/ton, respectively; the mean weighted content is 44 g/ton [6]). Data about the content of thorium are used for the diagnostics of feed rocks for bauxites.

The behavior of thorium in aqueous solutions at a temperature of 25°C and a pressure of 101.325 kPa was considered in [6]. It was shown in [9] that the possibility of formation of bauxite deposits depends directly on the climate and, at a temperature below 10–15°C, the formation of bauxites is restricted sharply. The effect of the temperature factor on the behavior of thorium in the laterite process has not been considered up to now, although the diurnal temperature at the surface of bauxite deposits can reach 80°C [10]. In the present paper, an analysis is conducted of the behavior of thorium in aqueous solutions at elevated temperature.

In the laterite weathering profile, the solutions are very dilute (ion strength, according to modeling data of the bauxite formation process on a computer [9], is less than 10^{-4}), and therefore the activity coefficients of all components are almost equal to unity. Taking this into account, the molarity of the components is equal to their activity.

TABLE 1. Value of the Equilibtium Constants of Reactions (1)-(6) at a Different Temperature

t, °C	$-\log K$					
	K_1	K_2	K_3	K_4	K_5	K_6
25	10,12	19,88	27,65	33,99	37,34	37,34
50	9,73	19,21	27,37	33,75	36,97	37,12
75	9,56	18,73	27,34	33,81	36,94	37,24
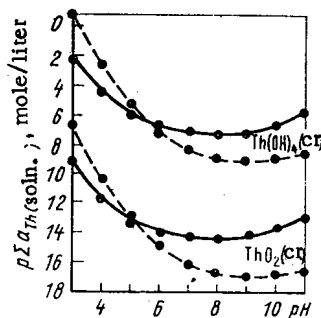
Fig. 1. Solubility of ThO$_2$(cr) and Th(OH)$_4$ at 25 (-- --) and 75°C (——).

Laterite weathering process takes place due to the action of rain water on rocks and therefore we shall assume that in aqueous solutions of the laterite weathering profile, there exist in fact only hydroxy complexes of thorium.

The probable reactions between thorium ions in aqueous solution can be represented in the form of the following equations:

$$Th^{4+} + OH^- = Th(OH)^{3+}; \tag{1}$$

$$Th^{4+} + 2OH^- = Th(OH)_2^{2+}; \tag{2}$$

$$Th^{4+} + 3OH^- = Th(OH)_3^+; \tag{3}$$

$$Th^{4+} + 4OH^- = Th(OH)_4^0; \tag{4}$$

$$Th^{4+} + 5OH^- = Th(OH)_5^-; \tag{5}$$

$$Th^{4+} + 6OH^- = Th(OH)_6^{2-}. \tag{6}$$
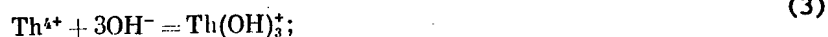
The equilibrium constants of these reactions have been calculated from [6, 11] and are given in Table 1. The equilibrium constants of reactions (3)-(6) at 50 and 75°C are calculated by the equation proposed in [12, 13] for estimating the instability constant of the complexes at elevated temperature. When calculating the constants by this equation, we shall assume that $r_{Th^{4+}}$ = 1.10 Å (1 Å = 10^{-10} m); r_{OH^-} = 1.40 Å; α_{OH^-} = 2.04·10^{-24} cm^3 [14]; ε_{323K} = 69.78 and ε_{348K} = 62.13 [5].

The total content of thorium in aqueous solution can be expressed as the sum of the molarity of all its ions:

$$\Sigma m_{Th(soln.)} = m_{Th^{4+}} + m_{Th(OH)^{3+}} + m_{Th(OH)_2^{2+}} + m_{Th(OH)_3^+} + m_{Th(OH)_4^0} + m_{Th(OH)_5^-} + m_{Th(OH)_6^{2-}}. \tag{7}$$

Assuming the total thorium content to be unity, and expressing the molarity of all thorium ions in terms of the molarity of every single ion, for example by $m_{Th^{4+}}$, m_{OH^-} by K_w/m_{H^+} (where K_w is the ionic product of water), and equating $m_{Th(soln)}$ to unity, we obtain

$$\Sigma m_{Th(soln.)} = 1 = m_{Th^{4+}} \left(1 + \sum_{i=1}^{6} \frac{K_i K_w^i}{m_{H^+}^i} \right). \tag{8}$$

243

TABLE 2. Ratios of the Th Ion Concentrations, Their Percentage Content and the Solubility of Th(OH)$_4$ and ThO$_2$ in Aqueous Solution at 75°C

Compound	pH								
	3	4	5	6	7	8	9	10	11
Th^{4+}	$\frac{0,3038}{49,7}$	$\frac{1,7169}{1,9}$	$\frac{4,373}{0}$	$\frac{7,5118}{0}$	$\frac{11,1564}{0}$	$\frac{15,1089}{0}$	$\frac{19,1984}{0}$	$\frac{23,6732}{0}$	$\frac{28,5723}{0}$
Th(OH)$^{3+}$	$\frac{0,4238}{37,7}$	$\frac{0,8369}{14,6}$	$\frac{2,493}{0,3}$	$\frac{4,6318}{0}$	$\frac{7,2764}{0}$	$\frac{10,2289}{0}$	$\frac{13,3184}{0}$	$\frac{16,7932}{0}$	$\frac{20,6923}{0}$
Th(OH)$_2^{2+}$	$\frac{0,9338}{11,6}$	$\frac{0,3469}{45,0}$	$\frac{1,003}{9,9}$	$\frac{2,1418}{0.7}$	$\frac{3,7864}{0}$	$\frac{5,7389}{0}$	$\frac{7,8284}{0}$	$\frac{10,3032}{0}$	$\frac{13,2023}{0}$
Th(OH)$_3^{+}$	$\frac{2,0038}{1,0}$	$\frac{0,4169}{38,3}$	$\frac{0,073}{84,5}$	$\frac{0,2118}{61,4}$	$\frac{0,8564}{13,9}$	$\frac{1,8089}{1,6}$	$\frac{2,8984}{0,1}$	$\frac{4,3732}{0}$	$\frac{6,2723}{0}$
Th(OH)$_4^{0}$	$\frac{5,2138}{0}$	$\frac{2,6269}{0,2}$	$\frac{1,283}{5,2}$	$\frac{0,4218}{37,9}$	$\frac{0,0664}{85,8}$	$\frac{0,0189}{95,7}$	$\frac{0,1084}{77,9}$	$\frac{0,5832}{26,1}$	$\frac{1,4823}{3,3}$
Th(OH)$_5^{-}$	$\frac{11,7638}{0}$	$\frac{8,1769}{0}$	$\frac{5,833}{0}$	$\frac{3,9718}{0}$	$\frac{2,6164}{0,3}$	$\frac{1,5689}{2,7}$	$\frac{0,6584}{22,0}$	$\frac{0,1332}{73,6}$	$\frac{0,0323}{92,8}$
Th(OH)$_6^{2-}$	$\frac{21,1438}{0}$	$\frac{16,5569}{0}$	$\frac{13,213}{0}$	$\frac{10,3518}{0}$	$\frac{7,9964}{0}$	$\frac{5,9489}{0}$	$\frac{4,0384}{0}$	$\frac{2,5132}{0,3}$	$\frac{1,4123}{3,9}$
$-\log C_{Th(soln.)}$, mole/liter:									
Th(OH)$_4$(cr)	2,07	4,65	6,00	6,86	7,21	7,26	7,17	6,7	5,8
ThO$_2$ (thorianite)	9,24	11,82	13,17	14,03	14,38	14,43	14,34	13,87	12,97

TABLE 3. Free Energy of Compounds $-\Delta G_{fT}^{o}$, kJ/mole

Compound	25°C	50°C	75°C
Th^{4+}	723,87	720,78	717,58
Th(OH)$^{3+}$	938,79	932,12	925,97
Th(OH)$_2^{2+}$	1152,06	1141,87	1131,70
Th(OH)$_3^{+}$	1353,52	1343,48	1333,71
Th(OH)$_4^{0}$	1546,99	1534,10	1521,54
Th(OH)$_5^{-}$	1723,39	1705,16	1687,01
Th(OH)$_6^{2-}$	1880,71	1857,22	1833,63
OH$^-$	157,28	151,13	144,64
H$_2$O (liq.)	237,19	233,13	229,16
Th(OH)$_4$ (cr)	1599,09	1584,56	1570,04
ThO$_2$ (cr)	1169,15	1164,32	1159,51

The solution of Eq. (8) for 25°C is given in [6]. Here, we shall carry out the calculation of the behavior of thorium in aqueous solution according to the data of Table 1:

for 50°C

$$\Sigma m_{Th(soln.)} - 1 = m_{Th^{4+}}(1 + 10^{-3,53}/m_{H^+} + 10^{-7.3}/m_{H^+}^2 + 10^{-12,4}/m_{H^+}^3 + 10^{-19,28}/m_{H^+}^4 + 10^{-29,31}/m_{H^+}^5 + 10^{-42,42}/m_{H^+}^6);$$

(9)

for 75°C

$$\Sigma m_{Th(soln.)} - 1 = m_{Th^{4+}}(1 + 10^{-3,12}/m_{H^+} + 10^{-6,63}/m_{H^+}^2 + 10^{-10.7}/m_{H^+}^3 + 10^{-16,91}/m_{H^+}^4 + 10^{-26,46}/m_{H^+}^5 + 10^{-38,84}/m_{H^+}^6).$$

(10)

The solution of Eq. (10) for different pH values is given in Table 2, where the negative common logarithm of the ion content in the solution is given in the numerator, and the percentage amount of this ion (with an error of up to 0.1%) in the denominator. The value of the electroneutrality point is equal to 9.16 at 25°C [6], 8.45 at 50°C and 7.88 at 75°C.

The free energy of Th^{4+}, Th(OH)$^{3+}$, Th(OH)$_2^{2+}$, OH$^-$, H$_2$O (liq.), ThO$_2$(cr), and Th(OH)$_4$(cr) at elevated temperature is calculated from the data of [11]; the values of ΔG_{tT} of the other hydroxy components of thorium are obtained by means of the equilibrium constants of reactions (3)-(6), calculated according to [12, 13], and are given in Table 3.

According to the data of [6], ThO$_2$ (cr) is more stable than Th(OH)$_4$(cr). The solubility of thorianite was calculated by the equation

$$ThO_2 + 4H^+ = Th^{4+} + 2H_2O. \tag{11}$$

The equilibrium constant of this reaction will be equal to

$$K_{(11)} = a_{Th^{4+}}/a_{H^+}^4;$$
$$lg\, a_{Th^{4+}} = lg\, K_{(11)} - 4\,pH. \tag{12}$$

At 75°C, the equation for calculation of the solubility of ThO_2 has the form

$$lg\, a_{Th^{4+}} = 2.46 - 4\,pH. \tag{13}$$

We calculate the solubility of $Th(OH)_4(cr)$ by the equation

$$Th(OH)_4 + 4H^+ = Th^{4+} + 4H_2O. \tag{14}$$

The equilibrium constant of reaction (14) will be similar to $K_{(11)}$ and therefore at 75°C the solubility of $Th(OH)_4(cr)$ is calculated by the equation

$$lg\, a_{Th^{4+}} = 9.63 - 4\,pH. \tag{15}$$

The solubility of $ThO_2(cr)$ and $Th(OH)_4(cr)$, calculated by Eqs. (13) and (15) (taking account of hydrolysis of thorium ions in solution), is shown in Table 2 and in Fig. 1.

The data obtained allow the following conclusions to be drawn: the most stable modification of thorium — thorianite — in the group of oxides and hydroxides is almost insoluble in the temperature and pH range of water of the weathering profile;

at elevated temperature, the point of electroneutrality of a thorium solution is displaced into the region of lower pH values;

thorium dissolved in sea water is found, apparently, in the form of the ions $Th(OH)_3^+$ and $Th(OH)_4^0$, and the latter should predominate;

in the bauxite formation process, the thorium initially formed in the original rocks must be accumulated, by which also is explained its enhanced coefficient of concentration in bauxites.

LITERATURE CITED

1. M. Yu. Gurvich, N. S. Parshakov, and L. N. Skosyreva, Izv. Vyssh. Uchebn. Zaved., Ser. Geol. Razv., No. 10, 38 (1974).
2. N. S. Parshakov et al., Izv. Vyssh. Uchebn. Zaved., Ser. Geol. Razv., No. 6, 32 (1976).
3. N. S. Parshakov et al., Izv. Vyssh. Uchebn. Zaved., Ser. Geol. Razv., No. 6, 25 (1977).
4. V. A. Tenyakov, in: Problems of the Origin of Bauxites [in Russian], Nedra, Moscow (1975), p. 18.
5. V. A. Tenyakov, in: Problems of Modern Lithology and Sedimentary Minerals [in Russian], Nauka, Novosibirsk (1977), p. 146.
6. V. A. Tenyakov and V. A. Kopeikin, in: Bauxites [in Russian], All-Union Institute of Mineral Resources, Moscow (1980), p. 199.
7. J. Adams and K. Richardson, Econ. Geol., 55, No. 8, 1653 (1960).
8. G. I. Bushinskii, Geology of Bauxites [in Russian], Nedra, Moscow (1975).
9. V. A. Kopeikin, Dokl. Akad. Nauk SSSR, 266, No. 5, 1264 (1982).
10. M. V. Pastukhova, Anomalies of Minerals of Iron Oxide and Hydroxide in Bauxites [in Russian], Nedra, Moscow (1981).
11. G. B. Naumov, B. N. Ryzhenko, and I. L. Khodakovskii, Handbook of Thermodynamic Quantities (for Geologists) [in Russian], Atomizdat, Moscow (1971).
12. O. V. Bryzgalin and R. P. Rafal'skii, Geokhimiya, No. 6, 839 (1982).
13. R. P. Rafal'skii, Geokhimiya, No. 12, 1780 (1982).
14. Handbook for Chemists [in Russian], Vol. 1, Khimiya, Leningrad (1966).
15. G. Akerlof and H. Oshry, J. Am. Chem. Soc., 72, No. 7, 2844 (1950).

LETTERS TO THE EDITOR

EXCITATION OF SURFACE VIBRATIONS OF DROPS

OF A RADIOACTIVE LIQUID

V. I. Kalechits, I. E. Nakhutin,
and P. P. Poluéktov   UDC 539.16.08:532.68

It was shown previously [1] that the disintegrations of radioactive materials in the near-surface region of solid macroscopic bodies accompanied by the effect of self-sputtering [2-4] lead to the excitation of natural vibrations, which can be recorded by measuring the correlation function of the scattered light. Moreover, the ideas presented in [1] may prove to be useful in the discussion of a drop of liquid containing some kind of radioactive material. The emission of fission fragments extracting and removing groups of molecules from the drop surface is accompanied by the transmission of momenta, which results in the excitation of natural vibrations of the drop shape. Just as in [1], the correlation function of the scattered light is proportional to $<\xi(t)\xi(t + \tau)>$, where ξ is the deviation of the drop radius from the equilibrium value.

Let the momentum K be imparted to the drop at the point of emission of a particle $(R_0, \varphi_0, \theta_0)$, where R_0 is the drop radius at the equilibrium position. Then the drop surface is described by the equation

$$R = R_0 + \xi = R_0 + \sum_{l=1}^{\infty} \sum_{m=-l}^{l} a_{lm} Y_{lm} \exp(i, \omega_l t),$$

where $\omega_l^2 = \gamma l(l - 1)(l + 2)/\rho R_0^3$ is the eigenfrequency of the drop vibrations and Y_{lm} are spherical functions. The motion of the liquid in the drop is determined by a velocity potential of the form

$$\psi(r, \theta, \varphi) = \sum_{l=0}^{\infty} \sum_{m=-l}^{l} \psi_{lm} \left(\frac{r}{R_0}\right)^l Y_{lm}(\theta, \varphi) \exp(i\omega_l t).$$

The initial equation for the velocity is

$$v_r = \frac{\partial \psi}{\partial r} = \frac{K}{\rho} \delta^*(A_0, A) \text{ at the point } A_0(R_0, \theta_0, \varphi_0); \quad v_r = 0 \text{ outside the point } A_0,$$

where the function $\delta^*(A_0, A)$ is such that the integral

$$\int \delta^*(A_0, A) f(A) r^2 \sin\theta\, d\theta\, d\varphi\, dr = f(R_0, \theta_0, \varphi_0) \text{ at the point } A_0.$$

When momentum is imparted to a liquid drop, not only surface vibrations but also body vibrations will be excited, for which the density (sound waves) increases [5, 6]. However, we shall consider drops with a radius $R \gg l_m$ (l_m is the mean free path of the fission fragments in the liquid); then transmission of momenta by virtue of fission fragments emitted from the drop and particles absorbed by them will occur only in the near-surface layer of the liquid with a thickness $\sim l_m$. In this case one can neglect excitation of body vibrations; therefore they are not discussed below.

Taking account of coupling on the surface $\dot{\xi} = \partial\psi/\partial r$, we obtain from the relationships given above after standard calculations that when the momentum K is imparted to the drop at point A_0 at time $t = \tau$ vibrations of its surface are excited:

$$R(r, \theta, \varphi, t) = R_0 + \sum_{l=1}^{\infty} \sum_{m=-l}^{l} \frac{(l+2) K Y_{lm(0)} Y_{lm}}{\rho R_0^3 \omega_l \| Y_{lm} \|^2} \sin\omega_l(t-\tau)\, \eta(t-\tau) \exp[\beta_l(t-\tau)],$$

where the function $\eta(t - \tau)$ takes into account the fact that $R = R_0$ for $t \leqslant \tau$; $Y_{lm(0)} = Y_{lm}(A_0)$; and $\| Y_{lm} \|$ is the norm of the spherical function. The exponential function describes the damping of the shape vibrations with the coefficient β_l.

246

If the disintegrations occur with equal probability at arbitrary points of the surface layer of the drop, the momenta K_i are imparted to the drop at the times τ_i at the points $(R_0, \theta_i, \varphi_i)$. Using the computational procedure previously outlined [1], we obtain for the correlation function $Z(\tau) = \langle \xi(t)\xi(t + \tau) \rangle$ the expression

$$Z(\tau) = \frac{1}{(\rho R_0^3)^2} \sum_{l, m} \frac{(l+2)^2 Y_{lm}^2}{\omega_2^2 \| Y_{lm} \|} \exp(-\beta_l \tau) \cos \omega_l \tau \; \overline{K_i^2} \langle \sum_i \eta(t - \tau_i) \exp[-2\beta_l(t - \tau_i)] \rangle,$$

where the averaging is performed over the time of emission, the imparted momentum, and the emission site for a time much greater than the vibration period of the drop shape and the damping time $\sim\beta_l^{-1}$ (assuming $\omega_l \gg \beta_l$). Let n_0 atoms of the disintegrating material be contained in unit volume of the drop; then the number of disintegrations accompanying the transfer of momentum to the drop per unit time will amount to

$$\frac{b}{2} \frac{4\pi R_0^2 l_m n_0}{T_{1/2}},$$

where $T_{1/2}$ is the half-life and b is a geometrical factor which takes account of the ratio of the fission fragments emitted outwards to all the disintegrating atoms (for α-decay b = 0.5). Then after the calculations of the expression for η we finally obtain, similarly to [1], for the correlation function

$$Z_l(\tau) = \frac{b\pi l_m n_0 \overline{K_i^2}(l+2)}{\rho R_0 \beta_l T_{1/2} l(l-1)} \exp(-\beta_l \tau) \cos \omega_l \tau \sum_{m=-l}^{l} \frac{Y_{lm}^2(\theta, \varphi)}{\| Y_{lm} \|}.$$

Let us estimate the expected amplitude of the vibrations in the shape of a drop 100 μm in radius of a 0.01% aqueous solution of ^{244}CmCl$_3$. The half-life of ^{244}Cm is 17.6 years; the emitted α-particles have an energy of 5.8 MeV and a momentum K = $0.88 \cdot 10^{-14}$ g·cm/sec. However, since each fission fragment emitted outwards carries away up to 10^8 atoms of the matrix [3], a momentum $K_i \approx \sqrt{2ME}$ is imparted to the drop in this case (where M is the mass of the fragment), which is accordingly equal to $\sim 10^{-10}$ g·cm/sec. Let us consider the fundamental $(l = 2)$ vibrations in the drop shape. Their frequency amounts to $\omega_2 \approx 3.8$ kHz with a damping $\beta_2 \approx 10$. The number of disintegrations accompanying the emission of particles is $\sim 10^7$ sec^{-1} for the indicated drop sizes. Then we obtain

$$Z_2(\tau) \approx 10^{-9} \exp(-0.1\tau) \cos \omega_2 \tau \; [\text{cm}^2]$$

for the correlation function. Thence the maximum amplitude of the vibrations (at the time $\tau = 0$) will be equal to $\sqrt{Z_2} \approx 3 \cdot 10^{-5}$ cm, i.e., approximately 10^3 times greater than the amplitude of the thermal vibrations of the drop [7].

Thus, by recording the correlation function of the light scattered by the vibrations in the shape of a drop containing disintegrating radioactive material, one can determine both the frequency and the damping time of the vibrations (consequently, the geometrical sizes of the drop and the physical parameters of the material) and the characteristics of the radioactive disintegration (the average momentum of the fragments $\overline{K_i^2}$, the content of unstable atoms n_0, etc.). The appreciable amplitude of the shape vibrations will permit avoiding experimental difficulties when making such measurements. The proposed procedure can be generalized to the case of a flat liquid surface. The ideas presented can be taken as the basis of a contact-free method for the determination and monitoring of the activity of solutions.

LITERATURE CITED

1. V. P. Kalechits et al., At. Energ., 51, No. 4, 261 (1981).
2. F. S. Lapteva and B. V. Ershler, At. Energ., 1, No. 4, 63 (1956).
3. V. K. Gorshkov and L. P. L'vov, At. Energ., 20, No. 4, 327 (1966).
4. B. M. Aleksandrov et al., At. Energ., 33, No. 4, 821 (1972).
5. L. D. Landau and E. M. Lifshits, The Mechanics of Continuous Media [in Russian], Gostekhteorizdat, Moscow (1954).
6. A. Bohr and B. R. Mottelson, Nuclear Structure, W. A. Benjamin (1969).
7. Yu. A. Bykovskii et al., Zh. Prikl. Spektrosk., 23, 866 (1975).

HEATING OF THE FOCUSING OPTICS OF LASER THERMONUCLEAR
REACTORS BY X-RAY RADIATION FROM THE TARGET

N. I. Belousov, P. A. Grishunin,
V. I. Subbotin, and V. V. Kharitonov

UDC 621.039.6:537.531.9

The output elements of the focusing system of a laser thermonuclear reactor (lenses or mirrors) will be subjected to the thermal action not only of the laser radiation initiating the thermonuclear reaction, but also of products of the explosion of the target: neutrons, x-ray photons, charged particles, and shock waves [1-3]. However, due to the low penetrability of low-energy x-ray radiation from the thermonuclear target and the short duration of the pulse (10^{-11}-10^{-10} sec), its thermal action will be most dangerous [4-6].

The energy from the x-ray pulse absorbed by the focusing elements can exceed by factors of 10 the energy absorbed from the laser radiation. According to [4], the x-ray radiation spectrum of thermonuclear targets falls between the spectrum of a blackbody with a temperature of 0.1-5 keV (depending on the energy of the explosion and the composition and mass of the target) and the spectrum of Bremsstrahlung from completely ionized hydrogen plasma with a temperature of tens of keV. Thus the most probable region of energies of x-ray photons absorbed by the optics is 100 eV-100 keV. Here, the dominant mechanism for absorption of x-ray radiation in the material is the photoeffect on atomic electrons.

Under the assumption that the attenuation of the flux of photons with energy ε at a depth x obeys an exponential law $\exp(-\mu(\varepsilon)x)$, we calculated the values of the mean free path of photons $1/\mu$ for a number of optical materials. In the calculations we used the total cross sections for interaction of x-ray radiation with separate elements, taken from [7]. The results of the calculations are presented in Fig. 1.

With exponential attenuation of radiation in the material, the heating of the surface S of metallic mirrors or transparent lenses by an x-ray pulse with total energy E, spectrum $W(\varepsilon)$, and duration t will constitute [5]

$$\Delta T = \frac{E}{S\rho C_p} \int_{\varepsilon=0}^{\infty} \frac{\mu(\varepsilon)}{u^2} \left(e^{u^2}\, \mathrm{erfc}\, u + \frac{2u}{\sqrt{\pi}} - 1 \right) W(\varepsilon)\, d\varepsilon, \tag{1}$$

where $u(\varepsilon) = \mu(\varepsilon)\sqrt{at}$ is the ratio of the distance over which the heat diffuses $\sqrt{at}$ and the mean free path of photons $1/\mu$; $a = K/\rho C_p$ is the thermal diffusivity; ρ is the density; C_p is the heat capacity; K is the thermal conductivity; and the spectrum of radiation is normalized to 1, i.e.,

$$\int_0^{\infty} W(\varepsilon)\, d\varepsilon = 1.$$

Taking as the upper limit of the temperature of the surfaces of mirrors or lenses the melting temperature of their materials, we can determine from Eq. (1) the maximum possible energy density E/S of the x-ray pulse, absorbed by the focusing optics. It is useful to express this quantity in terms of the most important parameters of the target: E_l, the energy of the laser pulse; Q, the energy gain in the target; γ, the fraction of the energy of the explosion converted into x-ray radiation; and the focal length F. Then

$$E/S = \gamma E_l Q/4\pi F^2. \tag{2}$$

From expressions (1) and (2) we find the minimum focal length as a function of the parameters of the thermonuclear target, the spectrum of the x-ray radiation, and the physical properties of the materials of the focusing optics:

$$F = \sqrt{\frac{\gamma E_l Q}{4\pi\rho C_p |\Delta T|} \int_0^{\infty} \frac{\mu(\varepsilon)}{u^2} \left(e^{u^2}\, \mathrm{erfc}\, u + \frac{2u}{\sqrt{\pi}} - 1 \right) W(\varepsilon)\, d\varepsilon}. \tag{3}$$

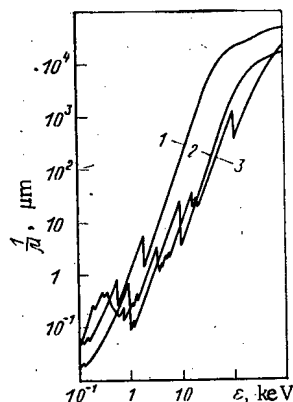Here $[\Delta T]$ is the maximum admissable heating of the surface.

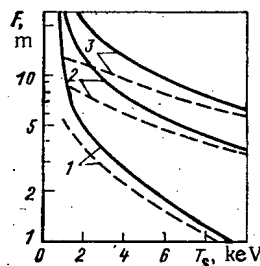Fig. 1   Fig. 2

Fig. 1. Dependence of the mean free
path of x-ray photons on energy: 1)
quartz (SiO_2); 2) copper; 3) ThF_4.

Fig. 2. Dependence of the minimum ad-
missable focal length of a quartz lens
(1), copper mirror (2), and a mirror
with a coating made of ThF_4 (3) on the
temperature of the x-ray spectrum: ——)
shows the calculation for unshielded op-
tics; ———) shows the calculation with
shielding by xenon pressurized at 25 Pa.

Figure 2 shows the dependences of F on the temperature of the spectrum T_S for a copper
mirror, quartz lens, and a reflective coating made of ThF_4 with an energy of 500 mJ in the
explosion, an x-ray yield of $\gamma = 5\%$, and pulse duration 10^{-11} sec, obtained from the formula
(3). In the calculations we used the radiation spectrum of a black body $W(T_S, \varepsilon)$ with temper-
ature T_S. In the case of low-energy x-rays $(T_s \leqslant 1 \text{ keV})$, characteristic for structured targets
[4, 6], the focusing elements must be separated from the latter by a distance of several tens
of meters. It should be noted that the use of long-focal-length optics in laser thermonuclear
fusion is problematical due to the relatively high divergence of the radiation from powerful
lasers [1].

For thermal shielding of the first wall and of the focusing optics of the reactors, it is
proposed [2, 3] that gases with comparatively high atomic numbers, for example, xenon, be
used. The pressure of the gas must be low enough to avoid its breakdown by the laser radia-
tion and to decrease scattering by density fluctuations. Helium and neon have the highest
thresholds for laser breakdown [3, 6]. However, the absorption of x-ray radiation by these
gases is small. For this reason, xenon is the optimum gas to use for gaseous shielding. The
focal length of the output optics in this case can be determined from the solution of the
transcendental equation obtained from expression (3) by substituting into the integrand the
fraction of the radiation passing through the gas $\exp[-\mu_{gas}(\varepsilon)F]$. The use of gaseous shield-
ing from low-energy x-ray radiation (see Fig. 2) lowers the heating of the optics and decreases
the focal length by a factor of 2-4. For high-energy x-ray radiation, however, such shield-
ing is ineffective.

LITERATURE CITED

1. N. G. Basov et al., Izv. Akad. Nauk SSSR, Energ. Transport, No. 2, 3 (1979).
2. M. Mousler and J. Maniscalo, in: Tech. Paper Top. Meeting, WC-5, San Diego (1978), p. 1.
3. R. Conn et al., SOLASE, A Laser Fusion Reactor Study, UWFDM-220A, Madison (1977).
4. T. Frank, AIChE Symposium Series, 73, No. 168, 77 (1977).
5. V. I. Subbotin et al., At. Energ., 55, No. 1, 37 (1983).
6. H. Karow and S. Abdel-Knalik, High Temp.—High Pressures, 12, No. 4, 373 (1980).
7. W. Veigele, At. Data Tables, 5, No. 1, 5 (1973).

249

AN EVACUATED EMISSION DETECTOR WITH EXTERNAL SUPPLY
SOURCE FOR RECORDING γ RADIATION IN NUCLEAR REACTORS

S. V. Chuklyaev and O. I. Shchetinin

UDC 539.1.074.8

Evacuated emission detectors [1, 2] are widely employed for recording ionizing radiations. During the interaction of γ radiation with matter, fast electrons are generated and, while they are slowed down inside a material, form slow secondary electrons with an energy <50 eV. The number of the secondary electrons per unit dose is independent of the energy of the primary radiation. Part of the slow secondary electrons which are generated in a $\sim 1 \cdot 10^{-6}$-cm-thick surface layer of the emitter material pass into the interelectrode detector space and are collected on a collector by an applied electric field. It has been shown in [3] that at a γ-radiation energy in excess of a few kiloelectron-volts, the dose rate is practically constant throughout the near-surface layer of the emitter material and the detector signal is proportional to the rate of the dose absorbed in this layer. Since the time constant of the generation and exit of the slow secondary electrons is small and does not exceed $1 \cdot 10^{-11}$ sec [4], the time resolution at the detector is given by the time of electron collection at the collector and amounts to $\sim 1 \cdot 10^{-9}$ sec. The amplitude characteristic is linear up to radiation dose rates of $\sim 1 \cdot 10^{13}$ rad/sec (1 rad = 0.01 Gr). The detectors described below are promising for measurements of the time dependence of the dose rate produced by the γ radiation of pulsed nuclear reactors and high-power accelerators [5].

We consider in the present work the design of an evacuated emission chamber with a stainless steel emitter of slow secondary electrons. Stainless steel is a technologically suitable material for manufacturing such detectors (because stainless steel can be mechanically worked and welded); in addition, high vacuum can be maintained for a long time in stainless steel vessels. The material is characterized by a stable emission of slow secondary electrons under the influence of nuclear reactor radiation.

The detector consists of two plane-parallel electrodes mounted in a cylindrical housing with a wall thickness of 0.8 mm and an outer diameter of 50 mm (Fig 1). Each electrode is a set of five or six disks with a diameter of 44 mm and a thickness of 0.4 mm. The disks carry on their periphery protrusions, "tongues," which in the assembly of the secondary emission chamber enter into openings of carrier posts, and are bent and soldered to the posts by electric spot welding. The openings in the posts are situated so that a 1.6-mm gap is maintained between the disks of opposite electrodes. Each disk of one electrode is located between two disks of the other electrode. The total sensitive surface area of the electrodes is always 125 cm². The posts of opposite electrodes are insulated from each other and from the housing by supporting insulators made from the high-aluminous VK 100-2 ceramic. The insulators are inserted into special recesses in the detector flanges. The posts are connected by conductors with corresponding standard cermet current leads welded into one of the flanges. All metal components, except for the kovar bushings of the input leads, are made from 12Kh18N10T stainless steel which is widely employed in reactor technology.

In order to maintain the required residual gas pressure during storage and use of the detector, the flange portion of the detector contains a KNTsTs-16 gas absorber which cannot be evaporated. In order to maintain stable readings of the secondary electron chamber during its use, the emitter surface is prepared with great care. The emitter surface was carefully cleaned, annealed in vacuum at 900°C, and chemically etched; the detector was evacuated in a vacuum furnace at 450°C to a pressure below $1 \cdot 10^{-3}$ Pa. Changes in the yield of slow secondary electrons from the emitter are usually caused by changes in the structure of the surface layer or its work function [6]. Structural changes in the surface layer or its destruction are often observed in emitters coated with oxide film or having foreign materials adsorbed on the emitter surface. In these materials, the emission is with great probability increased by an external electric field.
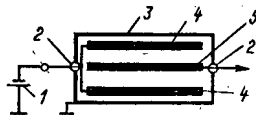
Fig. 1. Scheme of
the evacuated emis-
sion chamber: 1)
supply source; 2)
input leads; 3)
housing; 4) emit-
ter; 5) collector.
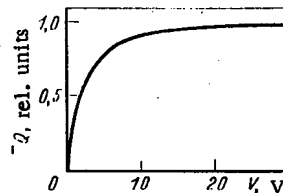
Fig. 2. Saturation
characteristic of
the evacuated emis-
sion chamber (at
V > 30 V, the slope
of the curve is
0.034%/V).
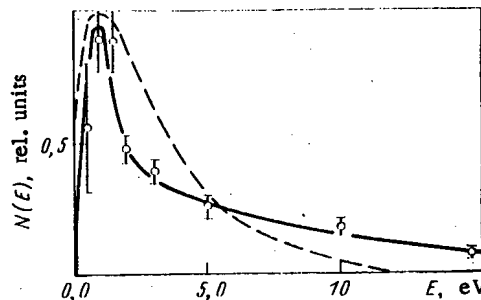
Fig. 3. Energy distribution of
the slow secondary electrons emit-
ted from stainless steel under
the influence of the γ quanta of
a ^{60}Co isotope source: ----) Max-
well distribution with the maxi-
mum at 1 eV; $\circ$) experimental re-
sults.

The emission of slow secondary electrons from the emitter surface was studied through
the detector saturation characteristic (Fig. 2) obtained with a ^{60}Co γ quantum source. It
follows from the theory of vacuum chambers [7] that the saturation characteristic Q(V) of a
secondary emission chamber with plane-parallel electrodes made of a single material is given
by the formula

$$-Q(V) = +Q(V) = \frac{eSD_{\gamma}k}{\int_0^\infty N(E)\,dE} \left[\int_0^V N(E)\,dE + \int_V^\infty \frac{V}{E} N(E)\,dE \right],$$

where D_γ denotes the averaged radiation dose absorbed in the material of the electrodes; k
denotes the number of slow secondary electrons emitted from a unit electrode area when the
unit dose has been absorbed; V denotes the potential difference between the emitter and the
collector; E denotes the energy of the slow secondary electrons; N(E) denotes the density of
the energy distribution of the slow secondary electrons; e denotes the electron charge; and

251

S denotes the electrode surface area facing the sensitive volume of the vacuum chamber. The signs + and − at Q denote the polarity of the voltage applied to the secondary emission chamber.

It follows from the above equation that

$$N(E) = -\frac{V}{eSD_\gamma k}\frac{d^{2-}Q(V)}{dV^2}.$$

The above formula and the saturation characteristic shown in Fig. 2 were used to obtain the energy distribution of the slow secondary electrons emitted from stainless steel subjected to the γ quanta of the ^{60}Co source (Fig. 3). The average electron energy in the distribution was 5.6 eV. This distribution approximately coincides with the distributions which were given in [8] for lead, copper, tin, aluminum, and carbon. This means that no abnormal emission mechanisms occur in the case of stainless steel to which an electric field is applied.

The sensitivity of the secondary emission chamber to the γ radiation of the ^{60}Co source was determined at the maximum of the saturation curve (V = 50 V) and is $(5.9 \pm 0.4) \cdot 10^{-12}$ C/rad. The signal contribution resulting from fast electrons to the total signal does not exceed a few percent. While the detector was used for two years on a pulsed nuclear reactor, detector sensitivity changes were not observed. Since stainless steel does not contain elements with a low work function of slow secondary electrons, noticeable sensitivity changes due to diffusion of atoms in the surface layer of the emitter must not be expected during the use of the detector under laboratory conditions.

The sensitivity of the secondary emission chamber to fast neutrons emitted by nuclear reactors is $\sim 1 \cdot 10^{-23}$ C·cm^2/neutron and, hence, the detector signal resulting from the neutrons does not exceed a few per cent when the ratio of the γ component to the neutron component of the radiation field is $4 \cdot 10^9$ neutrons/(cm^2·rad).

This design of the secondary emission chamber allows measurements of the time dependence of the dose rate generated by the γ radiation of a pulsed reactor; the accuracy is better than 10%. The errors result mainly from the error made in the determination of the sensitivity, the contribution of signals produced by fast electrons and fast neutrons to the detector signal, and the error produced in the detector signal recording by the oscillographic recording equipment.

We thank, in conclusion, M. G. Mitel'man, Ph.D. in engineering, who made several valuable comments on the present work.

LITERATURE CITED

1. T. Burlin, in: Topics in Radiation Dosimetry, Vol. 1, Academic Press, New York—London (1972), p. 144.
2. G. V. Kulakov, E. K. Malyshev, and O. I. Shchetinin, Evacuated Radiation Detectors [in Russian], Énergoatomizdat, Moscow (1982).
3. E. Burke, J. Wall, and A. Frederickson, IEEE Trans. Nucl. Sci., 17, No. 6, 193 (1970).
4. M. Greenblatt, RCA Rev., 16, No. 1, 52 (1955).
5. S. Kronenberg, High-Intensity Radiation Dosimetry with Semirad., Rep. 3, US Army Res. Developm. Lab. (1966).
6. I. M. Bronshtein and B. S. Fraiman, Secondary Electron Emission [in Russian], Nauka, Moscow (1969).
7. J. Greening, Brit. J. Radiol., 27, 163 (1954).
8. T. Burlin and S. Husain, Phys. Med. Biol., 13, 169 (1968).

INFLUENCE OF γ-QUANTUM SCATTERING UPON THE DEVELOPMENT

OF THE RADIATION FIELD OF A COBALT ISOTOPE UNIT

V. F. Zinchenko and M. N. Lebedev   UDC 621.039.8:539.122.08

At the present time γ units with ^{60}Co isotope sources are widely employed in research in various areas of radiation biology and chemistry, in dosimetry, and in investigations of the physics of radiation damage to materials and electronics components. In many cases a correct interpretation of the results of irradiation tests on various objects necessitates reliable information on the energy spectrum of the γ radiation of the unit; the contribution of the γ quanta scattered in the components of the unit and the objects in the neighborhood must be taken into account. Since information on the low-energy part of the spectrum resulting from scattered quanta is not available, a rather large error can be made in the calculation of the spectra of the linear energy losses of secondary electrons, calculation of the γ radiation energy absorbed in materials with medium and high atomic numbers Z and in heterogeneous compositions near the boundaries of various materials. For example, it has been shown in [1] that when the scattered gamma quanta of a cobalt isotope unit are taken into account, the energy absorbed within 100 μm from a gold—aluminum interface is increased by a factor of 1.5 relative to estimates made for the nonscattered radiation with the energy $E_\gamma = 1.25$ MeV.

The published experimental work [2, 3] attests to the noticeable contribution of scattered ^{60}Co quanta to the development of the space and energy dependent features of the γ-radiation field, which is strongly influenced by the design details of the particular isotope unit. The goal of the present work is therefore to provide a detailed computational investigation of the scattered γ radiation of a typical cobalt isotope unit used for various investigations in radiation physics wherein the real geometry of the source and of the experimental hall is taken into consideration.

Let us briefly consider the design features of the unit. The main component of the unit is the irradiator in the form of a hollow steel cylinder of variable diameter with a thin wall; the cylinder is placed on a solid brass support (see Fig. 1). Sixteen steel tubes (wall thickness about 2 mm) are uniformly distributed over the inner side of the irradiator periphery. Four standard GIK-7 ^{60}Co cobalt sources are mounted inside each of the tubes into which they enter from a storage compartment; the activity of a source is $7.2 \cdot 10^{13}$ Bq. The unit is mounted in an experimental compartment which is a rectangular room with monolithic concrete walls.

From this geometry one can draw the a priori conclusion that the large quantity of iron components must render a significant contribution of scattered γ quanta to the space and energy characteristics of the radiation field of the unit. Obviously, since the geometry is complicated, statistical testing is the best way of obtaining the characteristics. Therefore, in the present work the computational studies were made with one of the modifications of the method numerically practiced in the FASTER program [5]. The program makes it possible to calculate the flux components of the γ quanta in accordance with the order of scattering in any three-dimensional geometry for given pointlike surface or volume sources; various scalar flux quantities (dose rate, angular and spatial moments of the distributions, etc.) can also be computed. One of the advantages of the FASTER program is that optimal weight functions are used to select the values of the spatial and angular variables of the γ-quantum sources. In this way the dispersion of the calculated characteristics of the γ-radiation field is substantially reduced.

When the weight functions are selected, the "weight" of both the primary γ quanta of the source and the γ quanta multiply scattered by the components of the unit is taken into account in the quantities characterizing the radiation conditions at a particular point:

$$D_M(\mathbf{r}) = \int f(E_\gamma)\, \Phi_M(\mathbf{r},\, E_\gamma)\, dE_\gamma,$$
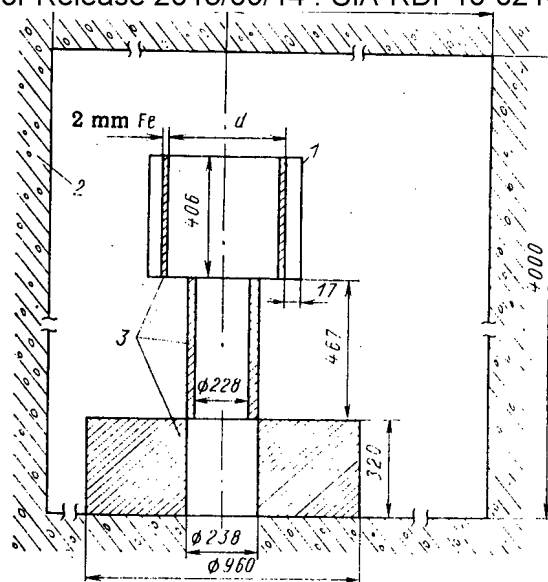
Fig. 1. Geometry of the cobalt unit:
1) 16 tubes; 2) concrete; 3) steel com-
ponents (all dimensions are stated in
millimeters).

where $f(E_\gamma)$ denotes a function accounting for the dependence of a contribution to $D_M(r)$ upon the γ quantum energy; and $\Phi_M(r, E_\gamma)$ denotes the energy spectrum obtained for the γ quanta with M-fold scattered quanta taken into account in the computations. The exposure dose is usually adopted as the reduced quantity.

This approach makes it possible to estimate the multiplicity M_0 of γ-quantum scattering at the surrounding objects and the structure of the unit above which it is meaningless to follow the trajectory of γ quanta because the contribution of the scattering with $M > M_0$ to the above quantity is negligibly small. The corresponding addition $D_{M>M_0}(r)$ was estimated in the single-velocity approximation with the "point nucleus" technique [5].

Let us also note that the coordinates of the primary γ-quantum source (coordinates in space, angular coordinates) were selected with proper regard for the relative "weight" of the variability limits of the angular variable, the attenuation of the radiation in the building materials, and self-absorption in the source. Thus, the correct use of the entire set of parameters of the random ensemble makes it possible to reach rather high precision with relatively short times of computer calculations. More particularly, the time required for working through one version ($\sim$3000 histories) is $\sim$1 h on an ES-1022 computer for the unit under consideration, when the structure of the unit is subdivided into 64 zones. The averaging made in the calculation of differential parameters of the γ-radiation field is 10%.

Calculations have confirmed the above conclusion that the γ-radiation spectrum of the unit is considerably softened in comparison with the nonscattered radiation. Figure 2 illustrates the results of a calculation of the energy density $\varphi(E_\gamma)$ of the γ-quantum flux in a particular multigroup approximation for the irradiator diameter $d = 390$ mm and at various points of detection. The error in the calculated grouped fluxes of the γ quanta is 10% near the maxima and 20% near the minima of the function $\varphi(E_\gamma)$.

The main contribution to the scattered component of the γ radiation originates from quanta scattered in the sources, the irradiator, or from the walls, and also from the brass support. The contribution of the scattered radiation to the total flux increases toward the wall and reaches $\sim$50-60% at a point in the immediate vicinity of the wall. It was established in an analysis of the results in which the scattered radiation of first and higher orders was included that the singly scattered γ quanta significantly contribute to the $\varphi(E_\gamma)$ distribution. The flux density of singly scattered γ quanta decreases with decreasing E_γ. The characteristic maximum at $E_\gamma \approx$ 0.15-0.25 MeV seems to result from multiply scattered radiation, as put into evidence by an examination of the results.

254

TABLE 1. Average Radiation Energy (MeV; numerator) and Contribution (%) of the Scattered Radiation (denominator) to the Total γ-Quantum Flux as Functions of the Distance from the Center of the Irradiator for Various Irradiator Diameters

d, mm	R, mm					
	0	80	300	700	1700	2100
240	$\dfrac{0,87}{47}$	$\dfrac{0,86}{50}$	$\dfrac{0,84}{49}$	$\dfrac{0,89}{44}$	$\dfrac{0,82}{49}$	$\dfrac{0,77}{56}$
390	$\dfrac{0,9}{44}$	$\dfrac{0,9}{45}$	$\dfrac{0,9}{46}$	$\dfrac{0,89}{43}$	$\dfrac{0,84}{46}$	$\dfrac{0,76}{56}$
540	$\dfrac{0,91}{44}$	$\dfrac{0,93}{42}$	$\dfrac{0,95}{41}$	$\dfrac{0,9}{43}$	$\dfrac{0,8}{50}$	$\dfrac{0,7}{60}$
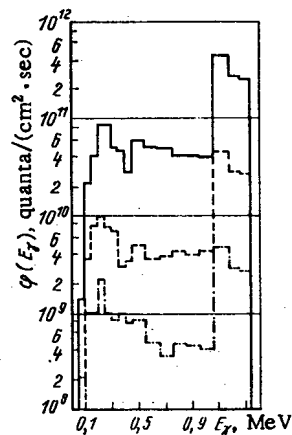
Fig. 2. Energy density of the γ-quantum flux at various points of detection on half the height of the irradiator at R = 0 (center of the irradiator) (——); 700 (— — —); and 2100 mm (—•—•—).
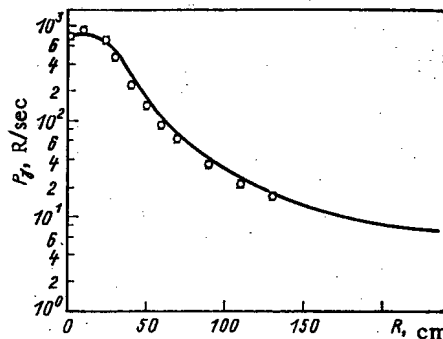
Fig. 3. Dependence of the exposure dose rate upon R at d = 390 mm; —— refers to the calculations; ○ refers to experiments (1 R = $2.58 \cdot 10^{-4}$ C/kg).

255

Table 1 lists the average energy values

$$\overline{E}_\gamma = \frac{\int E_\gamma \Phi\,(E_\gamma)\,dE_\gamma}{\int \Phi\,(E_\gamma)\,dE_\gamma}$$

and the contribution δ of the scattered radiation to the total γ-quantum flux

$$\left(\delta = \frac{\Phi_{sc}\cdot 100}{\Phi_{nonsc}+\Phi_{sc}}\ \% \right)$$

for various diameters of the irradiator in the direction toward the nearest wall. It follows from the listed results that the average energy of this unit is 0.7-0.9 MeV and is practically independent of the diameter of the irradiator. The error which is made in the determination of the integral parameters of the γ-radiation field amounts to 5-10% (see Table 1).

Since experimental information on the γ-radiation spectra of the isotope unit under consideration is not available, the calculated integral dose quantities were compared with experimental data obtained with the aid of a ferrosulfate dosimeter (see Fig. 3). The results coincide within the error limits of the calculation and of the experiment. This is an indirect confirmation of the validity of the calculated differential characteristics of the γ-radiation field.

Our investigations have therefore shown that the scattered γ quanta are important in the development of the radiation field of a cobalt unit. These results must obviously be taken into account in precision dosimetry, radiobiological investigations, and other research in radiation physics when radiation fields of similar isotope units are present.

We thank É. B. Brodkin for the help in making us familiar with the FASTER program and M. B. Moshchevitina for her collaboration in compiling the experimental information.

LITERATURE CITED

1. J. Garth and E. Burke, IEEE Trans. Nucl. Sci., NS-27, 1459 (1980).
2. M. Ehrlich, S. Seltzer, and M. Bielefeld, Metrologia, 12, 169 (1976).
3. J. Dod, Measurement Techniques, 19, 740 (1976).
4. Alpha-, Beta-, and Gamma-Neutron Radiation Sources [in Russian], V/O "Izotop," Moscow (1973).
5. T. Jordan, Nucl. Eng. Design, 13, 415 (1970).

ESTIMATE OF THE CORROSION RESISTANCE OF CHROME–NICKEL STEELS IN MOLTEN FLUORIDES

V. B. Kirillov, I. E. Lyublinskii, and N. M. Beskorovainyi

The alloy LiF–BeF$_2$ (Flaib) is considered as one of the possible coolants for the blankets of a thermonuclear reactor [1], in connection with which there arises the necessity of selection of corrosion-resistant structural materials, exceeding steel 1Kh18N10T in this respect. For the direct determination of the corrosion resistance of structural materials in an alloy of fluorides, as is well known, prolonged and laborious experiments are necessary, and therefore it will be advantageous to preliminarily assess prospective materials. As is well known [2], corrosion of 1Kh18N10T steel in a fluoride alloy is determined by the conversion of chromium in the alloy according to the reaction

$$m\mathrm{Cr}_{\text{(solid soln.)}} + 2MF_m\,_{\text{(liq.)}} \rightleftharpoons m\mathrm{CrF}_2\,_{\text{(liq.)}} + 2M\,_{\text{(liq.)}}. \qquad (1)$$
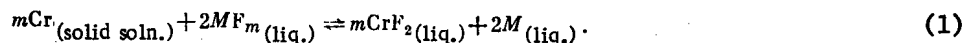
As the interaction of the alloys with corrosive media is characterized by the thermodynamic activity of the components, it is advantageous to use steels, in which the thermodynamic activity of chromium will be less than in 1Kh18N10T steel.

Information about the activity of chromium in multicomponent alloys based on iron is available only for the system Fe–Cr–Ni at temperatures of $\geq 900°C$ [3, 4]. The method proposed earlier for determining the thermodynamic activity of the components of alloys, based on the

TABLE 1. Chemical Composition of Materials Investigated, mass %

Steel	C	Si	Mn	Cr	Ni	Mo	Nb	Ti	B
1Kh18N10T	0,07	1,15	0,50	18,59	10,48	--	—	0,49	—
1Kh21N5T	0,07	0,66	0,65	20,33	5,55	—	—	0,41	—
Kh20N14S2	0,08	2,43	0,82	19,49	13,67	—	—	—	—
Kh20N30V5M3	0,04	0,6	0,51	20,57	27,64	3,2	1,0	5,4W	$< 5 \cdot 10^{-3}$
0Kh16N15M3B	0,06	0,48	0,43	16,68	15,2	2,8	0,63	—	$3 \cdot 10^{-5}$

TABLE 2. Parameters of the Temperature Dependence [Eq. (3)] of the Thermodynamic Activity of Chromium in Steels

Steel	Temp., °C	A	B
1Kh18N10T	825—1025	$-2,53 \pm 0,18$	$2,66 \pm 0,22$
1Kh21N5T	825—950	$-1,27 \pm 0,68$	$1,09 \pm 0,78$
Kh20N14S2	825—975	$-1,31 \pm 0,29$	$1,30 \pm 0,34$
Kh20N30V5M3	825—975	$-1,78 \pm 0,49$	$1,90 \pm 0,57$
0Kh16N15M3B	825—975	$-1,93 \pm 0,29$	$2,00 \pm 0,34$
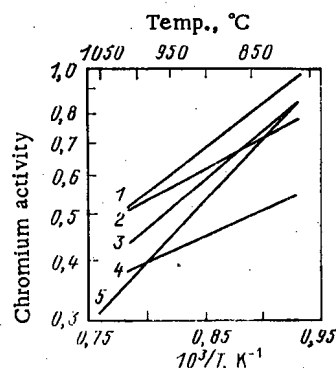
Fig. 1. Temperature dependence of the thermodynamic activity of chromium in chrome— nickel steels Kh20N30-V5M3 (1); Kh20N14S2 (2); 0Kh16N15M3B (3); 1Kh21N5T (4), and 1Kh18N10T (5).

high-accuracy determination of the equilibrium solubility of metals in lithium of high purity [5], gives the possibility of finding the thermodynamic activity of chromium in alloys based on iron at a temperature of ∿800–1000°C [6], and obtaining an analytical dependence in this way of the thermodynamic activity of chromium on the concentration of elements in the alloys (C, mass %) and temperature (T, °K), adequately describing the experimental results at a temperature of 825–975°C and a concentration of chromium and nickel of 8–18 mass %:

$$\lg a = -2.15 + 0.035 C_{Cr} + 0.0075 C_{Ni} + 1.315 \cdot 10^3 / T. \tag{2}$$

Relation (2) allows to a first approximation (without taking account of the effect of additional alloying elements) the thermodynamic activity of chromium to be determined in purely austenitic chrome—nickel steels.

The results obtained (Fig. 1) for a number of industrial chrome—nickel steels, the chemical composition of which is given in Table 1, are described by expressions of the type

$$\lg a = A + B \cdot 10^3 / T. \tag{3}$$

lne values of the constants A and B found by the method of least squares, taking account of the statistical weight of individual measurements, are given in Table 2.

Comparing the results of the calculation of the thermodynamic activity of chromium according to Eq. (2) with the experimental data for different steels, the conclusion can be drawn that additional alloying of Fe—Cr—Ni alloys on the whole slightly enhances the thermodynamic activity of chromium.

The minimum thermodynamic activity of chromium at a temperature of $\sim$1000°C is possessed by steel 1Kh18N10T, and at 800–900°C by steel 1Kh21N5T.

LITERATURE CITED

1. V. G. Vasil'ev, Z. V. Ershova, and E. V. Dmitrievskaya, At. Energ., 48, No. 5, 283 (1980).
2. V. B. Kirillov and V. I. Fedulov, Fiz.-Khim. Mekh. Mater., 16, No. 6, 62 (1980).
3. F. Mazandarany and R. Pehlke, Met. Trans., 4, No. 9, 2067 (1973).
4. W. Slough, P. Spencer, and O. Kubaschewsi, J. Chem. Thermodyn., 2, 117 (1970).
5. N. M. Beskorovainyi, V. K. Vasil'ev, and I. E. Lyublinskii, in: Metallurgy and Metallography of Pure Metals [in Russian], Issue 14, Atomizdat, Moscow (1980), p. 135.
6. N. M. Beskorovainyi et al., Fiz.-Khim. Mekh. Mater., 16, No. 3, 59 (1980).

KINETICS OF THE BEHAVIOR OF SODIUM ACETYLIDE
IN A SODIUM—MINERAL OIL SYSTEM

Yu. P. Kovalev and N. V. Gavrilova

At the present time, sodium is being used as the coolant in the primary and secondary circuits of nuclear power stations with fast reactors. The purity of the coolant with respect to the many impurities, including carbon, is strictly regulated. One of the potential sources of carbon is mineral oil, used for lubrication and cooling of the bearings of the centrifugal pumps which pump the sodium round. An excessive content of carbon in the sodium can lead to carbonization of the structural materials of the reactor core and, consequently, to their embrittlement.

It has been established that stainless steels in contact with sodium containing mineral oil are carbonized to a higher degree than in the case of contamination of the sodium with carbon or graphite [1, 2]. During interaction of the sodium with hydrocarbons of a saturated nature, in addition to sodium—organic compounds, the formation of sodium acetylide is possible [3], which at a temperature above 500°C becomes thermodynamically unstable in the sodium [4]. Nevertheless, being an intermediate product of the sodium—oil reaction, it can exist in the coolant for a time which is sufficient for the carbonization of austenitic steels, in particular those containing carbide-forming alloying additives. Data about the kinetics of the behavior of sodium acetylide in sodium are necessary for estimating the transfer of carbon from the free surface of sodium in the pump (after oil enters it) into the coolant flow.

The results were published earlier of an investigation of the behavior of gaseous products of pyrolysis of the oil used in the pumps, in the presence of sodium at 350°–700°C [5]. The results are given in the present paper of a study of the composition of the condensed phase in the course of the sodium—oil reaction in the same temperature range in ampule conditions.

Experiment. A vacuum oil was used for the experiments, represented by a mixture of paraffin—naphthene hydrocarbons of narrow fractional composition. Weighed amounts of previously dried oil were deposited on the inside surface of small nickel cups. Sodium of reactor purity, supplied to a fast reactor type facility, was used in the experiments. Before filling the ampules, it was purified additionally in a cold trap.
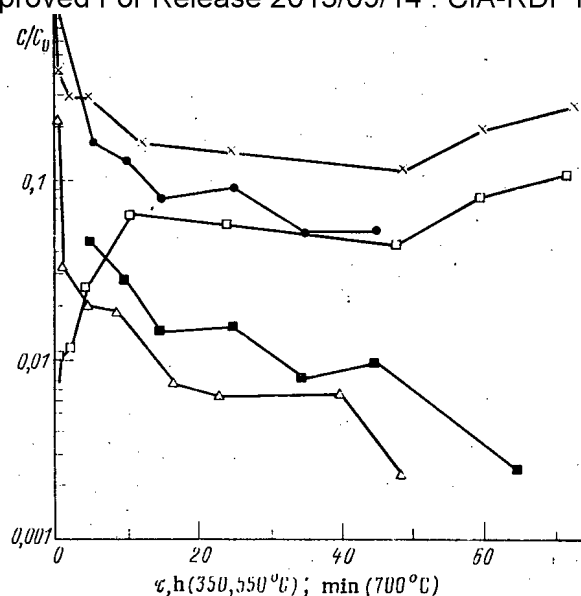

Fig. 1. Behavior of carbon acetylide
(□, △, ■) and carbon in forms soluble in
chloroform (×, ●), at 350° (□, ×), 550° (△)
and 700°C (■, ●).

Hermetic sealing of the ampules (nickel tubes with a diameter of 6 and length 60 mm) was effected by crumpling the ends of the tubes and subsequent welding. The volume of the ampule after welding the ends amounted to ~1 ml. The oil was placed in the ampule together with the small cup.

The facility for exposing the ampules was a horizontal tubular furnace, in the center of which was installed coaxially a cassette with ten cells round the periphery. The ampules were placed in nine cells, and an imitation ampule with a microthermocouple was placed in the tenth. The cassette, during exposure, was rotated so that mixing of the contents of the ampules took place.

After removal from the furnace, the ampules were cooled to room temperature, opened and placed in a metal reaction flask, equipped with a unit for the entry of water and two nozzles for purging the flask with gas. The contents of the ampuls were quenched with water. The acetylene released by the interaction of the sodium acetylide with water was absorbed with the reagent Ilosvaya, the optical density of which was measured on a photoelectrocoulometer. The content of carbon acetylide was found from a calibration graph. Its limit of detection amounted to 0.6 μg and the relative error of a single measurement was 20%. The alkaline solution after quenching the contents of the ampules was treated with hydrochloric acid to pH = 4–5. Then, the hydrocarbons were extracted with chloroform, which was chosen as the extractant for two reasons: the original oil is completely soluble in chloroform, and the latter readily extracts hydrocarbons from aqueous solutions with an acid reaction. After evaporation of the chloroform, the carbon in the samples was determined quantitatively by the method of high-temperature combustion above copper oxide with potentiometric recording of the carbon dioxide formed. The limit of detection of carbon in the forms soluble in chloroform was 10 μg and the relative error of a single measurement was 15%.

Results and Discussion. In the analysis of the original sodium, neither carbon acetylide nor carbon in forms soluble in chloroform was detected. The results of the chemical analyses are shown in Fig. 1. The time of exposure of the ampules, expressed in hours for 350 and 550°C and in minutes for 700°C, is plotted along the abcissa, and along the ordinate axis are plotted the ratios of the quantity found of carbon acetylide and carbon soluble in chloroform to the initial quantity of this element in the weighed batch of oil.

It can be seen from the figure than on scaling to the carbon introduced, up to 10–20% of carbon acetylide is formed. The nature of the kinetic curves confirms that sodium acetylide is an intermediate product in the chain of reactions taking place. Its content increases relatively rapidly up to a maximum (in less than 30 min at 550°C), and then decreases slowly. The behavior kinetics of sodium acetylide depends on the temperature. At 350°C (the tempera-

259

ture which is characteristic for a sodium pump of a sodium circuit) the content of carbon acetylide after 3 h increased and amounted to ∿10% of the carbon introduced. The fluctuations of the curve, obviously, are due to errors of the charge, exposure and opening of the ampules, which is confirmed by the correlated path of the kinetic curve of the content of carbon in forms soluble in chloroform. At 550°C (intermediate heat exchanger between the primary and secondary sodium circuits), for this same time a descending branch of the curve is obtained, and after 2 days the content of carbon acetylide was reduced to 0.3–0.5%. At 700°C (reactor core), the behavior kinetics of the acetylide is determined with a time less by a factor of 50–60 than at 550°C.

The measurements of the content of carbon in forms soluble in chloroform at 350° and 700°C show that at first it decreases relatively rapidly. Then this content varies slowly in the range 5–20%, which confirms the reduction of the reaction capabilities of the remaining part of the hydrocarbons.

In order to estimate the effect of sodium on the pyrolysis process of oil at 630°C, a 20-min exposure of an ampule not containing weighed amounts of sodium was carried out. Neither carbon acetylide nor carbonaceous forms soluble in chloroform were found, which confirms the total destruction of the oil. This coincides with the data of [6] concerning the suppression with molten sodium of cracking of hydrocarbons of the paraffin and naphthene series.

Conclusions. During the exposure with sodium in ampule conditions over 2–3 days at 350–500°C and 1 h at 700°C of mineral vacuum oil, not containing aromatic hydrocarbons, carbon acetylide is formed to the amount of ∿20% (550°C) scaled to the carbon in the original oil.

Sodium acetylide, which is an intermediate product, at 550–700°C in the presence of excess sodium is decomposed, and the change of its content by 1.5–2 orders takes place after 1 h at 700°C and after 2 days at 550°C.

LITERATURE CITED

1. O. V. Starkov, B. A. Nevzorov, and I. N. Luk'yanov, Zashch. Met., 7, No. 6, 674 (1971).
2. A. Raine and A. Thorley, in: Specialists Meeting on Carbon in Sodium, IAEA, IWGFR/33, 13 (1980).
3. A. V. Topchiev et al., Izv. Akad. Nauk SSSR, Ser. Khim., No. 10, 1838 (1960).
4. É. E. Konovalov. A. P. Smirnov-Averin, and A. I. Lastov, Preprint FÉI-806 [in Russian], Obninsk (1978).
5. F. Kozlov et al., in: Specialists Meeting on Carbon in Sodium, IAEA, IWGFR/33, p. 36 (1980).
6. Ya. M. Paushkin, Yu. P. Losev, and P. G. Anan'ev, Izv. Akad. Nauk SSSR, Ser. Khim., No. 6, 1276 (1969).

ANALYSIS OF AN EMERGENCY INVOLVING RUPTURE
OF THE MAIN CIRCULATION PIPELINE IN THE VVÉR-1000

A. I. Boyadzhiev and S. I. Stefanova

UDC 621.039.586

Coolant loss emergencies (CLE) have been examined since 1974 in relation to the design and licensing of nuclear power stations operating with pressurized-water reactors (PWR or VVÉR types) [1, 2]. Such a hypothetical emergency involving failure in the main coolant pipe has been called a maximal design emergency. Three stages are distinguished: decompression of the first loop with coolant loss, filling of the lower mixing chamber (LMC) with water from the emergency cooling system (ECS), and repeat analysis for the active zone.

There are many theoretical and experimental studies on PWR [3-5] and VVÉR-440 [6-8] on outflow during CLE. During this stage there are heavy mechanical loads on the equipment within the containment over a millisecond period and large thermal loads on the fuel pins over intervals of seconds. There should be no damage to the equipment within the containment as a result of the deformation of the fuel-pin cladding, nor should there be any substantial blocking of the flow cross section in the core that could lead to meltdown in the subsequent stages. The thermal stresses on the fuel cladding are due to the heat-transfer crisis during the coolant stagnation, which may occur at this stage from pump overshoot in the forward direction and in the reversed direction because of the pressure fall in the core when the pipe breaks.

Theoretical analysis of CLE in pressurized-water reactors may be based on various computer programs, of which the best-known are RELAP 4 in its various forms [9-11] and the programs BRUKh, TECh', etc. Here we consider CLE in a VVÉR-1000 due to failure in the Du850 main circulation pipe at the inlet near the reactor. We use the RELAP 4/MOD 6 program as the most thoroughly tested and as suitable for analyzing CLE. The study has been made in relation to the proposed construction of nuclear power stations containing VVÉR-1000 in Bulgaria.

In the RELAP 4/MOD 6 algorithm, the first loop is slpit up into 35 control volumes and 45 links between them (see Fig. 1 in the paper by Boyadzhiev and Stefanova "Shock loads on units within the containment in the VVER-1000 in the initial stage of an emergency involving failure in the main circulation pipeline," this issue, p. 264). The geometrical and thermal and hydraulic characteristics are then very close to the real ones. The circuit is represented by two circulation loops: the emergency and combined ones, which includes three unbroken loops; the core is represented by a single undeformable fuel pin with four energy-producing zones along the height and with the average linear power for the reactor of about 170 W/cm.

The CLE is considered with the following boundary conditions:

1) failure in the Du850 pipe in the loop to which the volume compensator is connected will be simulated by links 32, 33, and 34, where at the start ($\tau = 0$) link 32 is open and closes virtually instantaneously at $\tau = 1 \cdot 10^{-4}$ sec, while links 33 and 34 are closed and open completely in $15 \cdot 10^{-3}$ sec;

2) the change in the relative power production after the start of the CLE is given in the curve of Fig. 1;

3) the main circulation pumps (MCP) are deenergized within 1 sec after the start of the CLE, and their overshoot is incorporated;

4) the steam-generating (SG) volumes in the second loop are cut off during the second second after the start of the CLE;

5) the hydraulic accumulators in the ECS are switched on when the pressure falls in the upper mixing chamber (UMC) and the lower one to values less than 6 MPa, while the emergency

261
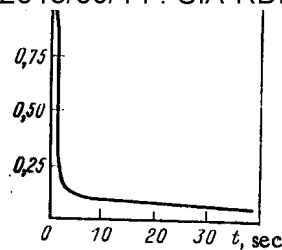
Fig. 1. Relative change in energy production.
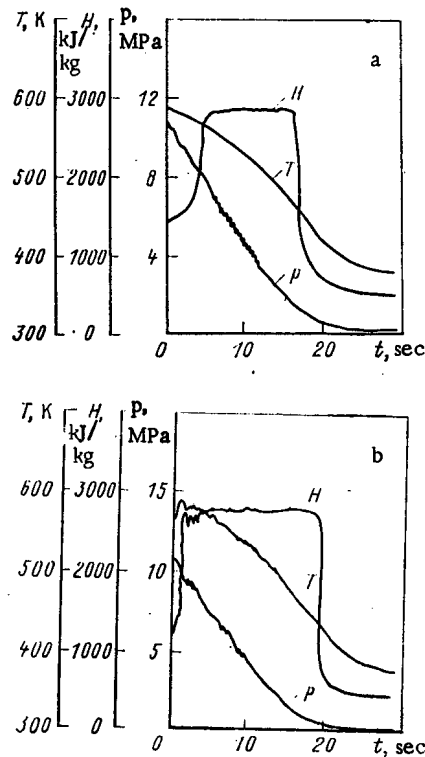
Fig. 2. Changes in pressure p, enthalpy H, and temperature T in the UMC (a) and LMC (b).

low-pressure pumps are switched on at 40 sec after the start of the CLE; and

6) the heat flows through the walls of the equipment in the first loop are not incorporated because the process is of brief duration.

We now consider the most important results for CLE in the VVÉR-1000. The outflow stage lasts about 25 sec until the pressures in the first loop and inside the shield equalize. Immediately after pipe failure, critical coolant outflow begins, and as a result the pressure in the UMC and LMC falls rapidly to the saturation point (Fig. 2) at the initial temperature, which causes vigorous boiling in the core and a back pressure. On average, the pressure in the loop changes from 16 MPa to about 10 MPa in 0.1 sec, after which it falls slowly. The pressure in the steam generator (SG) from the second loop rises to about 6.9 MPa because of the SG shutoff and the heating of the stagnating coolant, and then falls somewhat because of the cooling in the first loop.

The coolant flow rate through the core varies during the first 5 sec; the sharp pressure fall and the boiling lead to a heat-transfer crisis and a temporary temperature rise in the fuel-element cladding (Fig. 3). At 5-15 sec after the start of the CLE, the back pressure in the core exceeds the reducing pressure from the decelerating pumps in the combined loop, so the flow reverses, which leads to a temporary improvement in the fuel-pin cooling. After 15-20 sec, although the amount of heat accumulated in the fuel is comparatively small, the coolant flow rate in the core becomes close to zero, so a heat-transfer crisis arises again

262
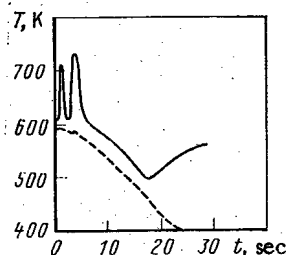
Fig. 3. Temperatures of coolant (dashed line) and rod surface (solid line).

at the fuel-rod surfaces. Therefore, at the end of the outflow stage, the temperature of the fuel and cladding tends to settle down, while the heat-transfer coefficient stabilizes at the level of 100 $W/m^2 \cdot K$.

The calculations imply that during the CLE in a VVÉR-1000, the medium-power rods do not attain either the melting point of the fuel (about 3000°K) or the critical temperature for the onset of plasticity in the zirconium cladding (about 1000°K).

LITERATURE CITED

1. A. M. Bukrinskii and V. P. Tatarnikov, Elektrich. Stantsii, No. 8 (1978).
2. J. Cermak, "Loss-of-coolant accident: past, present, and future," in: Proc. Int. Meeting on Nuclear Power Reactor Safety, Brussels (1978).
3. Projekt Nukleare Sicherheit, Halbjahresbericht 1978/2, KFK-2780, Karlsruhe (1979).
4. P. MacDonald, J. Spore, and J. Broughton, "Results of the first nuclear blowdown tests on single fuel rods (LOC-11 series)," in: Proc. ACRS Reactor Fuel Meeting, USA (1978).
5. Quarterly Technical Progress Report on Water Reactor Safety, TREE-NUREG-1128, Idaho EG and G (1977).
6. L. S. S"botinov and N. I. Kolev, "A study of a nuclear power station containing a VVÉR-440 in an accident involving main circulation loop failure with initial nominal or elevated power levels," Paper at the Comecon Semiar Teplofizika-82 [in Russian], Karlovy Vary (1982).
7. E. Adam, H. Karl, and A. Kirchner, "A study of accident processes on coolant loss from an experimental loop," ibid.
8. I. Mishak, Z. Bazho, and V. Polak, "The effects of first-loop emptying rate in the failure of a cold section in the circulation pipe in a VVÉR-440 on the thermal behavior of the core," ibid..
9. K. Moore and W. Retting, RELAP4: A Computer Program for Transient Thermal-Hydraulic Analysis, ANCR-1127, Idaho EG and G (1973).
10. K. Katsma et al., RELAP4/Mod5: A Computer Program for Transient Thermal-Hydraulic Analysis of Nuclear Reactors and Related Systems, ANCR-NUREG-1335, Idaho EG and G (1976).
11. S. Fischer et al., RELAP4/Mod6: A Computer Program for Transient Thermal-Hydraulic Analysis of Nuclear Reactors and Related Systems, CDAP-TR-003, Idaho EG and G (1978).
12. R. Meyder, SSYST-2, Eingabebeschreibung und Handhabung, KFK-2966, Karlsruhe (1980).

SHOCK LOADS ON UNITS WITHIN THE CONTAINMENT
IN THE VVÉR-1000 IN THE INITIAL STAGE OF AN EMERGENCY
INVOLVING FAILURE IN THE MAIN CIRCULATION PIPELINE

A. I. Boyadzhiev and S. I. Stefanova

UDC 621.039.586

There are many experimental and theoretical studies on the shock loads on equipment within the containment arising from pressure fluctuation at the start during a cooling-loss emergency (CLE) in pressurized-water reactors. The most interesting experimental results have been obtained in the Federal German Republic with the HDR system [1] and in Czechoslovakia [2]. Three-dimensional theoretical studies have been described in [1, 3, 4], and one-dimensional ones in [5-8]. In [1-4], studies have been made on the general aspects of the interaction between the coolant and the equipment when shock loads occur. Estimates have been made [5-7] of the shock loads for the VVÉR-440 on the basis of the BRUKh and TECh' codes. A good survey has been given [9] of computational models in this area.

Here we estimate the shock loads occurring on failure of the main circulation pipe in the VVÉR-1000 by means of the RELAP4/MOD6 program [8]. Figure 1 shows how the circuit is divided into individual volumes. We consider the situation at 0.25 sec after the failure, when there are large pressure fluctuations.

Figure 2 shows the changes in pressure and coolant flow rate in the second volume, while Fig. 3 shows the pressure differences between input to and output from the core and at three points along the height of the thermal shield (ΔP_{12-2}, ΔP_{12-3}, ΔP_{12-4}). The amplitudies of the shock loads vary from 0.6 to 2.8 MPa. It has been found [1, 6, 10] that the calculated pressure pulsation is substantially influenced by the division of the circuit into control volumes and by the time required for the fault to open up. If there are more than 29 such volumes, there is only a minor error in calculating the maximum amplitude. In our case the number of volumes is 35. The time for complete failure was taken as 0.015 sec on the basis of the studies and recommendations of [1, 10].

Figure 4 compares our results on the pressure differences between input and output of the reactor with experimental values obtained on the HDR reactor [1] and with approximate calculations for the VVÉR-1000 [5]. The pulsation frequencies are approximately equal, and an interesting point is that they coincide with the frequency in analogous calculations for the VVÉR-440 [5, 7]. However, the amplitudes differ substantially. The maximum amplitude in the experiment was about 1.1 MPa, while in the RELAP calculations it was 2.8 MPa, or 7.0 MPa in the BRUKh ones. The coolant does not boil within this time interval, so the differences cannot be explained in terms of the vapor, which influences the speed of sound. One of the reasons for the differences in amplitude is evidently that the calculation model is one-dimensional, and it is impossible to incorporate the asymmetry in pressure wave propagation in the ring channel in the outlet part in the reactor. Another is that the computational model assumes inelastic interaction between the coolant and the units within the reactor, whereas in the HDR experiments it was possible for small axial and radial shifts to occur within the reactor pit, which had a damping effect. The differences in the amplitudes given by the BRUKh and RELAP programs (Fig. 4) may be ascribed to the BRUKh calculations being in the nature of estimates, with an inadequate description of the geometry within the containment.

These data on the pressure pulsations at the start of an accident involving pipe failure in a standard VVÉR-1000 can be used as initial data in evaluating the stability of internal units by this method.
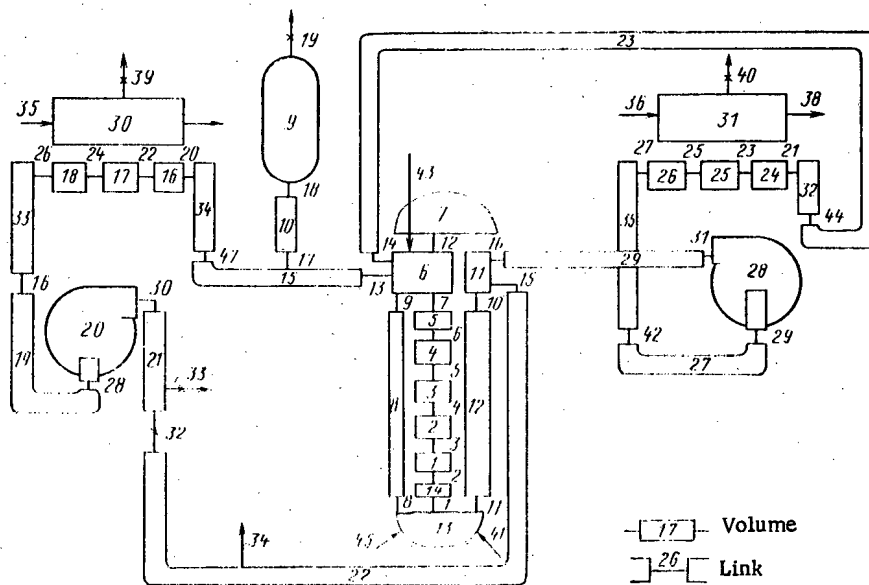
Fig. 1. Scheme for splitting up the first circuit. Volumes:
1-4) core; 5, 14) volume from the end of a fuel-pin sheath
to the end of the fuel pins; 6) upper mixing chamber; 7) in-
tertube space; 8) bypass zone; 9) volume compensator; 10)
link from volume compensator to circuit; 11) reactor inlet;
12) descending part; 13) lower mixing chamber; 15, 23) tube
from reactor outlet to inlet to steam generator; 16, 17, 18,
24, 25, and 26) steam generator on first-circuit side; 19,
27) tube from exit from steam generator to pump; 20, 28)
pump; 21, 22, and 29) tube from pump exit to inlet to reactor;
30, 31) steam generator on second-circuit side; 32, 34) col-
lector at inlet to steam generator; 33, 35) collector at
steam generator exit. Links: 19) safety valve in volume
compensator; 32-34) links for simulating failure; 35, 36)
steam generator feed; 37, 38) output from steam generator;
39, 40) safety valve on steam generator; 41) feed to active
part of emergency cooling system (pumps); 43, 45) feed to
passive part of emergency cooling system (hydraulic accumu-
lators).
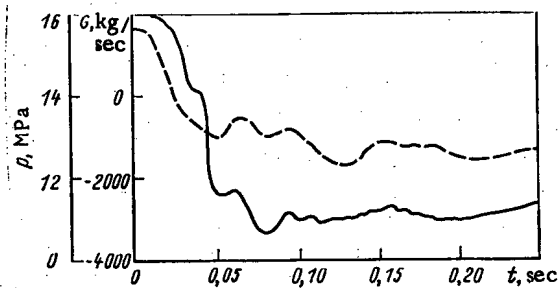
Fig. 2. Pressure (solid line) and
flow rate (dashed line) of coolant
in second volume.

265
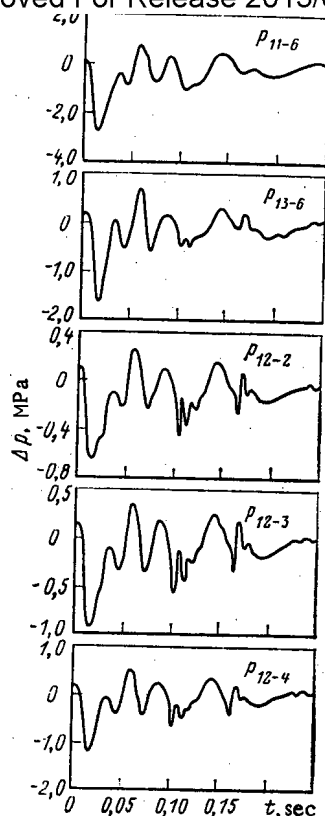
Fig. 3. Pressure dif-
ferences between vari-
ous points in circula-
tion loop.
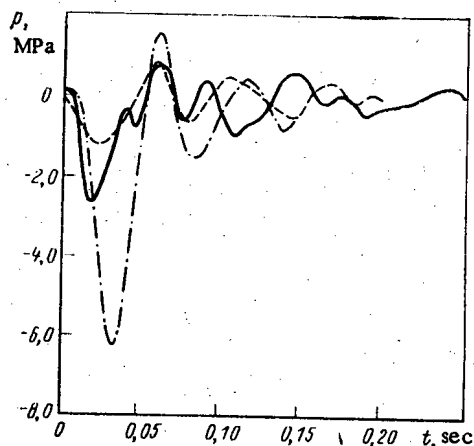
Fig. 4. Comparison of calcula-
tions from the BRUKh–D program
(dash–dot line) and RELAP4 (solid
line) on the pressure difference
between the input and output in
the reactor together with experi-
mental data obtained with the HDR
system (dashed line).

LITERATURE CITED

1. U. Schumann, Nucl. Eng. Design, 73, 303 (1982).
2. Z. Gavelka, M. Sukhanek, and O. Kodim, "An experimental study of the effects of shock waves on a model reactor pit in simulating an accident involving coolant loss," Paper at the Comecon Seminar Teplofizika–82 [in Russian], Karlovy Vary (1982).
3. U. Schumann, Nucl. Eng. Design, 69, 313 (1982).
4. F. Chang et al., ibid., 70, 335 (1972).
5. S. Benedek, "Comparison of calculations from the BRUKh–D and TECh'–12 models on the consequences of failure of a large pipeline in the VVÉR–440 reactor," Paper at the Comecon Seminar Teplofizika–78 [in Russian], Budapest (1978).
6. A. M. Bukrinskii and R. L. Fuks, Teploperedacha, No. 7, 77 (1977).
7. N. Kolev and L. Sabotinov, Kernenergie, 23, No. 6, 230 (1980).
8. S. Fischer et al., RELAP4/MOD6: A Computer Program for Transient Thermal–Hydraulic Analysis of Nuclear Reactors and Related Systems, CDAP TR 003, Idaho EG and G (1978).
9. V. Adamik and A. Tkach, "Computational models for pressure–wave propagation in the first circuit of a VVÉR–440 reactor," Paper at the Comecon Seminar Teplofizika–82 [in Russian], Karlovy Vary (1982).

266

10. A. M. Bukrinskii, Emergency Transients in Nuclear Power Stations Containing VVÉR Reactors
     [in Russian], Énergoizdat, Moscow (1982).

NEUTRON ENERGY SPECTRA IN BFS CRITICAL ASSEMBLIES

V. V. Vozyakov, E. N. Kuzin,
and A. V. Shapar'

A comparison has been made [1] of calculated and observed neutron energy distributions
for some BFS critical assemblies. This continuing study deals with six new compositions
realized with the BFS. Two of them (BFS-24 and BFS-39, Table 1) simulate large power reac-
tors, while the others have been examined in relation to the constant problem. The energy
spectra measured by the time-of-flight method have been corrected for the subcriticality,
the neutron leak into the outgoing channel, the presence of an external source, the flux
anisotropy, and the heterogeneity of the medium (Table 2).

One can derive the overall error in the measured values and the error matrix [2, 3] by
examining the error components in the time-of-flight method (i.e., for $E \leqslant 200$ keV) and in
measurements with proportional counters (E = 1-1200 keV). In the scintillation spectrometer
range (0.8-10 MeV), the error was determined in additional experiments on the well-known
spontaneous fission-neutron spectrum of ^{252}Cf [4]. The errors were estimated for a group de-
composition of the energy scale (Table 3).

The spectra were calculated by means of the programs in the "Spektr" suite, which imple-
ments a numerical method [5] of solving the moderation equation for an infinite homogeneous
medium by means of a specialized nuclear-data library [6]; the effects of neutron diffusion
on the spectrum are incorporated in the harmonic approximation by introducing the material
parameter B^2. The specialized working library has been generated at the Nuclear Data Center
on the basis of cross-section libraries and contains a pointwise representation of the neu-
tron cross sections (total, absorption, radiative capture, fission, and inelastic scattering)
at 14,000 nodes in a nonuniform energy net. The presence of a single net for all isotopes
simplifies the logic in solving for the neutron moderation and saves computer time because
the nuclear data are in a standard format suitable for calculations on any composition. The
number of nodes and the disposition of them are specified from the conditions for minimal
distortion of the resonant-structure description ($\leqslant 0.5\%$) and maximal compression of the nu-
merical data. The library also contains inelastic-transition matrices in the 70-group repre-
sentation, group microconstants derived by the standard BNAB method [7], and other sets of
numbers. The library has been formulated for the range 10 eV to 10 MeV.

Figure 1 compares the calculated and observed neutron energy spectra normalized by
area. The convolution of the calculated spectrum was used, and the detailed distribution
was averaged with the spectrometer resolution-function weights. In the case of the BFS-28
assembly, the measurements at energies below 1 keV have been performed with inadequate sta-
tistics and are not given in the figure, while the time-of-flight measurements for the BFS-24
and BFS-39 are not given because these compositions were examined with a test bed not having
a neutron-beam output to the time-of-flight system.

The structure in the calculated and observed spectra in the main coincide, although
there are some quantitative differences, which is due to inaccuracy in selecting the resolu-
tion parameters in the convolution, incomplete correspondence between the approximating func-
tion and the actual one, and mismatch between the conditions used in deriving the experimental
and calculated data: on the one hand, the errors considered for the experimental methods do
not incorporate the errors in the correction coefficients (Table 2), which may be substantial,
while on the other the methods of zero-dimensional calculation on the detailed spectrum do
not incorporate the smallness of the insert dimensions, the many zones in the assembly, and
so on.
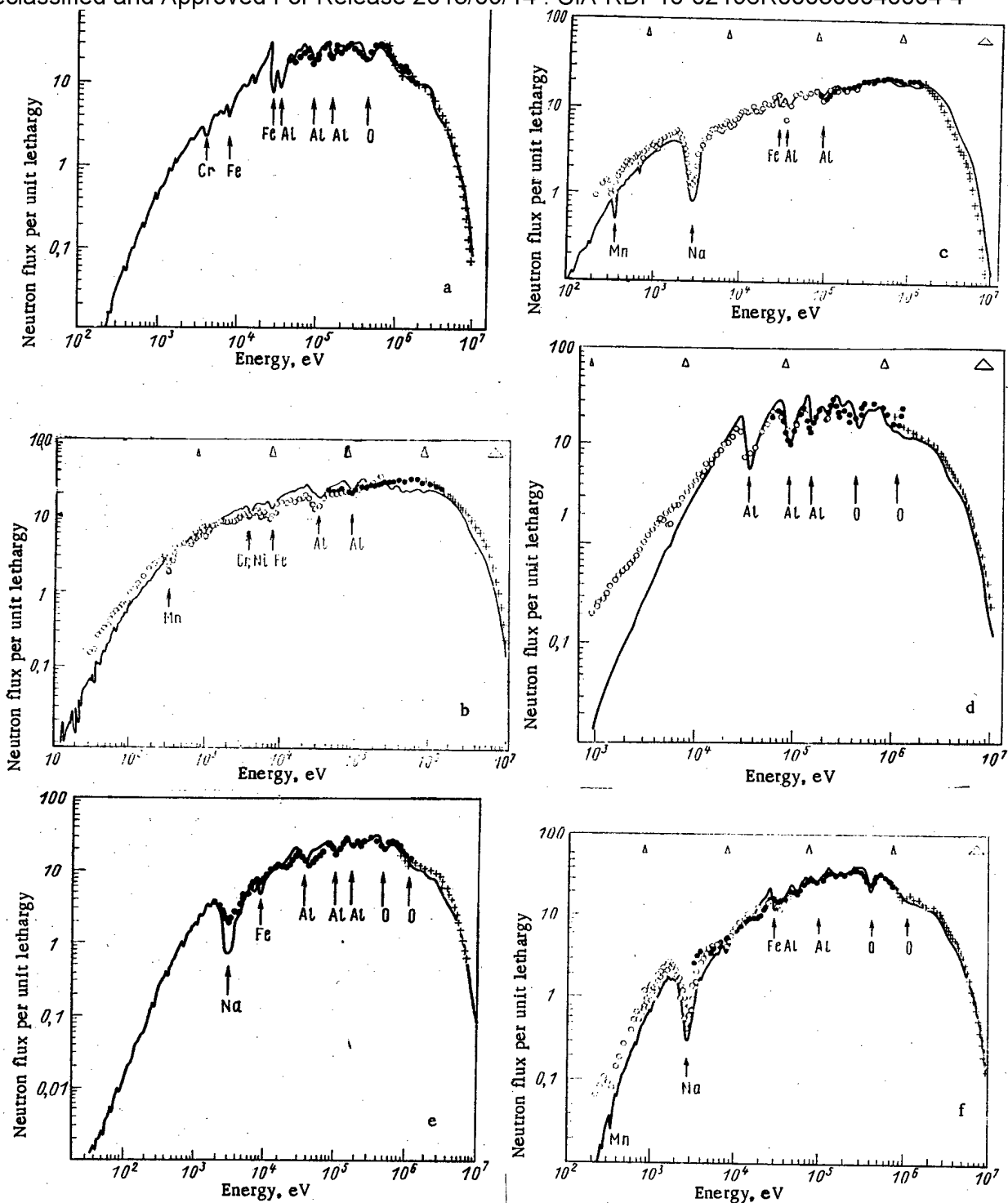
Fig. 1. Neutron spectra in the assemblies BFS-24 (a), 26 (b), 27 (c), 28 (d), 39
(e), and 45 (f): solid line from calculation; o, ●, and +) measurements correspond-
ingly by time of flight, with a hydrogen counter, and with a scintillation spec-
trometer.

The differences between the calculated and observed fluxes obtained by convolution in
the BNAB groups fit approximately within twice the error of experiment for all the critical
assemblies in the energy range 10 keV to 1 MeV. The large discrepancies below 4 keV are
evidently due to the above inadequacy in the derivation of the calculated and experimental
data. The most serious difficulties in comparing the calculations with experiment occur for
the BFS-26 assembly: the curves cross over and the quantitative differences are relatively
large. Incorporating the corrections for the time-of-flight measurements did not eliminate

TABLE 1. Volume Proportions of the Central Zones in the BFS Assemblies, %

Assembly	Fuel	Steel	Alumi-num	Sodium	Carbon	En-rich-ment, %	Central zone vol., liter	Assembly characteristics
BFS-24-16	33	20	25	—	—	21	1550	Model for BN-600 reactor, medium of enriched uranium metal, together with the dioxide of depleted uranium with the addition of Al_2O_3, Al, and Fe
BFS-26	2,9	20	21	—	36	90	700 (16*)	Medium of enriched uranium metal, graphite, iron, and aluminum
BFS-27†	3,8	5	11	29	30	90	565 (12)	Medium of enriched metallic uranium, graphite, sodium
BFS-28	33	—	49	—	—	27	450 (8)	Assembly similar in composition to the zone of high enrichment in the BN-600 (without sodium)
BFS-39	25	21	10	26	—	17	1325	Model for the BN-800 reactor, medium of enriched metallic uranium, dioxide of depleted uranium, sodium, aluminum, and iron
BFS-45	34	13	6	29	—	21	685	Assembly close in composition to zone of low enrichment in the BN-800

*The numbers in parentheses relate to the homogenized part of the insert.
†There were small amounts of Ti and Si in the BFS-27 assembly.

TABLE 2. Corrections for Group Fluxes in the Time-of-Flight Measurement Range

Group No.	Energy range	Correction			
		BFS-26	BFS-27	BFS-28	BFS-29
8—10	0,2 MeV—21.5 keV	1,01	1,01	1,00	1,01
11	21,5—10 keV	1,01	1,01	1,02	1,04
12	10—4,65 keV	1,01	1,01	1,08	1,12
13	4,65—2,15 keV	1,03	1,08	1,22	1,24
14	2,15—1 keV	1,05	1,13	1,43	1,56
15	1—0,465 keV	1,16	1,19	1,81	2,12
16	465—215 eV	1,41	1,46	3,00	3,20
17	215—100 eV	1,51	1,57	—	—
18	100—46,5 eV	2,36	2,50	—	—

TABLE 3. Errors in Measured Neutron Spectrum, %

Energy	Time-of-flight method	Proportional counters	Scintilla-tion spec-trometer
10 eV—0,2 MeV	8—15	—	—
2 keV—1,2 MeV	—	5—25	—
0,8—10 MeV	—	—	10—15

the discrepancies completely, although it reduced them (for example, the discrepancies were reduced by a factor 5–6 for the BFS–45 at energies below about 300 eV). However, the ac-curacy attained in the experiments is inadequate (2–5%) [8]. The error in the calculation method (neglecting the constant component) is estimated as ±5% for the low–energy region, where the fall in the neutron flux relative to the maximum is by not more than 3–4 orders of magnitude.

LITERATURE CITED

1. Yu. A. Kazanskii et al., At. Energ., 52, No. 4, 235 (1982).
2. E. N. Kuzin et al., Preprint FÉI-698, Obninsk (1976).
3. V. F. Efimenko, Preprint FÉI-697, Obninsk (1976).

4. V. M. Lityaev, V. A. Dulin, and Yu. A. Kazanskii, At. Energ., 47, No. 1, 44 (1979).
5. M. F. Vorotyntsev et al., Preprint FÉI-1006, FÉI-1007, Obninsk (1980).
6. V. V. Vozyakov et al., Nuclear Science and Engineering: Nuclear Constants Series [in Russian], Issue 27 (1977), p. 16.
7. L. P. Abagyan et al., Group Constants for Calculating Nuclear Reactors [in Russian], Atomizdat, Moscow (1964).
8. Yu. Kazansky, A. Vankov, and E. Inyutin, At. Energy Rev., 13, No. 4, 807 (1975).

MEASUREMENT OF THE THICKNESS OF THE DEPOSITS

OF NUCLEAR FUEL

P. S. Otstavnov and V. P. Koroleva   UDC 621.039.58

Nuclear fuel, entering into the first loop of a reactor from unsealed fuel elements, accumulates together with other elements in the coolant and in deposits on the inner surfaces of the loop. The main radiation danger of the nuclear fuel is from α radiation. If plutonium is used as the fuel, then the danger of contact with the fuel increases due to its very high toxicity. Information on the content of fuel in the coolant, in the walls of the loop and in the equipment is required in order to evaluate the radiation environment, especially during maintenance operations.

The possibility of using solid track detectors for detecting α activity of the fuel in the first loop of a fast reactor was studied in [1, 2] and the structure and nature of its deposits were also investigated. The measurements of the contamination of the surfaces of pipes by the fuel provided information on the content of fuel only in the surfaces and near-surface layers due to the small mean free path of α particles in the material of the deposits. To determine the fuel content of the deposits, it is necessary to know the depths of penetration of radioactive materials into the deposited layer and the degree of uniformity of their distribution in it, which is obtained by measuring the thickness of the radioactive deposits. To determine the thickness of radioactive deposits, the method of layer-by-layer removal of the surface of the specimen under study by a mechanical or a chemical method, combined with subsequent measurement of the radioactivity of the layers which were removed or which remain, is usually used.

The purpose of this work was to use the method of solid track detectors to determine the thickness of the deposits of nuclear fuel on the inner surface of samples cut out of the pipe in the bypass line of a sodium-cooled reactor.

The experiment basically involved projecting the transverse section of the layer of deposits (thickness of the layer) with the help of α particles from the fuel, contained in the deposits, onto the track detector: nitrocellulose in direct contact with the layer. This method is direct and reliable, and since it does not involve the destruction of the radioactive layer, it permits performing repeated measurements with the same sample.

We attached the detector consisting of the nitrocellulose with a thickness of 0.12 mm from RF-3 photographic film on the lateral surface of a section of the metallic sample of the pipe. We first worked the lateral surfaces of the samples mechanically in order to remove jags, scoring, and other forms of surface irregularities, remaining after the sample was cut out of the pipe. This operation is necessary in order to ensure a close contact between the detector and the sample and in order to obtain a high-quality profile of the deposits.

To eliminate the effect of tracks from α particles from the active layer which is not in direct contact with the nitrocellulose, we covered the inner surface with a closely fitting screen made of aluminum foil, which absorbed all the α particles leaving at an angle to the solid track detector from the inner surface of the pipe sample. In order to irradiate several nitrocellulose detectors simultaneously from samples with the deposits, we constructed a ring-shaped holder whose outer diameter corresponded to the inner diameter of the pipe.

To determine the thickness of the radioactive layer, we placed the nitrocellulose detectors, which were closely clamped with a load, in the endface surface of the ring-holder and the lateral surface of the section of the samples with the layer. In this case, the ring-holder also functioned as an aluminum screen.

The exposure was performed for a period of 3-5 days. After etching in an alkali solution, flushing in distilled water, and drying, we examined the detectors in a PMT-3 microscope with a magnification of 360. We determined the thickness of the layer from the width of the line of intense α radiation recorded by the detector. The density of the tracks formed by the α particles from the layer under study in the nitrocellulose exceeded the density in neighboring background sections by tens and hundreds of times. We determined the width of the line visually with the help of a scale on the eye piece of the microscope. The scale value permitted determining the dimensions to within ±2 μm. The fine matted strip from the layer of radioactive deposits could also be observed against the background of the transparent nitrocellulose with the naked eye. It repeated the form of the inner surface of the metallic sample itself. The thickness of the layer of deposits was ∿100 μm. The maximum spread of the thickness of the layer, obtained on the nitrocellulose in contact with the radioactive layer, was 10 μm.

To determine the density distribution of the α-active material in the layer, we measured the density distribution of the tracks of α particles over the thickness of the layer. In most cases, the density of tracks over the thickness of the layer is constant within a single section, but varies somewhat from section to section, even for the same sample. The investigations established that solid track detectors can be used successfully to measure the thickness of deposits of the α-active substance to study the distribution of its concentration over the thickness of the layer.

<div align="center">LITERATURE CITED</div>

1. V. P. Koroleva, P. S. Otstavnov, and V. S. Shereshkov, At. Energ., 46, No. 2, 125 (1979).
2. V. P. Koroleva and P. S. Otstavnov, ibid., 50, No. 2, 145 (1981).
3. V. A. Kuznetsov et al., ibid, 32, No. 6, 481 (1972).

RADIATION-STIMULATED DIFFUSION OF AEROSOLS

I. E. Nakhutin, P. P. Poluéktov,
and G. Yu. Kolomeitsev

Diffusion plays an important role in the behavior of aerosol systems, for example in filtration, deposition of aerosols on different surfaces, as well as in coagulation processes [1]. Diffusion of particles arises as a result of their Brownian motion, where the source of the Brownian impacts is the thermal motion of the gas molecules. In radioactive gases there is one other factor responsible for the random wandering of aerosols. Radioactive decay events are accompanied by ionization of the gas; as a result of the fission of ions of different signs, very strong local electric fields appear, whose characteristic spatial dimensions, as a rule, exceed the dimensions of the particles. The local fields have a twofold effect on the particles; first, due to the charging of aerosols in radioactive gases, coulomb forces act on the particles and, second, neutral particles are entrained into nonuniform fields.

The purpose of this work is to calculate the coefficient of diffusion of particles in radioactive gases taking into account the processes mentioned above. We note that there is one more source of random wanderings: recoil, which accompanies emission from particles, but is insignificant compared to the effects under examination.

To derive the coefficient of diffusion, we shall use the method for obtaining the Fokker-Planck equation described in [2]. The equation of motion for a Brownian particle, represented in the form of a sphere with radius R and mass m, moving in a gas with velocity v,

271

in the limit of small Reynolds numbers $(\text{Re} = vR/v \ll 1)$, has the form $\gamma_v = y(t)$, where $\gamma = 6\pi R\eta$ and η is the dynamic viscosity of the gas. The random force $y(t)$ represents a sum of three terms: the Langevin force y_m, which arises from the thermodynamic fluctuations in the gas; the force qE acting on a charge q in an electric field E; the ponderomotive force $\frac{\alpha V}{4\pi}(E\nabla)E$, which acts on neutral particles in an inhomogeneous field (V is the volume of the particle, αV is its polarizability). It is assumed that the characteristic length over which the random electric field varies exceeds the dimensions of the particles.

Thus, we have three random functions of time y_m, q, E, which are independent of one another. The derivation of the equation of diffusion is based on the hierarchy of times in the problem. It is assumed that the correlation time of the Langevin source is small [2] compared to the the characteristic Stokes relaxation time $\tau_p \sim (\gamma/m)^{-1} \sim \rho_0 R^2/9\eta$ ($m = \frac{4}{3}\pi R^3 \rho_0$ is the mass of the particle; ρ_0 is the density of the particle material). The use of the equation of motion of a particle in the form presented above presumes that the process is examined with a time ($t - t_0$) greatly exceeding τ_p. Let us compare τ_p to the characteristic time τ_e of variation of the random electric field, which coincides with the recombination time of the plasma in the region of radiation damage, estimated as $\tau_e = (\beta n)^{-1}$ (here n is the number of electron-ion pairs in the radiation decay channel; β is the coefficient of recombination). Thus there exists a size R^* of aerosol particles for which $\tau_p = \tau_e$, equal to $R^* = \sqrt{9\eta/\beta n \rho_0}$. In air under normal conditions, we obtain $R^* \approx 10^{-2}$–10^{-3} cm. Since the sizes of typical aerosols, suspended in an air atmosphere, are less than 10 µm, we can assume that $\tau_p \ll \tau_e$. This means that the changes in the particle velocities follow the changes in the field, in accordance with the equation of motion. Restricting our analysis to processes averaged over times longer than τ_e, we can assume that the random electric field is δ-correlated; its average value equals 0, while $<E_i(t)E_k(t')> = B\delta_{ik}\delta(t - t')$ (the structure of the constant B is examined below).

Thus there are two "slow" processes: charging of aerosols and their diffusion in space. The first process has been studied in many papers [3–10], where it is established that the characteristic time for charging a particle is independent of the dimensions of the system. On the other hand, the characteristic time for diffusion increases as the square of the dimensions of the system, and for large dimensions greatly exceeds the charging time. Therefore, spatial diffusion can be examined assuming a stationary distribution of charge over particles (of a given size), although the charge of each particle varies.

Under the assumptions made above, the procedure for obtaining the coefficient of diffusion is the same as the one described in [2]. In [2], the coefficient of diffusion of particles is determined by averaging the square of the velocity over time: $<v_i v_k> = 2D\delta_{ij}\delta(t - t')$. In our case D has the form

$$D = D_T + \frac{\tau_k}{6\gamma^2}\left\{\bar{q}^2\langle E^2\rangle + \left(\frac{\alpha V}{4\pi}\right)^2 \langle [(E\nabla)E]_i^2\rangle\right\}, \tag{1}$$

where $D_T = kT/\gamma$ is the coefficient of thermal diffusion of particles; k is Boltzmann's constant; T is the temperature; $\bar{q}^2$ is the average (for a given R) charge; τ_k is the correlation time of the electric field (it coincides with the characteristic lifetime of the region of radiation damage τ_e). The braces correspond to averaging over time at some point or (with a stationary random process) averaging over space. For $A V_h \tau_h \ll 1$ (V_h is the volume of the region of damage arising with a single decay; A is the specific activity of the gas), when the regions of radiation damage do not overlap, we have

$$\langle E^2\rangle = A V_h \tau_h \langle E^2\rangle_0; \tag{2}$$

$$\langle [(E\nabla)E]^2\rangle = A V_h \tau_h \langle [(E\nabla)E]^2\rangle_0, \tag{3}$$

where the zeroth index indicates averaging over separate channels of the damage.

Based on the above, the coefficient of radiation-stimulated diffusion of aerosols is expressed by the formula*

$$D = \frac{kT}{\gamma} + \frac{A V_h \tau_k}{6\gamma}\left\{\bar{q}^2\langle E^2\rangle_0 + \left(\frac{\alpha V}{4\pi}\right)^2 \langle [(E\nabla)E]^2\rangle_0\right\}. \tag{4}$$

---

*We emphasize that the use of formula (4) is restricted to the case of low activity in accordance with the inequality $A V_h \tau_h \ll 1$ and the formula is accurate to this order.

We note the linear growth of the coefficients of diffusion with increasing activity, if we restrict our attention to the case of nonoverlapping fields of radiation damage, as well as to the assumption that $\overline{q}^2$ does not depend on the activity (both of these assumptions restrict the upper limits of the activity). We shall determine the activity for which the terms related to the thermal and radiation wandering in the coefficients of diffusion are equal.

The value of the coefficient of diffusion according to the formula is primarily determined by the average values of some functions of the electric field in the region of radiation damage. According to the data in [11], for the 1-MeV β-electron channel in air, we may take $E \approx 10$ V/cm, $\tau_k \approx 0.1$ sec, $V_k \approx 0.2$ cm^3.

Let the diameter of a particle be ~ 10 μm and its density $\rho \approx 1$ g/cm^3. In air, for these particles, $\gamma \approx 1.5 \cdot 10^{-6}$ g/sec, $D_T \approx 2.5 \cdot 10^{-8}$ cm^2/sec. We shall assume the diffusion mechanism for charging of particles; from the relation $qe/R \approx kT$ (the energy required for an electron to reach the surface of the particle is close to the thermal energy), we estimate $q \approx 100e$ (e is the charge of an electron). Then, according to the formula, with an activity of $A \approx 10^{-5}$–10^{-6} Ci/liter* the contribution of radiation electric fields to diffusion becomes determining compared to the thermal diffusion.

Thus the velocity of diffusion of aerosols increases markedly with a comparatively low level of activity. As a result, the deposition of aerosols in pipes and aerosol-removing equipment can accelerate. This process should be especially clearly manifested in operating with air-cleaning systems under emergency conditions at nuclear power plants (see [12]). It is evident that the rate of diffusion increases not only in the presence of the intrinsic radioactivity of the gas, but also under the conditions of irradiation by external radiation. We note that the model presented for radiation-stimulated diffusion is applicable to both gases and liquids. The present description can be extended, aside from aerosols, to the diffusion of molecules.

LITERATURE CITED

1. N. A. Fuks, Mechanics of Aerosols [in Russian], Izd. Akad. Nauk SSSR, Moscow (1955).
2. Yu. L. Klimontovich, Statistical Physics [in Russian], Nauka, Moscow (1982).
3. V. D. Ivanov, V. N. Kirichenko, and I. V. Petryanov, Dokl. Akad. Nauk SSSR, 182, No. 2, 307 (1968).
4. V. D. Ivanov and V. N. Kirichenko, ibid., 188, No. 1, 65 (1969).
5. V. N. Kirichenko and V. D. Ivanov, ibid., 188, No. 2, 315 (1969).
6. V. N. Kirichenko, V. M. Berezhnoi, and B. V. Shan'gin, ibid., 205, No. 1, 78 (1972).
7. V. D. Ivanov et al., ibid., 203, No. 4, 806 (1972).
8. V. N. Kirichenko and N. N. Suprun, ibid., 215, No. 2, 325 (1974).
9. L. Reed, H. Jordan, and J. Cieseke, J. Aerosol Sci., 8, 457 (1977).
10. V. V. Gromov, Electric Charge in Irradiated Materials [in Russian], Énergoizdat, Moscow (1982).
11. Tables of Physical Quantities [in Russian], Atomizdat, Moscow (1976).
12. G. Yu. Kolomeitsev, I. E. Nakhutin, and P. P. Poluéktov, At. Energ., 55, No. 3, 183 (1983).

---

*This corresponds to a specific activity of $3.7 \cdot 10^8$–$3.7 \cdot 10^7$ Bq/m^3.

POSSIBILITIES OF USING NEUTRONS OF THE COSMIC
BACKGROUND FOR THE INVESTIGATION OF THE SALT CONTENT
OF SEAWATER

E. M. Filippov
UDC 550.35:551.46.083

Nuclear reactions leading to the formation of neutrons arise under the action of the solar wind on atomic nuclei of the atmosphere. As the altitude decreases, the neutron flux of cosmic origin declines according to an exponential law [1]. Due to reflection of neutrons from the land and water surfaces as well as their origin in rocks and water under the action of mesons and so on, this flux increases. It has been shown that the near-surface component of cosmic neutrons can be used to study neutron-absorbing useful minerals (boron and tungsten) which outcrop at the surface or are exposed by open-pit mining [2-4].

The possibility of using the neutrons of cosmic background to study seawater is considered in this paper. The use of neutrons of an external source for these purposes has been described in [5] and in more detail — [6]. In order to estimate the albedo α of neutrons isotropically incident on the surface being irradiated, people use various relationships:

$$\alpha = 1 - 2.31\,(\Sigma_c/\Sigma)^{1/2},\tag{1}$$

where Σ_a and Σ are the macroscopic absorption cross sections of neutrons in the medium being investigated and the total cross section, respectively [7], or

$$\alpha = (1 - \beta)/(1 + \beta),\tag{2}$$

where $\beta = \frac{2}{3}\lambda_t L$, λ_t is the transport migration length of thermal neutrons, and L is the diffusion length of thermal neutrons [6, 8].

For an isotropic flux of fast neutrons the albedo of thermal neutrons is calculated from the formula [8]

$$\alpha = \frac{\tau L v}{(L_s + L)\,(\tau v + 2L)},\tag{3}$$

where τ and v are the mean lifetime and velocity of thermal neutrons and L_s is the thermalization length of fast neutrons in the medium being studied [8]. For neutrons of a californium source $L_s = 5.24$ cm [5]. The diffusion parameters for thermal neutrons (macroscopic cross sections with respect to capture Σ_a and scattering Σ_s of neutrons and the mean free paths of neutrons λ_a, λ_s, λ corresponding to them, the diffusion coefficient D, etc.) depend on the salinity of the water (Table 1) and its temperature (Table 2). The results of calculations of the values of α (Fig. 1) indicate that an increase in the salinity of the water will lead to a decrease in the albedo of thermal neutrons.

The distribution of the flux density of thermal neutrons near the water surface and in water of different salinities is shown in Fig. 2. The curves given are constructed from the data of [1, 9], and the neutron fluxes of cosmic origin in water of different salinities are calculated by the author. It follows from Fig. 2 that the neutron component in the atmosphere near the water surface can be represented as the sum of two exponential functions shown as dashed lines. The higher the salinity of the seawater, the more rapidly does the neutron component of the cosmic background decrease with depth. It follows from this that by lowering neutron detectors into seawater and measuring the neutron radiation of cosmic origin one can assess the variation of the salinity of seawater. It is best for these purposes to use highly efficient proportional counters filled with ^{3}He. Cassettes with a neutron recording efficiency of $\sim$50% [10] can be assembled on their basis. One can determine the salinity of seawater with an error of $\sim$1% by the immersion of such cassettes of detectors with an area of 10^4 cm^2 (1 m^2) to a depth of 40–80 cm.

TABLE 1. Diffusion Parameters for Thermal Neutrons in Water of Various Salinities

Neutron parameters	Fresh water (zero salinity)	Black Sea water (salinity of 17.5 g/kg)	Ocean water (salinity of 35 g/kg)
Σ_a, cm²/g	0,0221	0,02736	0,03239
Σ_s, cm²/g	3,716	3,689	3,662
Σ, cm²/g	3,738	3,716	3,694
λ_a, cm	45,25	36,19	30,06
λ_s, cm	0,269	0,268	0,266
λ, cm	0,268	0,2625	0,264
λ_t, cm	0,431	0,429	0,426
τ, sec	$2,06 \cdot 10^{-4}$	$1,65 \cdot 10^{-4}$	$1,365 \cdot 10^{-4}$
L, cm	2,77	2,42	2,20
D, cm²/sec	$3,97 \cdot 10^4$	$3,55 \cdot 10^4$	$3,54 \cdot 10^4$

TABLE 2. Effect of the Temperature of Ocean Water on the Velocity and Diffusion Length of Thermal Neutrons

t, °C	ρ, g/cm³	L, cm	v, cm/sec
20	1,024806	2,19	$2,191 \cdot 10^5$
22	1,024265	2,20	$2,1985 \cdot 10^5$
25	1,023383	2,21	$2,2096 \cdot 10^5$
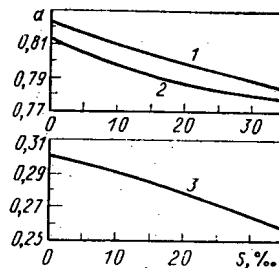
Fig. 1. The effect of salinity of water on the neutron albedo: 1, 2, 3) results of calculations according to formulas (1), (2), and (3), respectively.

Devices with neutron detectors on ships and helicopters can be used to determine the salinity of seawater by recording the neutrons of cosmic origin reflected by the water surface. To get a quantitative estimate of the possibilities of this method, we shall represent the total flux density Φ of cosmic neutrons in the atmosphere as the sum of two exponential functions:

$$\Phi(H) = \Phi_1 + \Phi_2 = \Phi_{10} e^{-H/L} + \Phi_{20} e^{b/H}. \tag{4}$$

Here L is the diffusion length of thermal neutrons in the atmosphere, b is a constant, and Φ_{10} and Φ_{20} are coefficients determined from the graphs of Fig. 3 for Φ_1 and Φ_2 at H = 0 and are equal to $1.76 \cdot 10^{-3}$ and $2.4 \cdot 10^{-4}$ neutrons/(cm²·sec), respectively. The flux density of the neutrons reflected by a flat water surface is described by the diffusion equation

$$\Phi_f = \frac{q}{2\Sigma_a L} e^{-H/L}, \tag{5}$$

Fig. 2. Distribution of the flux
density of thermal neutrons near the
water surface and in water of differ-
ent salinities for the geomagnetic
latitude 44°.
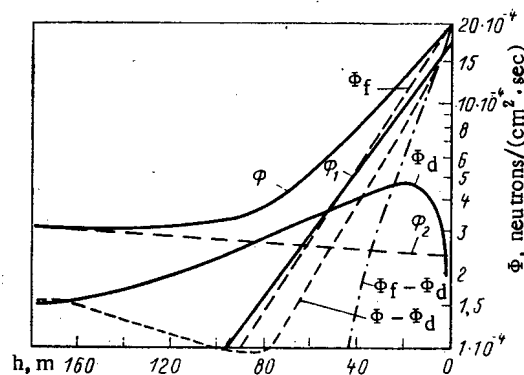
Fig. 3. Dependence of the flux
density of neutrons on altitude:
Φ) total flux density, and its com-
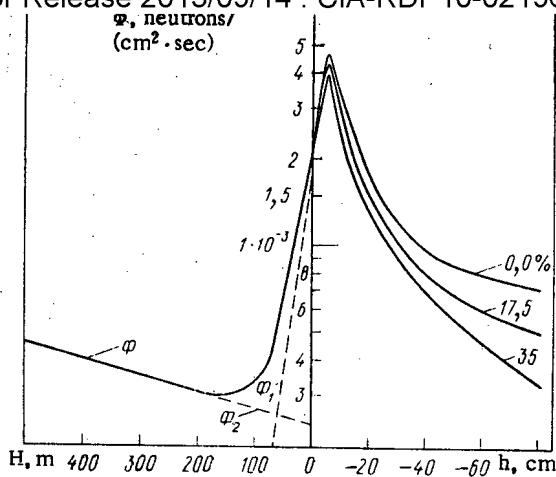ponents are Φ_1 and Φ_2; Φ_f) flux
density of neutrons reflected by a
flat water surface, Φ_d) diffusion
flux of neutrons, and $\Phi - \Phi_d$ and
$\Phi_f - \Phi_d$) difference fluxes.

where q is the flux density of neutrons at the water surface [for the case under discussion
$q = 10^{-3}$ neutrons/(cm$^2\cdot$sec)] and Σ_a is the macroscopic absorption cross section of thermal
neutrons in the atmosphere; the function Φ_f is given in Fig. 3.

In order to suppress the neutron fluxes from the upper half-space and to record those
from the lower half-space, the cassettes of detectors mentioned above should be shielded from
above by a layer of cadmium 1 mm thick [1]. In addition to the flux Φ_f neutrons diffusing
from the lower half-space will exert an effect on a detector located at the point D at an
altitude h above the water surface (Fig. 4). Both the component Φ_f and the component of the
neutron flux emerging from the upper half-space, Φ_2, are sources of them. The flux density
of neutrons produced by diffusion in the lower half-space and incident on the detector can
be determined by calculating the following integral:

$$\Phi_d = \int_v \Phi(H) F(r) \, dv. \tag{6}$$

The function F(r) is the diffusion equation of thermal neutrons of a point source lo-
cated in a space with the coordinates (H, y), and it is determined by the relationship [8]:

276

Fig. 4. Scheme for calculation of the neutron fluxes above a water surface.
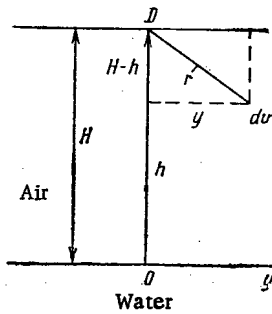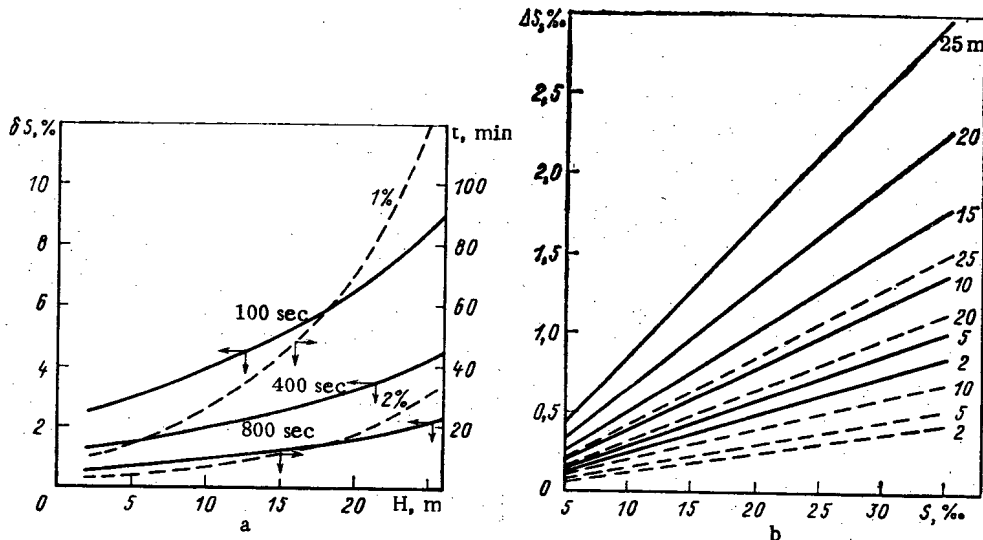

Fig. 5. Errors in measuring the salinity of water: a) absolute errors for different altitudes with a measurement duration of 100 (———) and 400 sec (—————); b) relative errors for various measurement duration.

$$F(r) = \frac{1}{4\pi L^2} \frac{e^{-r/L}}{r} \text{ (neutrons/cm}^3\text{).}$$ (7)

Calculating the integral (6) in the cylindrical coordinate system, we obtain

$$\Phi_d = \frac{1}{2} \left\{ \Phi_{10} \frac{H}{L} e^{-H/L} + \frac{\Phi_{20}}{1+bL} (e^{bH} - e^{-H/L}) \right\}.$$ (8)

The first term is determined by measurements of the fluxes of neutrons from the lower half-space at an altitude no greater than 100 m. For H > 100 m the expression (8) reduces to the form

$$\Phi'_d = \frac{\Phi_{10}}{2(1+bL)} (e^{bH} - e^{-H/L}).$$ (9)

For H > 200 m one can also neglect the second term in this expression:

$$\Phi''_d = \frac{\Phi_{10}}{2(1+bL)} e^{bH}.$$ (10)

For calculations using the relationships (8)-(10) it is necessary to estimate the parameters for the diffusion of thermal neutrons in the atmosphere. To this end, we shall adopt the following composition of air: nitrogen — 78%, oxygen — 21.5%, and hydrogen — 0.5%; density of nuclei of the indicated elements: $p_N = 4.19202 \cdot 10^{19}$, $p_O = 1.5549 \cdot 10^{19}$, and $p_H = 2.6872 \cdot 10^{17}$ [11]. Finally, the diffusion parameters of thermal neutrons in air will take the following values: $\Sigma_a = 7.89 \cdot 10^{-5}$ cm^{-1}, $\Sigma_s = 4.947 \cdot 10^{-4}$ cm^{-1}, $\Sigma = 5.736 \cdot 10^{-4}$ cm^{-1}, $\tau = 0.0576$ sec, L = 2920 cm, D = $1.482 \cdot 10^8$ cm^2/sec, and b = $1.24225 \cdot 10^{-5}$ cm^{-1}.

277

The values of Φ_d calculated using formulas (8)–(10) are shown in Fig. 3. It is evident that at H = 0 the function Φ_d = 0 and reaches a maximum at H ≈ 20 m, then gradually decreases to an altitude of H ≈ 165 m, and then gradually increases again. The function $\Phi - \Phi_d$, which describes the flux of neutrons incident on the detector from the upper half-space, and the neutron flux $\Phi_\alpha = \Phi_f - \Phi_d$, which conveys direct information about the salinity of seawater, are also shown in Fig. 3. It follows from a comparison of the plots of Φ_α and Φ_d that the first of these components prevails at H ⩽ 23 m.

Let us proceed to a calculation of the errors in the determination of the salinity of seawater from the results of measurements of the neutron flux densities at altitudes of 2–25 m, having taken the effective area of the detecting system εs to be equal to 10^4 cm² (the area s = 2 m², and the efficiency ε = 50%). The counting rate is related to the neutron flux density by the relationship

$$N_\alpha = \varepsilon s \Phi_\alpha. \tag{11}$$

We find the absolute error of determining the useful counting rate from the equation

$$\Delta N_\alpha = \sqrt{N_\alpha + 2N_d}, \tag{12}$$

whence the absolute error in determining the salinity of seawater is

$$\Delta S = S\delta S = S\delta N_\alpha = S\frac{\Delta N_\alpha}{N_\alpha}, \tag{13}$$

where δS and δN_α are the relative errors of determining the salinity and the counting rate, respectively, which are taken to be equal [6].

The numerical values obtained for the measurement errors are shown in Fig. 5. The absolute errors of determining the salinity of water at various altitudes with measurement durations of 100 and 400 sec can be estimated from the data of Fig. 5a. It follows from Fig. 5b that when the detecting system is located at an altitude of 2 m above the water surface it is necessary for determination of the salinity with an error of ∼1% to measure the counting rate for ∼400 sec; at H = 25 m the measurement duration should be increased to 120 min.

In the future helicopters may be replaced by aircraft of the small-dirigible type, to the creation of which a lot of attention is being devoted at the present time, for obtaining information about the salinity of water with the help of neutron detectors. If one fills the gondola of such a dirigible completely or partially with ³He, i.e., converts it into a detecting system of large volume, the measurement duration can be significantly reduced.

We have assumed in the calculations performed that the neutron fluxes are constant. Their actual fluctuations can be taken into account with the help of special monitors which measure the ratios of the counting rates of neutrons from the lower and upper half-spaces.

LITERATURE CITED

1. G. V. Gorshkov et al., The Natural Neutron Background of the Atmosphere and the Crust of the Earth [in Russian], Atomizdat, Moscow (1966).
2. V. M. Bondarenko and B. N. Kul'kov, "The natural neutron background at the earth–air boundary," VINITI, No. 1626–79 Dep., Moscow (1979).
3. V. M. Bondarenko, and B. N. Kul'kov, "The first results of the testing of the albedo method for neutrons of cosmic radiation at boron deposits," VINITI, No. 2003–79 Dep., Moscow (1979).
4. V. M. Bondarenko and B. N. Kul'kov, "The first results of the application of the albedo method of cosmic neutrons at the Tyrnauz deposit," VINITI, No. 2004–79 Dep., Moscow (1979).
5. E. M. Filippov, At. Energ., 47, No. 4, 263 (1979).
6. E. M. Filippov, "Neutron methods for the study of seawater," VINITI, No. 3180–83 Dep., Moscow (1983).
7. T. A. Germagenova et al., The Albedo of Neutrons [in Russian], Atomizdat, Moscow (1973).
8. E. M. Filippov, Nuclear Geophysics [in Russian], Vols. 1, 2, Nauka, Novosibirsk (1973).
9. G. V. Gorshkov and O. S. Tsvetkov, in: Methods for the Determination of Radioactivity (Symposium Materials) [in Russian], Naukova Dumka, Kiev (1978), p. 14.
10. V. A. Zyabkin and R. M. Yakovlev, Preprint RI–89 of the V. G. Khlopin Radium Institute [in Russian], Leningrad (1978).
11. Yu. A. Medvedev, B. M. Stepanov, and G. Ya. Trukhanov, Nuclear Physics Constants of the Interaction of Neutrons with Elements Which Make Up the Atmosphere and Crust of the Earth [in Russian], Énergoizdat, Moscow (1981).

278

COMBINED SHIELDING FOR MONOCHROMATORS OF CRYSTAL-DIFFRACTION

INSTRUMENTS

E. A. Garusov, I. V. Golosovskii,   UDC 539.1.074:621.039.7
N. K. Pleshanov, V. A. Trunov,
A. K. Tsytsenko, and V. B. Shchebetova

Monoenergetic thermal neutrons are obtained most simply by diffraction on a crystal-monochromator. In operation at wavelengths $\lambda > 0.5$ Å (1 Å = 10^{-10} m) the relative width of the spectral line usually amounts to several per cent of λ. Since the remainder of the incident spectrum should be effectively absorbed, in any diffraction apparatus shielding of the crystal-monochromator is one of the main subassemblies which accounts for a considerable part of the cost of the entire apparatus. A possible way of cutting these costs is that of using several crystal-monochromators, ensuring the simultaneous operation of a number of apparatuses, and optimizing their shielding. In nuclear power plants, in which the shielding cost C_S amounts to 20-30% of the total cost of the plant [1], the principle for optimizing C_S is to minimize it with the condition that the radiation dose be limited to a value below the allowable dose [2]. In addition to minimum cost and observance of radiation safety standards, the shielding of crystal-monochromators should also ensure the maximum neutron flux of the prescribed spectral composition and a certain divergence at the crystal-monochromator. Consequently, the geometric beam-attenuation factor K_g, determined by the total thickness of the absorbing material, should be minimum. Moreover, as a rule, stringent requirements are set as to the overall dimensions of the shielding, owing to the limited area for installing equipment in the experimental hall of the reactor. It thus follows that it is necessary to minimize the quantity*

$$C_s K_g / K = \min,$$

where K is the overall attenuation factor and C_S and K_g are defined as above. Thus, attenuation of the scattered beam in the crystal-monochromator must be ensured primarily by the optimum choice of absorbing materials and not the thickness of the shielding.

In designing the shielding for the crystal-monochromators of diffraction apparatuses set up on the neutron beams of the VVR-M water-cooled water-moderated reactor at the B. P. Konstantinov Institute of Nuclear Physics, Academy of Sciences of the USSR, Leningrad, it was necessary to meet the following requirements: build it as a demountable unit in case operational disassembly is necessary, ensure the simultaneous operation of three crystal-monochromator apparatuses (multiple-counter diffractometer for the investigation of poly-crystals, a four-circle diffractometer, and an apparatus with polarized neutrons for solving nuclear physics problems), make provisions for continuous variation of the wavelength of neutrons reflected by the monochromator-polarizer. The need to conduct polarization through the shielding imposes additional conditions on the design of the exit channel.

Most often the shielding of a crystal-monochromator is made in the form of a cylinder, inside which is a crystal with a channel through it for the reflected beam. To vary the wavelength the entire unit (weighing several tons) is rotated about the vertical axis. Either a complex system of moving wedges is used to provide the shielding at the beam exit or the beam is extracted through a wide sector. In this case an extra stationary shield between the cylinder and the reactor is required.

The proposed shielding design was solved as follows (Figs. 1, 2). The multiple-counter and four-circle diffractometers use beams of fixed-wavelength neutrons reflected from two families of crystallographic planes of one crystal, (331) and (111), respectively. The scattering angles of the diffracted beams (76° and 32°) are prescribed by the particular layout

---

*This functional does not take account of savings made on the fuel costs and operating costs of the reactor, which would require simultaneous optimization of the shieldings for all equipment operating on the reactor.
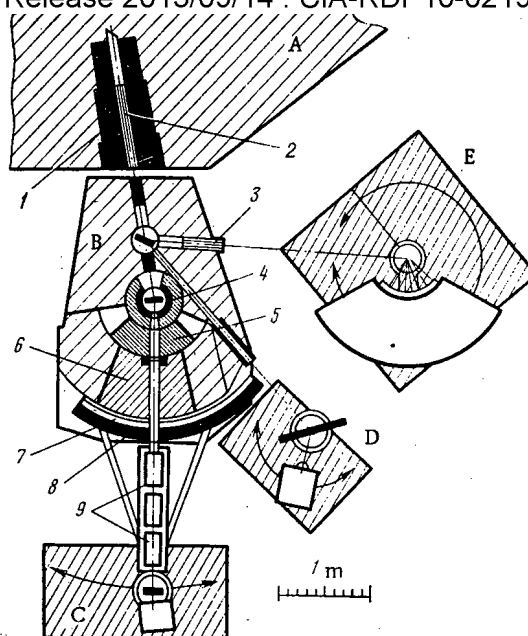
Fig. 1. Design of shielding and lay-
out of physical equipment: A) reac-
tor radiation shielding; B) shield-
ing of crystal-monochromators; C) ap-
paratus with variable wavelength for
nuclear physics research; D) four-
circle diffractometer for research on
single crystals; E) multiple-counter
diffractometer for research on poly-
crystals; 1, 3) multiple-slit colli-
mators; 2) reactor-beam gate; 4)
cast iron; 5) iron-paraffin mix-
ture; 6) hydrogen-containing shield-
ing; 7) nickel layer; 8) lead layer;
9) girder with experimental equipment.

of the physical equipment and the angle between the crystallographic planes. Moreover, in choosing the diffraction angles we took into account their relation to the resolution of the instruments and other physical factors (in particular, the necessity to discriminate from higher orders in the diffracted beam). The apparatus with polarized neutrons with a variable wavelength (possible diffraction angles of up to 30°) employs the short-wavelength part of the spectrum with $\lambda < 1$ Å. Such neutrons, which are practically not absorbed, pass through the first crystal-monochromator and are reflected from the second.

The value of the exposure dose outside the shielding is determined by the flux of fast neutrons and the attendant flux of capture γ-rays as well as the flux of moderated neutrons. In order to reduce the thickness of the shielding in the direction of the direct beam to a minimum, a combination of iron with a hydrogen-containing material of optimum composition was used [1]: the first layer of the shielding was made of cast iron 5 cm thick, the second layer (see Fig. 1, items 4 and 5) 40 cm thick in the direction of the direct beam consists of iron shot of diameter 1-2 mm, with paraffin poured over it (the packing of the shot was close to the dense packing of spheres), and the last layer consists of lead 12 cm thick and nickel 5 cm thick. (Nickel was introduced into the last layer of the shielding to attenuate neutrons with an energy of 20-40 keV, since iron has two gaps in the scattering cross section in that energy range.) The side and upper parts of the shielding, onto which only scattered radia-tion impinges, are made of heavy concrete with a density of 3.2-3.5 g/cm^3. In view of the high directivity of the fast-neutron scattering, a large part of the iron-paraffin layer was made in the form of a sector 20 cm high, abutting on the main cylinder. This design permit-ted a decrease in the mass of the heavy shielding, which rests on a ball bearing and can be rotated about the vertical axis. Mounted inside the cylindrical shield is the crystal-mono-
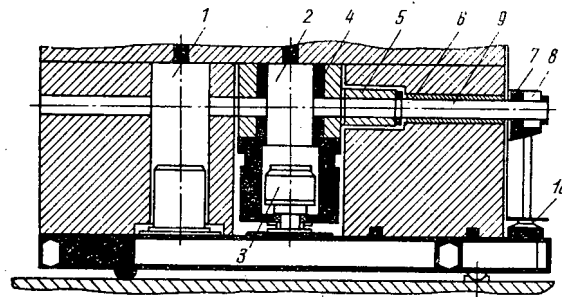
280

Fig. 2. Section of shielding in the direction of the beam: 1) niche of first crystal–monochromator; 2) niche of second crystal–monochromator; 3) monochromator module; 4) cast iron; 5) iron–paraffin mixture; 6) hydrogen–containing shielding; 7) nickel layer; 8) lead layer; 9) tube with magnetic guide field; 10) pneumatic supports.

chromator module (see Fig. 2) [3]. It rotates the monochromator and is furnished with an accurate angle–code transducer and an optical communications system for matching the rotation angles of the crystal and the reflected beam. By means of a tube (see Fig. 2), inside which the reflected beam travels in magnetic guide fields, the moving heavy shielding is rigidly connected to a "collar" 20 cm high which rests on two pneumatic supports. The latter move on a smoothly finished surface. Thus, the entire moving part of the shielding, weighing 2.5 tons, rests on three points, thus ensuring that it moves smoothly. Rigidly connected to the collar is a girder holding experimental equipment (see Fig. 1, item 9), whose other end rests on a transport module [3] on pneumatic supports. It holds a servodrive which moves the entire structure.

The hydrogen–containing part of the shielding can be made in two versions. If it is necessary that the wavelength be changed without dismantling the shielding, the hydrogen–containing layer is made in the form of two water–filled bags, between which the exit channel is located. The outer jacket of the channel has an elliptical cross section so as to ensure that the bags are in contact outside the channel. If the wavelength is changed fairly rarely, it is more expeditious to employ filling with granulated polyethylene.

The overall attenuation factor of the shielding for fast neutrons is $(4-6) \cdot 10^{11}$, the geometrical factor being $2 \cdot 10^4$. When the fast–neutron flux density at the bottom of the channel is $\sim 5 \cdot 10^{12}$ neutrons/cm$^2 \cdot$sec, of which $3.3 \cdot 10^8$ are scattered on the crystal monochromator (at a reactor power of 16–18 MW), the shielding ensures that the dose loads are permissible.

In conclusion, the authors would like to express their thanks to Yu. V. Petrov for taking an interest in the work, K. N. Semenkova and A. N. Andreev for participating in the construction of the shielding, G. Ya. Vasil'ev for carrying out neutron–flux measurements, G. A. Petrov, G. V. Val'skii, and Yu. S. Pleva for assembling the shielding, and V. A. Priemyshev for being of assistance in the fabrication of the entire complex of equipment.

<div align="center">LITERATURE CITED</div>

1. V. P. Mashkovich, Ionization Radiation Shielding [in Russian], Énergoizdat, Moscow (1982).
2. Radiation Safety Norms NRB–76 and Principal Sanitary Regulations OSP–72/80 [in Russian], Énergoizdat, Moscow (1981).
3. A. N. Darovskikh et al., Preprint No. 583, B. P. Konstantinov Institute of Nuclear Physics, Academy of Sciences of the USSR, Leningrad (1980).

# MEASUREMENT OF ENERGY AND INTENSITY OF PRINCIPAL ^{246}Cm α-GROUPS

V. M. Shatinskii

UDC 539.164

The summary report of the Third Coordinated Research Meeting on the Measurement and Evaluation of Transactinium Isotope Nuclear Data (Vienna, 1980) [1] presented the accuracy attained in the values of the half-lives and rates of α-transitions, the requirements as to the accuracy of these constants for nuclear power, the problems of guarantees, environmental protection, etc. In particular, it turns out that a 2% error is required in measurements of the intensity of the principal ^{246}Cm α-groups and the attained error is ∿5% in the absence of the necessary data for obtaining the estimated value of the intensity of ^{246}Cm α-groups.

The energy and intensity of ^{246}Cm α-groups were measured on a sample of curium isolated from spent fuel from an atomic power plant with a VVÉR-440 water-moderated water-cooled power reactor. The isotope ^{245}Cm was used as an energy standard ($E_{\alpha_{169}} = 5362.0 \pm 0.7$ keV, $I_{\alpha_{169}} = 93.2 \pm 0.5\%$ [2]) in a series of four measurements on a $\pi\sqrt{2}$ magnetic α-spectrometer [3]. The density of the active layer of the source, prepared by vacuum evaporation of a $^{243-246}$Cm mixture, is ∿2 μg/cm². The energy resolution of the spectrometer at a solid angle ∿10^{-3} from 4π and a source size of 2.50 mm² was ∿5 keV (see Fig. 1).

The following values were obtained for the ^{246}Cm nuclear physical constants: $E_{\alpha_0} = 5386.5 \pm 1.0$ keV, $I_{\alpha_0} = 82.2 \pm 1.2\%$, $E_{\alpha_{45}} = 5343.5 \pm 1.0$ keV, and $I_{\alpha_{45}} = 17.8 \pm 1.2\%$. A root-mean square error σ, which corresponds to a confidence coefficient of 0.68, is given.
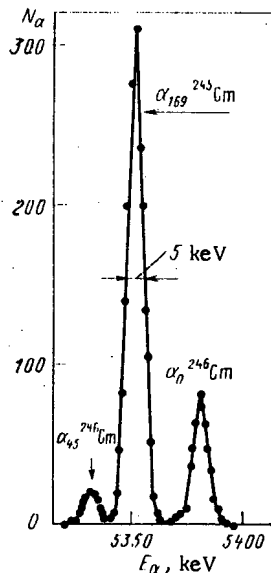
Fig. 1. Spectrum of ^{245,246}Cm.

LITERATURE CITED

1. Summary Report of Third Coordinated Research Meeting on the Measurement and Evaluation of Transactinium Isotope Nuclear Data, INDC(NDS)-118/NE, Vienna (1980).
2. S. A. Baranov, A. G. Zelenkov, and V. M. Kulakov, At. Energ., 41, No. 5, 342 (1976).
3. S. A. Baranov et al., At. Energ., 7, No. 3, 262 (1959).

APPLICATION OF FERROSULFATE SOLUTION IN DOSIMETRIC
RESEARCH ON REACTOR BEAMS

S. P. Kapchigashev, V. I. Potetnya,
and O. I. Potetnya

UDC 539.125.5.08

The wide range of energies and intensities of neutron beams used in radiobiological research necessitates the use of different dosimetry methods based on variation of the heat, ionization current, and the chemical effect. In intense fields of reactor radiation use is often made of a standard ferrosulfate solution ($FeSO_4$ system) in combination with glass thermoluminescence dosimeters, intended mainly to determine the γ-ray dose. This system is distinguished by tissue-equivalence, simplicity of preparation, high stability, a known sensitivity to γ rays, and a possibility to simulate biological objects of any shape and to carry out phantom measurements.

More extensive application of the $FeSO_4$ system in reactor dosimetry is hindered by the lack of data about the dependence of the radiation-chemical yield $G(Fe^{3+})$ of trivalent iron on the neutron energy. At the present time, because of the lack of experimental data this dependence is determined on the basis of knowledge of G for heavy charged particles, in two ways: using the universal dependence of G on the linear energy transfer (LET) and expansion of the absorbed neutron dose over the LET spectra of secondary charged particles; and using direct data about G for charged particles, determined in so-called thick-target experiments (complete stopping of particles), and expansion of the absorbed neutron dose over the spectra and types of secondary charged particles.

To date a large volume of experimental data on G for protons and α-particles has been obtained in the energy range E = 0.2–23 MeV. Practically no data, however, are available on G for C, N, and O recoil atoms in general and for all heavy charged particles for E < 0.2 MeV.

In just one experiment [1] has a high radiation-chemical yield (G_p) been detected for low-energy protons ($E \approx 70$–150 keV). The results of that paper are difficult to explain unambiguously at this time. Considering characteristic features of the energy losses of slow ions in matter and their high efficiency in the damage of macromolecules [2, 3], however, we can assume that elastic nuclear collisions are capable of causing an increase in G_p for slow protons. In [4], on the basis of concepts about the local radiation-chemical yield at each point on the proton path Ryabukhin obtained calculated values of $G(Fe^{3+})$. In the range E > 0.4 MeV the agreement between the calculated and experimental data is satisfactory. For E_p < 0.2 MeV, however, a considerable divergence is observed (by a factor of up to 2).

In this paper we present the results of experimental investigations on the action of thermal, intermediate, and fast neutrons from a BR-10 reactor on a ferrosulfate solution. The experimental values of G_n for intermediate and fast neutrons are compared with the calculated results obtained on the basis of G_p data.

A ferrosulfate solution, prepared by the standard method [5], was irradiated with neutrons from the I-2 (intermediate) and F-3 (fast) channels of the BR-10 reactor. The dosimetric data file for these investigations consisted of absorbed-dose data obtained with the aid of solid-state and activation track detectors, ionization chambers, and thermoluminescence dosimeters [6].

The radiation-chemical yield of Fe^{3+} was determined from the results of measurements of the optical density at a wavelength of 304 nm [5]. The radiation-chemical yield G_n in the solution under neutron irradiation was calculated in two approximations. In the first approximation we assumed that the entire absorbed dose of neutrons in water is due only to recoil protons. In the second approximation the value of $G_n(E)$ was obtained by taking into account the following charged particles formed in the water under the action of the neutrons:

283

TABLE 1. Values of Radiation-Chemical Yield of Fe^{3+} in Standard Ferrosulfate Solution, ions/100 eV

Radiation energy, MeV	Protons		Neutrons*			
	expt. [5]	calc. [4]	recoil protons	all particles	calc. [8]	calc. [9]
15,0	11,8	11,6	11,7	10,4	9,8	7,7
11,5	11,4	12,2	11,2	10,2	9,6	7,7
10,9	11,3	12,0	11,1	10,1	9,5	7,7
10,0	—	12,0	11,0	10,0	9,5	7,6
9,0	—	11,8	10,7	9,8	9,3	7,5
8,4	11,3	11,6	10,6	9,7	9,1	7,45
7,0	—	11,2	10,2	9,5	8,9	7,3
5,0	—	10,4	9,5	9,0	8,4	7,1
3,0	—	9,3	8,4	8,3	7,8	6,6
1,99	8,0	8,5	7,7	7,7	7,3	6,3
1,69	7,65	8,2	7,5	7,5	7,1	6,25
1,27	7,45	7,8	7,1	7,1	6,9	6,0
0,98	7,19	7,4	6,3	6,8	6,7	5,8
0,64	6,5±0,4	6,8	6,4	6,4	6,7	5,7
0,52	6,0±0,3	6,4	6,1	6,1	6,7	5,6
0,39(0,38) †	5,24(6,3)	6,2	6,0	6,0	6,8	5,5
0,29(0,3)	7,16(6,5)	6,0	5,9	5,9	6,8	5,4
0,26(0,25)	6,2(7,0)	5,9	5,9	5,9	6,85	5,4
(0,2)	(7,7)	5,8	5,8	5,8	6,9	5,4
0,15(0,15)	6,44(9,5)	5,8	5,7	5,7	7,0	5,5
(0,1)	(12,3)	5,7	5,7	5,7	7,0	5,7
(0,085)	(15,8)	5,7	5,6	5,6		
(0,070)	(16,1)	5,7	5,6	5,6		
0,05	—	5,8	5,7	5,7		
0,02	—	6,7	6,7	6,7		
0,01	—	6,9	6,5	6,5		
0,005	—	6,5	5,1	5,1		
0,002	—	3,8	2,1	2,1		

*At a radiation energy of 15.0 MeV the radiation-chemical yield according to the experimental data of [5] is 10.54-12.4 ions/100 eV.

†The data of [1] are given in parentheses.

recoil protons and protons from the nuclear reactions $^{16}O(n, p)^{16}N$ and $^{16}O(n, n'p)^{14}N$;

α particles of the reactions $^{16}O(n, \alpha)^{13}C$ and $^{16}O(n, n'\alpha)^{12}C$;

heavy recoil nuclei formed as a result of elastic and inelastic scattering of neutrons from oxygen nuclei as well as the aforementioned nuclear reactions with the emission of charged particles;

electrons and positrons formed in the water under the action of γ-ray quanta from inelastic scattering of neutrons from oxygen nuclei. The calculations were carried out from the formula

$$\bar{G}_n(E) = \sum_i \bar{G}_i(E) K_i(E) / \sum_i K_i(E),$$

where $\bar{G}_i(E)$ is the mean radiation-chemical yield of Fe^{3+} for charged particles of type i, formed in the water under the action of neutrons of energy E and $K_i(E)$ is the kerma of neutrons of energy E, caused by charged particles of type i. According to [7] the average energy of protons from nuclear reactions was assumed to be equal to 3 MeV and $G_p \approx 9.3$ ions/100 eV. The spectrum $N(E_\alpha)$ of α particles presented in [7] was used to determine $\bar{G}_\alpha$. The values of G for α particles of different energy were taken from the data of [8]. The mean radiation-chemical yield of Fe^{3+} for α particles turned out to be 5.15 ions/100 eV. For heavy recoil nuclei (C, N, O) the yield G = 4 ± 0.4 ion/100 eV. In the calculation of $\bar{G}_n$ the components of the kerma of neutrons for water were determined from data presented in [7]. Table 1 presents the values of the radiation-chemical yield of Fe^{3+} in a standard ferrosulfate solution under the action of monoenergetic protons and neutrons. It is seen that the contribution of the nuclear reaction products to $\bar{G}_n$ becomes appreciable for E = 3-4 MeV. Our calculated data differ substantially from the results of [8]. This discrepancy, reach-

ing 20% for E = 0.5 MeV, is apparently due primarily to different assumed values of $G_p(E)$. Table 1 also presents calculated data obtained in [9] for an infinite medium. The calculated values of $\overline{G_n}$ on the whole are in satisfactory agreement with the experimental data for E = 14 MeV. The discrepancy of 12-18% may be due to the contribution of γ rays to the dose being taken into account inaccurately.

Below we give the results of experimental and theoretical investigations of the radiation-chemical yield $\overline{G_n}(Fe^{3+})$ when a ferrosulfate solution is irradiated with neutrons in different channels of the BR-10 reactor (in ions/100 eV):

	F-3	I-2
Experiment	6.8 ± 0.4	9.7 ± 1.6
Calculation	6.9	6.4

It is noteworthy that the experimental yield $\overline{G_n}$ for intermediate neutrons is substantially higher than that for fast neutrons and than the calculated data. This effect may be due to the specific nature of the radiolysis of water by slow ions, in particular by elastic nuclear collisions. According to the data of [10] the two spectra investigated differ only as to the contribution of such collisions to the absorbed dose (by a factor of 1.5).

For separate measurement of absorbed doses in the thermal channel of the reactor we used a system consisting of three dosimeters: a standard ferrosulfate solution with the addition of boric acid, measuring the total absorbed dose (epithermal and thermal neutrons, γ rays); a standard solution without boric acid, practically insensitive to thermal neutrons; and a thermoluminescence dosimeter, in practice sensitive only to γ rays.

The field of radiation from channel T-4 of the BR-10 reactor has the following characteristics: rate of dosage absorption in tissue, as a result epithermal and thermal neutrons as well as γ rays, is 0.2, 0.32 ± 0.03, and 0.33 ± 0.04 Gy/h, respectively; the density of the thermal neutron flux, measured with the aid of the ferrosulfate solution with boric acid, is $(2.7 ± 0.3) \cdot 10^8$ neutrons/cm²·sec and, with the aid of ^{197}Au, $2.9 \cdot 10^8$ neutrons/cm²·sec.

From the results of the investigations it follows that a standard ferrosulfate solution is applicable to fast-neutron dosimetry; the values of $\overline{G_n}$ necessary in this case can be obtained by the usual method of calculation; the use of the standard solution for the dosimetry of intermediate neutrons requires special investigations of $G_p(E)$ at a proton energy below 0.2 MeV.

LITERATURE CITED

1. J. Pucheault and R. Julien, in: Proceedings Third Tihany Symposium on Radiation Chemistry, Budapest (1973), p. 1191.
2. S. P. Kapchigashev, in: Abstracts Third All-Union Conference on Microdosimetry [in Russian], Engineering Physics Institute, Moscow (1979), p. 114.
3. H. Jung, Naturforsch., 20, b, No. 8, 764 (1965).
4. Yu. S. Ryabukhin, in: Dosimetry and Radiation Processes in Dosimetric Systems [in Russian], Fan, Tashkent (1972), p. 185.
5. A. K. Pikaev, Dosimetry and Radiation Chemistry [in Russian], Nauka, Moscow (1975).
6. S. P. Kapchigashev et al., Med. Radiol., 22, No. 10, 64 (1977).
7. R. Caswell and J. Coyne, Rad. Research, 83, 217 (1980).
8. R. Lawson and D. Porter, Phys. Med. Biol., 20, No. 3, 420 (1975).
9. I. K. Sokolova, Chemical Methods of Dosimetry in Radiobiology [in Russian], Atomizdat, Moscow (1972).
10. V. V. Duba et al., Radiobiologiya, 19, No. 6, 893 (1979).

How To Comply With The New Copyright Law

Participation in the Copyright Clearance Center (CCC) · assures you of legal photocopying at the moment of need.

Libraries everywhere have found the easy way to fill photocopy requests legally and instantly, without the need to seek permissions, from more than 3000 key publications in business, science, humanities, and social science. You can:

Fill requests for multiple copies, interlibrary loan (beyond the CONTU guidelines), and reserve desk without fear of copyright infringement.

Supply copies from CCC-registered publications simply and easily.

The Copyright Clearance Center is your one-stop place for on-the-spot clearance to photocopy for internal use.

Its flexible reporting system accepts photocopying reports and returns an itemized invoice. You send only one convenient payment. CCC distributes it to the many publishers whose works you need.

And, you need not keep any records, the CCC computer will do it for you. Register now with the CCC and you will never again have to decline a photocopy request or wonder about compliance with the law for any publication participating in the CCC.

To register or for more information, just contact:
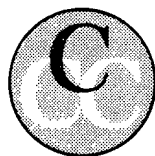
Copyright Clearance Center
21 Congress Street
Salem, Massachusetts 01970
(617) 744-3350

a not-for-profit corporation

NAME . TITLE

ORGANIZATION

ADDRESS

CITY STATE ZIP

COUNTRY TELEPHONE

CHANGING YOUR ADDRESS?

In order to receive your journal without interruption, please complete this change of address notice and forward to the Publisher, 60 days in advance, if possible.

(Please Print)

Old Address:

_____
name

_____

_____
address

_____
city

_____
state (or country)   zip code

New Address

_____
name

_____

_____
address

_____
city

_____
state (or country)   zip code

_____
date new address effective

_____
name of journal

Plenum THE LANGUAGE OF SCIENCE
PUBLISHING CORPORATION **233 Spring Street, New York, New York 10013**

MEASUREMENT TECHNIQUES
Izmeritel'naya Tekhnika
Vol. 27, 1984 (12 issues) $520

MECHANICS OF COMPOSITE MATERIALS
Mekhanika Kompozitnykh Materialov
Vol. 20, 1984 (6 issues) $430

METAL SCIENCE AND HEAT TREATMENT
Metallovedenie i Termicheskaya Obrabotka Metallov
Vol. 26, 1984 (12 issues) $540

METALLURGIST
Metallurg
Vol. 28, 1984 (12 issues) $555

PROBLEMS OF INFORMATION TRANSMISSION
Problemy Peredachi Informatsii
Vol. 20, 1984 (4 issues) $420

PROGRAMMING AND COMPUTER SOFTWARE
Programmirovanie
Vol. 10, 1984 (6 issues) $175

PROTECTION OF METALS
Zashchita Metallov
Vol. 20, 1984 (6 issues) $480

RADIOPHYSICS AND QUANTUM ELECTRONICS
Izvestiya Vysshikh Uchebnykh Zavedenii, Radiofizika
Vol. 27, 1984 (12 issues) $520

REFRACTORIES
Ogneupory
Vol. 25, 1984 (12 issues) $480

SIBERIAN MATHEMATICAL JOURNAL
Sibirskii Matematicheskii Zhurnal
Vol. 25, 1984 (6 issues) $625

SOIL MECHANICS AND FOUNDATION ENGINEERING
Osnovaniya, Fundamenty i Mekhanika Gruntov
Vol. 21, 1984 (6 issues) $500

SOLAR SYSTEM RESEARCH
Astronomicheskii Vestnik
Vol. 18, 1984 (6 issues) $365

SOVIET APPLIED MECHANICS
Prikladnaya Mekhanika
Vol. 20, 1984 (12 issues) $520

SOVIET ATOMIC ENERGY
Atomnaya Énergiya
Vols. 56-57, 1984 (12 issues)..................... $560

SOVIET JOURNAL OF GLASS PHYSICS AND CHEMISTRY
Fizika i Khimiya Stekla
Vol. 10, 1984 (6 issues) $235

SOVIET JOURNAL OF NONDESTRUCTIVE TESTING
Defektoskopiya
Vol. 20, 1984 (12 issues) $615

SOVIET MATERIALS SCIENCE
Fiziko-khimicheskaya Mekhanika Materialov
Vol. 20, 1984 (6 issues) $445

SOVIET MICROELECTRONICS
Mikroélektronika
Vol. 13, 1984 (6 issues) $255

SOVIET MINING SCIENCE
Fiziko-tekhnicheskie Problemy Razrabotki Poleznykh Iskopaemykh
Vol. 20, 1984 (6 issues) $540

SOVIET PHYSICS JOURNAL
Izvestiya Vysshikh Uchebnykh Zavedenii, Fizika
Vol. 27, 1984 (12 issues) $520

SOVIET POWDER METALLURGY AND METAL CERAMICS
Poroshkovaya Metallurgiya
Vol. 23, 1984 (12 issues) $555

STRENGTH OF MATERIALS
Problemy Prochnosti
Vol. 16, 1984 (12 issues) $625

THEORETICAL AND MATHEMATICAL PHYSICS
Teoreticheskaya i Matematicheskaya Fizika
Vol. 58-61, 1984 (12 issues)...................... $500

UKRAINIAN MATHEMATICAL JOURNAL
Ukrainskii Matematicheskii Zhurnal
Vol. 36, 1984 (6 issues) $500

Send for Your Free Examination Copy

RUSSIAN JOURNALS IN THE PHYSICAL AND MATHEMATICAL SCIENCES

AVAILABLE IN ENGLISH TRANSLATION

ALGEBRA AND LOGIC
Algebra i Logika
Vol. 23, 1984 (6 issues) $360

ASTROPHYSICS
Astrofizika
Vol. 20, 1984 (4 issues) $420

AUTOMATION AND REMOTE CONTROL
Avtomatika i Telemekhanika
Vol. 45, 1984 (24 issues) $625

COMBUSTION, EXPLOSION, AND SHOCK WAVES
Fizika Goreniya i Vzryva
Vol. 20, 1984 (6 issues) $445

COSMIC RESEARCH
Kosmicheskie Issledovaniya
Vol. 22, 1984 (6 issues)........................... $545

CYBERNETICS
Kibernetika
Vol. 20, 1984 (6 issues)........... .... $445

DIFFERENTIAL EQUATIONS
Differentsial'nye Uravneniya
Vol. 20, 1984 (12 issues) $505

DOKLADY BIOPHYSICS
Doklady Akademii Nauk SSSR
Vols. 274-279, 1984 (2 issues) $145

FLUID DYNAMICS
Izvestiya Akademii Nauk SSSR,
Mekhanika Zhidkosti i Gaza
Vol. 19, 1984 (6 issues) $500

FUNCTIONAL ANALYSIS AND ITS APPLICATIONS
Funktsional'nyi Analiz i Ego Prilozheniya
Vol. 18, 1984 (4 issues) 410

GLASS AND CERAMICS
Steklo i Keramika
Vol. 41, 1984 (6 issues) $590

HIGH TEMPERATURE
Teplofizika Vysokikh Temperatur
Vol. 22, 1984 (6 issues) $520

HYDROTECHNICAL CONSTRUCTION
Gidrotekhnicheskoe Stroitel'stvo
Vol. 18, 1984 (12 issues) $385

INDUSTRIAL LABORATORY
Zavodskaya Laboratoriya
Vol. 50, 1984 (12 issues) $520

INSTRUMENTS AND EXPERIMENTAL TECHNIQUES
Pribory i Tekhnika Éksperimenta
Vol. 27, 1984 (12 issues) $590

JOURNAL OF APPLIED MECHANICS AND TECHNICAL PHYSICS
Zhurnal Prikladnoi Mekhaniki i Tekhnicheskoi Fiziki
Vol. 25, 1984 (6 issues) $540

JOURNAL OF APPLIED SPECTROSCOPY
Zhurnal Prikladnoi Spektroskopii
Vols. 40-41, 1984 (12 issues) $540

JOURNAL OF ENGINEERING PHYSICS
Inzhenerno-fizicheskii Zhurnal
Vols. 46-47, 1984 (12 issues) $540

JOURNAL OF SOVIET LASER RESEARCH
A translation of articles based on the best Soviet research in the field of lasers
Vol. 5, 1984 (6 issues) $180

JOURNAL OF SOVIET MATHEMATICS
A translation of Itogi Nauki i Tekhniki and *Zapiski Nauchnykh Seminarov Leningradskogo Otdeleniya Matematicheskogo Instituta im. V. A. Steklova AN SSSR*
Vols. 24-27, 1984 (24 issues)..................... $1035

LITHOLOGY AND MINERAL RESOURCES
Litologiya i Poleznye Iskopaemye
Vol. 19, 1984 (6 issues) $540

LITHUANIAN MATHEMATICAL JOURNAL
Litovskii Matematicheskii Sbornik
Vol. 24, 1984 (4 issues) $255

MAGNETOHYDRODYNAMICS
Magnitnaya Gidrodinamika
Vol. 20, 1984 (4 issues) $415

MATHEMATICAL NOTES
Matematicheskie Zametki
Vols. 35-36, 1984 (12 issues).................... $520